Direct numerical simulation of free-surface and interfacial flow using the VOF method : cavitating bubble clouds and phase change

Leon Malan

Ph.D Thesis Manuscript

Direct Numerical Simulation of Free-Surface and Interfacial Flow Using the VOF Method: Cavitating Bubble Clouds and Phase Change

Author:
Léon Malan

Supervisors:
Prof. Stéphane Zaleski
Prof. Arnaud Malan
Prof. Pieter Rousseau

September 2017

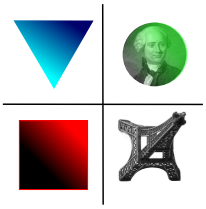

Acknowledgements

D'Alembert, Paris

The work in Part I was funded by the French Atomic and Alternative Energies Commission (CEA). Simulations were run on the Airain supercomputer at the TGCC (*Très Grand Centre de calcul*) computing facility. I thank them for their kind co-operation. I also would like to thank Antoine Llor for his support and enthusiastic participation as well as Laurianne Pillon and Renaud Motte.

Thank you to the permanent staff members at D'Alembert for welcoming me to the lab. Christophe Josserand, Pierre-Yves Lagrée, Stéphane Popinet and Maurice Rossi: thank you for interesting discussions and general scientific advice. Thank you also to Simona, Olivier, Pascal, Catherine and Evelyne for your constant friendly assistance in the lab.

To my fellow students and friends at D'Alembert - Vincent, Christian, Barend, Raphaël, Andrés, Jaïr, Paul, Antoine, Aditya, Valentina, Zhen, Bertrand, Peng, Jan, Walid, Bharat, Gounséti, Julien, Aurélie, Hervé, Elisabeth, Etienne, David, Léo, Cansu, Geoffroy and Alex - thank you for all the good memories.

To my fellow PARIS collaborators, Matteo, Tomas, Daniel and Stanley: Thank you for working together on a project that meant a tremendous amount to me.

Thank you Prof. Gretar Tryggvason and Dr. Jaicai Lu for the friendly visit to Notre Dame and the phase change discussions that ensued.

Lastly, I would like to thank my supervisor, Prof. Stéphane Zaleski. If it wasn't for your enthusiastic reply to an uncertain Steam Turbine Engineer in South Africa looking to do Fluid Mechanics, this Ph.D would never have been written. I appreciate your constant support, interest in my work and dedication to the project. It was an absolute pleasure and priviledge working with you.

InCFD, Cape Town

Funding for Part II of the work was provided by the South African Research Chair Initiatives (SARChI) program of the National Research Foundation (NRF).

Thank you to all my fellow INCFD students: Matt, William, Roy, Donovan, Christa, Andrew, Javon, Niran, Bevan, Kobus and Tomas. I really enjoyed the office environment and team work.

Prof. Pieter, thank you for investing so much effort and (personal) resources to establish the collaboration. I appreciated your guidance throughout the project. Prof. Arnaud, thank you for your unwavering support. You inspired me to deliver my best and cemented my passion for CFD.

Persoonlike Bedankings

Hierdie projek was 'n spanpoging. Alhoewel my naam op die titelblad staan, sou dit nooit moontlik gewees het sonder die opoffering, ondersteuning en aanmoediging van 'n merkwaardige groep mense nie. Hierdie groep strek wyd. Vriende uit Suid-Afrika wat ons besoek het in Parys, soos die Van Niekerks, McLaggans, Scholtze, Corneels en Reinier. Die Dalais en La Cité vriende. Die Bloemhofs: Lisses was ons tuiste in Parys en julle was soos familie vir ons, baie dankie! Martin, Petro en gesin: julle inspireer my om voluit te lewe.

Baie dankie aan my familie. Julle is fantasties en ek waardeer al die kuiers, oproepe en motivering.

Aan my ouers, julle leer my elke dag oor die belangrike dinge in die lewe. Kruger ouers, julle huis is vir ons 'n tuiste, maar julle harte ook en ek waardeer julle oneindig baie. Dit is 'n voorreg om julle as ouers te hê en ek is baie lief vir julle.

Malan ouers, julle aanmoediging, gebede, liefde, besoeke en opoffering is onvergeetlik. Ek lief julle en waardeer julle.

Lisa en Klara: julle kon nie kies om tydens 'n Ph.D julle verskyning op aarde te maak nie, maar ek is so dankbaar julle het. En my liefste Mina: daar is baie laat nagte, enkelouer-dae en opoffering van jou in hierdie blaaie, wat niemand ooit sal kan meet nie. Jy is my inspirasie. Ek is so dankbaar vir jou en jou ondersteuning en ek sou nooit hierdie werk kon afhandel sonder jou nie.

Laastens besef ek dat in die oneindig groter prentjie van die ewigheid is hierdie werk 'n onbenullige deel van die woel en werskaf op die aarde. My gebed is: My Pa in die Hemel, mag hierdie werk bydra dat jou Koninkryk hier op aarde kom en jou Naam verheerlik word.

Abstract

Direct Numerical Simulation of two-phase flow is used extensively for engineering research and fundamental fluid physics studies [54, 81]. This study is based on the Volume-Of-Fluid (VOF) method, originally created by Hirt and Nicols [30]. This method has gained increased popularity, especially when geometric advection techniques are used coupled with a planar reconstruction of the interface [14, 89].

The focus of the first part of this work is to investigate the hydrodynamics of isothermal cavitation in large bubble clouds, which originated from a larger study of micro-spalling [61], conducted by the French CEA. A method to deal with volume-changing vapour cavities, or pores, was formulated and implemented in an existing code, PARIS . The flow is idealized by assuming an inviscid liquid, negligible thermal effects and vanishing vapour pressure. A novel investigation of bubble cloud interaction in an expanding liquid using Direct or Detailed Numerical Simulation is presented. The simulation results reveal a pore competition, which is characterised by the Weber number in the flow.

In the second part of the study the governing equations are extended to describe incompressible flow with phase change [79]. The description of the work commences with the derivation of the governing equations. Following this, a novel, geometric based, VOF solution method is proposed. In this method a novel way of advecting the VOF function is invented, which treats both mass and energy conservation in conservative form. New techniques include the advection of the interface in a discontinuous velocity field. The proposed algorithms are consistent and elegant, requiring minimal modifications to the existing code. Numerical experiments demonstrate accuracy, robustness and generality. This is viewed as a significant fundamental development in the use of VOF methods to model phase change.

Contents

Chapter 1

Introduction

This chapter will provide the background to the topic of interest in this work. It includes a general introduction to the topic and the analysis techniques that will be used throughout this work as well as the origin of the choice of problems to be studied. The original contribution to knowledge that is the aim of this project will be summarized followed by the outline of the remainder of this document.

1.1 Problem Background

A notable observation to make about the tangible environment in which humans live, is that much of it consist of fluids. The study of fluid flow has been a lasting human endeavour. It is not only pursued to gain understanding of the natural world, it is also hugely important for industrial processes. A quick example of this is the fact that the majority of electricity that is generated in the world today, comes from power plants where the Rankine cycle is used to convert heat energy to electrical energy in a turbo-generator.

In modern times, a significant achievement in the field of fluid mechanics was the mathematical description of fluid flow by the Navier-Stokes equations, credited to C.L.M.H. Navier and Sir George G. Stokes. There is notable research activity in theoretical and applied mathematics on modelling fluid flow. However, the complex nature of the mathematical description of industrial flows leave them practically unsolvable by the analytical solution techniques at our disposal today.

Numerical analysis is another approach that is well suited to study flows, since many of the analytical difficulties can be overcome by using numerical approximations. With the ever increasing improvement in computing capabilities, the field of computational fluid dynamics (CFD) has grown immensely. Direct numerical simulation (DNS) is one approach that is applied to multi-phase flow problems, [81, 54]. The main idea of DNS is to resolve the flow domain to a sufficient level such that additional physical models to account for unresolved flow effects are minimal or excluded all together.

In the case of multi-phase flow, a phase tracking method is required to distinguish between phases. For this study the Volume-Of-Fluid (VOF) method will be used, of which the much cited first publication belongs to Hirt and Nichols [30]. Major improvements since the invention of VOF include the reconstruction of the interface using a piece-wise linear construction (PLIC), introduced by De Bar [14] and Youngs [89], momentum-conserving schemes [49] and height functions [42, 46] to calculate local geometrical quantities such as interface normal and curvature. Interface advection to conserve mass to machine accuracy has also been achieved by Yue and

Weymouth [87]. These advances as well as relative ease of implementation in codes has made the VOF method popular for industrial and research applications.

In this work, different multi-phase flow problems will be studied with the VOF method in order to gain better understanding of the behaviour of flows and to evaluate improvements on methods in which they are studied. The next section will elaborate more on the background to the project and the problems that will be studied.

1.2 Project background

This work is a collaboration between two institutions. The formal French term for the collaboration is *thèse en co-tutelle*. A summary of the project and problem of interest at each of the institutions will be given here.

The first part of the work was conducted at *Institut Jean Le Rond ∂'Alembert* – or D'Alembert for short – in Paris, France. It is divided into five teams, with research focus on Mechanics, Acoustics and Energetics. The D'Alembert institute is affiliated to the CNRS and the Pierre and Marie Curie University (*Université Pierre et Marie Curie, Paris VI Sorbonne*), which is part of the Paris Sorbonne group of universities. A research group within the French Alternative Energies and Atomic Energy Commission or CEA (*Commissariat à l'énergie atomique et aux énergies alternatives*) is interested in micro-spall failure of materials [61, 60] and wished to gain more insights by performing numerical simulations. This work is the result of them defining a model problem and collaborating with D'Alembert to investigate it. The model problem will be described in more detail in Part I . In summary, it is an idealized problem where the interactions between bubbles are studied when hundreds of bubbles are present in a carrier liquid while it is expanding. Thermal effects are neglected and a free surface approach is introduced to allow for volume changing bubbles in an incompressible liquid.

The second part of the work was conducted in Cape Town, South Africa. The Industrial CFD research group (InCFD) is affiliated to the Department of Mechanical Engineering in the faculty of Engineering and the Built Environment of the University of Cape Town. This group is also home to the South African Research Chair (SARChI) in Industrial Computational Fluid Dynamics. This group has relations with a variety of industrial partners. A problem that is of interest not only to this group, but also to researchers and industries worldwide is the direct numerical simulation of phase change processes. Part II of the work focusses on this problem and specifically investigates a novel technique to simulate phase change using a VOF method and the geometric interface reconstruction method for a sharp interface representation.

1.3 Original contributions in this work

An existing computer code was used as a platform for this work. The code is called PARIS and will be introduced in Chapter 3. New developments were made to the code in order to enable the simulation of problems that include physics that has not previously been accounted for in the code. Apart from software development contributions, there were novel scientific contributions. The contribution made in each part of the work will be given separately.

For the bubble cloud simulations, a free surface approach is applied to an existing VOF framework. The ability to apply a polytropic equation of state for the bubble phase was introduced and an existing algorithm was applied to enable the tracking of individual bubbles. This made the data of their movement and volume evolution available during simulations of hundreds of bubbles. To the best knowledge of the author, this is the first time that the interaction of bubbles was studied using DNS as an idealized model for micro-spall.

In the phase change work, a thermal energy conservation equation was added to the existing code. In this equation, an implicit discretisation of the heat conduction term (with special treatment at the interface) was added. Another addition was a temperature dependent density in the gravity term of the momentum equation according to the Boussinesq approximation. A novel method is proposed to perform the advection of the VOF colour function when phase change occurs and velocity jumps exist across the interface. The advection is based on geometric reconstruction of the interface. This advection strategy is applied consistently to the advection term in the energy equation to ensure an energy flux that is consistent around the interface with the calculated movement of the fluid and the interface relative to it.

1.4 Thesis Outline

This chapter provided an introduction to the work that is represented in this thesis. The work will be divided into two parts, each corresponding to the problem studied at each of the collaborating institutions. Before the two parts are presented, a general mathematical formulation will be provided that will serve as a reference to both parts.

After a mathematical reference for the work is established, another important element that is common to both parts will be presented: the computer software that will be employed throughout this work. PARIS will be used to solve each of the numerical problems presented later on. The modifications made to it in order to do so will be introduced in the respective parts for each individual problem.

The foundations are now laid to continue to the individual parts. Each part will be presented with a similar structure: at first, the problem background will be given with an overview of other work on the problem. Thereafter, the problem-specific mathematical formulation will be given. The numerical method employed to discretize and solve the governing equations in the mathematical formulation will then be presented, followed by a results chapter. Verification tests will be provided as well larger simulations to study certain physical problems. The individual parts will then conclude with a discussion and some perspectives on the results and further work.

Part I will study the behaviour of bubble clouds when it is subject to expansion of the carrier liquid in which they exist. Different flow conditions will be tested to establish the effect that bubble interactions exhibit on the expansion of the carrier fluid. Part II will study two-phase flows with phase change.

Chapter 2

Mathematical formulation

2.1 Introduction

In this chapter a general mathematical formulation is presented that will serve as a reference for the specific problems that will be introduced later in Parts I and II. Each problem will eventually have its own governing equations. The specific formulation for each problem will be derived by making certain simplifying assumptions and applying different physical models to the general formulation that will be presented here.

The general mathematical formulation will be derived in a classical manner: by considering a generic control volume. Throughout this chapter, the derivations are inspired by and reproduced from the texts of Kundu and Cohen [12], White [88] and Tryggvason *et al.* [81]. There are simplifying assumptions that apply to all problems that will be studied in this work. These assumptions will be presented, followed by the derivations of the governing equations from first principles.

2.2 Simplifying assumptions

It will be assumed throughout this work that all fluids can be treated as matter in which the physics at molecular level has a representative average effect at a larger scale. This is called the continuum hypothesis. Some perspective on its validity is given in the next section.

2.2.1 Continuum hypothesis

The continuum hypothesis is reasonable under certain conditions. One aspect to consider is the length scale of the problem in question. White [88, p.6] provides a lower limit based on the uncertainty in measurements of fluid density: when fluid density is calculated by measuring the molecular mass δm in a volume δV, there is significant uncertainty in the result when $\delta V < 10^{-9}\ mm^3 = 10^{-18}\ m^3$. This is a conservative case for all liquids and gases at atmospheric conditions. For a spherical volume δV, the radius R will be $R \approx 6 \times 10^{-7}\ m = 600\ nm$ for a volume of this size.

Kundu [12, p.5] uses the mean free path of fluid particles (atoms or molecules) as a reference for the breakdown in modelling accuracy of continuum mechanics and where molecular dynamics becomes important. The mean free path ℓ_{mfp} of air at atmospheric conditions is estimated $\ell_{mfp} \approx 5 \times 10^{-8}\ m = 50\ nm$. For liquids at atmospheric conditions, [81] provides that $\ell_{mfp} \approx 10^{-9}\ m = 1\ nm$.

For the problems considered in this work, the physical fluid parameters and length scales were found to fall safely within the limits of the continuum approach.

2.2.2 Incompressible flow

In certain flow situations the effect of pressure on the density of the fluid is much less than its effect on the flow velocity. Under these circumstances, one can apply the incompressible flow assumption, which assumes that the density in a fluid (or phase) is invariant to pressure changes

$$\frac{\partial \rho}{\partial p} = 0\,, \tag{2.1}$$

with p the static pressure in the fluid. Furthermore, the variation of density with temperature is deemed negligible, except for the body force term in the momentum conservation equation. The result is that for a specific fluid or phase, the density is considered a constant.

The validity of these assumptions can be shown [88, p.231][12, p.715] to be related to the Mach number in the flow. The Mach number Ma is a non-dimensional number that gives the ratio between the flow velocity magnitude, u and the sonic velocity, c, in the fluid under consideration at the prevailing conditions

$$\mathrm{Ma} = \frac{u}{c}\,. \tag{2.2}$$

Both references — [88, p.231] and [12, p.715] — show that the incompressible assumption is applicable when $\mathrm{Ma} < 0.3$. It is important to note that the Mach number criteria here is a guideline and not a general rule. It is possible to imagine flows where fluids are compressed at a low velocity, for example in a cylinder with a moving piston. Some other considerations are applicable in this case, as shown by Heyns *et al.* [29].

However, for the purpose of this work, the guideline of small flow velocities will be followed and the incompressible assumption is applied without any special additional compressibility considerations.

2.2.3 Boussinesq approximation

Throughout this work and unless stated otherwise, the Boussinesq approximation will be used. A formal discussion on its validity is given by Spiegel and Veronis [67]. Similarly, Kundu provides arguments for the application of the approximation [12, p.124-128]. The reader can consult these works for more detail. The Boussinesq approximation is a simplification applied to the general governing equations of fluid flow. It assumes that variations in density have a negligible effect on all terms relating to momentum conservation, apart from the body force term. Additionally, it is assumed that temperature variations are small, relative to the bulk average temperature. The effects of these assumptions on the conservation of mass, momentum and thermal energy will be shown.

2.3 Control volume analysis

In this section, a generic control volume for the problems under consideration in this work will be defined. The rate of change of a generic fluid property will then be evaluated in this control volume.

2.3.1 Control volume definition

Following White [88], some fluid property B is considered in a closed system. The system is defined as all fluid contained inside a control volume V which exists in three dimensional space, $\mathbb{R}^3$. The control volume is completely enclosed by control surface S and is shown in Fig. 2.1. The choice of a fixed control volume is made based on the numerical discretization of the equations in a finite volume or calculating a finite difference at a fixed location in space, which will be detailed in later chapters. The specific quantity — per unit mass — of B is $\beta = {}^{dB}/_{dm}$, with dm the mass of a differential quantity, dB.

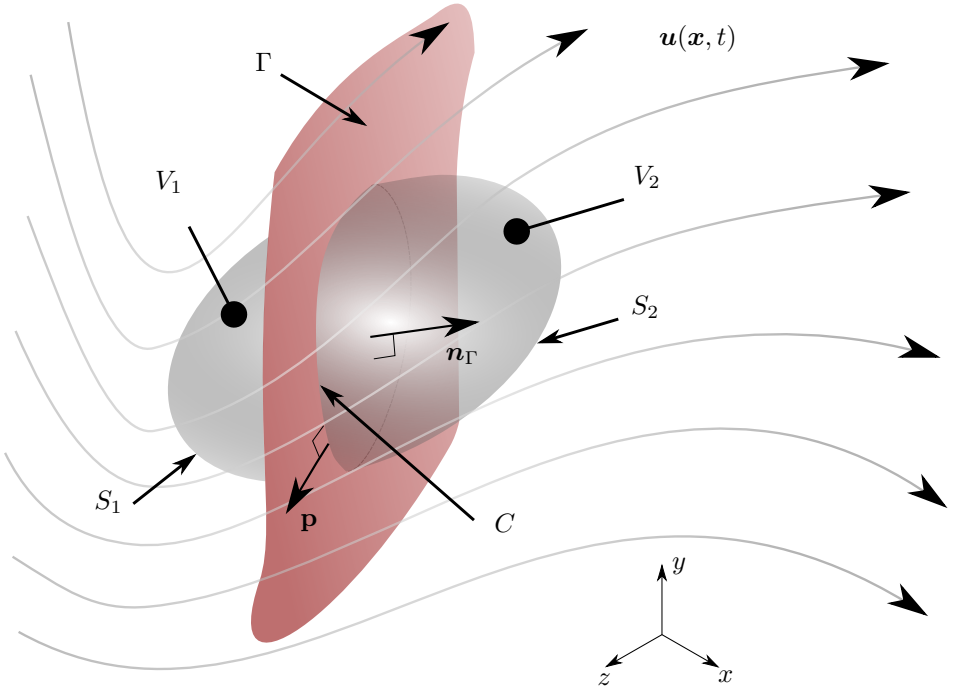

Figure 2.1: A general, 3D control volume V in an arbitrary velocity field $\boldsymbol{u}\,(\boldsymbol{x},t)$ is shown. V is enclosed by surface S, which is fixed in space. The red shaded surface, Γ is an arbitrary surface that represents the interface and divides V into V_1 and V_2 and S into S_1 and S_2. The intersection of Γ with S is the contour C, with normal $\mathbf{p}$ in the osculating plane.

Unless stated otherwise, a standard Cartesian coordinate system in three dimensions will be used throughout this work. The total rate of change of fluid property B in the system is [88, p. 144]

$$\left.\frac{dB}{dt}\right|_{sys} = \int_V \frac{\partial\,(\rho\beta)}{\partial t}\,dV + \oint_S \rho\beta\,(\boldsymbol{u}\cdot\boldsymbol{n})\,dA\,, \tag{2.3}$$

with t the time and ρ the density such that $\rho = \frac{dm}{dV}$. The surface unit normal on S is $\boldsymbol{n}$ with the convention that it is positive in the direction pointing outward. Therefore the surface integral represents the total efflux of B from V through control surface S. The interface Γ is a material surface with unit normal $\boldsymbol{n}_\Gamma$, which moves with the fluid velocity $\boldsymbol{u}(\boldsymbol{x},t)$. The position vector $\boldsymbol{x}$ is given by $\boldsymbol{x} = x\,\boldsymbol{i} + y\,\boldsymbol{j} + z\,\boldsymbol{k}$ with $\langle \boldsymbol{i},\boldsymbol{j},\boldsymbol{k}\rangle$ the orthogonal Cartesian unit vectors.

Two fluids are represented in control volume V, namely fluid 1 in V_1 and fluid 2 in V_2. The naming convention used in this work is that the fluids represent different phases (phase 1 and phase 2) in a two-phase flow. Note that this convention places no physical constraint on the definition of problems, since the fluid properties can be chosen arbitrarily to represent any fluid. It is merely a convention to avoid ambiguity.

2.3.2 Conservation of a fluid property

Conservation of a property in a system means that it cannot be created or destroyed, so that

$$\left.\frac{dB}{dt}\right|_{sys} = 0\,. \tag{2.4}$$

Conservation of B in V requires that

$$\left.\frac{dB}{dt}\right|_{sys} = \int_V \frac{\partial\left(\rho\beta\right)}{\partial t}\,dV + \oint_S \rho\beta\left(\boldsymbol{u}\cdot\boldsymbol{n}\right)\,dA = 0\,. \tag{2.5}$$

The physical interpretation of (2.5) when B is conserved is that the net change of B inside V must be balanced by the net amount of B flowing across its bounding surface S.

Before the general conservation of mass, momentum and energy will be presented, some useful comments and results on the mathematical formulation of two-phase flows will be presented.

2.4 Two-phase flows

As mentioned in the introduction, the flow problems in this work will be two-phase in nature, of which each phase has its own fluid properties. A general method to represent the interface and to include the physics related to it will be presented here. Note that the work in this section, including 2.4.1 and 2.4.2 is credited to Tryggvason *et al.* [81]. Many of the mathematical tools related to flows with interfaces in this reference are used in PARIS that will be used in this work. For convenience of reading, the former tools are defined in the next section, while PARIS will be detailed in Chapter 3.

2.4.1 Interface between fluids

Throughout this work, it will be assumed that the interface between fluids (or phases) is sharp, or infinitely thin. The fluids will also be considered immiscible, meaning that there is no dilution of the one fluid into the other and no diffusion of mass across the interface is possible. Transfer of mass by phase change will be possible and will be detailed in Part II. The interface is represented geometrically as a surface of arbitrary shape.

A full derivation of various interface properties are given in Appendix A of [81, p.270-278]. The main result that will be of use in this work is that the interface mean curvature κ is given by the equation

$$\kappa = \kappa_1 + \kappa_2 = -\boldsymbol{\nabla}_\Gamma\cdot\boldsymbol{n}_\Gamma\,, \tag{2.6}$$

with κ_1 and κ_2 the principal curvatures and $\boldsymbol{\nabla}_\Gamma$ the surface gradient on surface Γ with outward pointing normal $\boldsymbol{n}_\Gamma$.

2.4.2 One-fluid formulation

The main idea of the one-fluid formulation is to distinguish between fluids or phases by using an indicator function that is attributed to a specific phase. The Heaviside function seems a suitable choice for this purpose, so a convention is made where

$$H(\boldsymbol{x}) = \begin{cases} 1, & \text{if } \boldsymbol{x} \text{ is inside } V_1 \\ 0, & \text{if } \boldsymbol{x} \text{ is inside } V_2 \,. \end{cases} \tag{2.7}$$

Note that in this case, phase 1 is the tracked phase and that the entire volume V is partitioned into V_1 and V_2, with $\boldsymbol{x}$ the position vector. The definition of H can be constructed by using the integral of consecutive products of one dimensional Dirac delta functions, which is extended to three dimensions for V from the derivation in [81, p.279]

$$H(\boldsymbol{x}) = \int_V \delta(x - x')\,\delta(y - y')\,\delta(z - z')\,dv' \,, \tag{2.8}$$

where $dv' = dx'\,dy'\,dz'$ and $\boldsymbol{x}' = \langle x', y', z' \rangle$ is a vector function indicating the location of the tracked phase. This construction is very useful, since it can be shown [81, p.280] that

$$\boldsymbol{\nabla} H = -\delta_\Gamma \boldsymbol{n}_\Gamma \,, \tag{2.9}$$

with δ_Γ a Dirac delta function distributed along the interface, with normal $\boldsymbol{n}_\Gamma$ pointing from phase 1 into phase 2. It can also be used to convert surface integrals — like those on the interface — into volume integrals [81, p.280]

$$\int_\Gamma f(\boldsymbol{x})\,dA = \int_V f(\boldsymbol{x}) \delta_\Gamma(\boldsymbol{x})\,dV \,, \tag{2.10}$$

with $f(\boldsymbol{x})$ any arbitrary function.

2.5 Governing equations

In this section, the general conservation of mass, momentum and thermal energy will be derived for the arbitrary control volume in Fig.2.1.

2.5.1 Mass conservation

Conservation of mass states that the total mass in a system is conserved and cannot be created or destroyed

$$\left.\frac{dm}{dt}\right|_{sys} = 0 \,. \tag{2.11}$$

For the case of mass, $B = m$ and $\beta = \dfrac{dm}{dm} = 1$ so that (2.5) is rewritten

$$\left.\frac{dm}{dt}\right|_{sys} = 0$$

$$\therefore \int_V \frac{\partial \rho}{\partial t}\,dV + \oint_S \rho\,(\boldsymbol{u} \cdot \boldsymbol{n})\,dA = 0 \tag{2.12}$$

This equation is the integral form of the conservation of mass in control volume V. Note that the first term is generally non-zero in V, despite the assumption of constant phase density. The reason is that, in general, there may be more than one phase present in V. Mass conservation can be written for each separate phase

$$\frac{d}{dt}\left(\int_{V_1}\rho_1\,dV\right)=\int_{V_1}\frac{\partial\rho_1}{\partial t}\,dV+\int_{S_1}\rho_1\left(\boldsymbol{u}_1\cdot\boldsymbol{n}\right)\,dA+\int_{\Gamma}\rho_1\left(\boldsymbol{u}_1\cdot\boldsymbol{n}_\Gamma\right)\,dA\;=\;0 \tag{2.13}$$

$$\frac{d}{dt}\left(\int_{V_2}\rho_2\,dV\right)=\int_{V_2}\frac{\partial\rho_2}{\partial t}\,dV+\int_{S_2}\rho_2\left(\boldsymbol{u}_2\cdot\boldsymbol{n}\right)\,dA-\int_{\Gamma}\rho_2\left(\boldsymbol{u}_2\cdot\boldsymbol{n}_\Gamma\right)\,dA\;=\;0\,. \tag{2.14}$$

The reader is reminded of the convention that normal $\boldsymbol{n}_\Gamma$ points from phase 1 outward into phase 2, which explains the sign of the surface integrals over Γ. The separate phase volumes can be simplified by applying the constant density assumption

$$\int_{S_i}\boldsymbol{u}_i\cdot\boldsymbol{n}\,dA+\int_{\Gamma}\boldsymbol{u}_i\cdot\boldsymbol{n}\,dA=\int_{V_i}\boldsymbol{\nabla}\cdot\boldsymbol{u}\,dV=0\,, \tag{2.15}$$

where the subscript $i=1,2$ indicates the phase. Note that the outward pointing surface normal $\boldsymbol{n}$ was used throughout for the surface integrals. The divergence theorem of Gauss was applied, since the velocities are smooth everywhere within a phase.

2.5.2 Conservation of linear momentum

The conservation of linear momentum is based on Newton's second law of motion. The law states that the acceleration of a system is directly proportional to the resultant force applied to it, with its inertia (or mass) the proportionality constant. Equivalently, the rate of change of the momentum of a system is equal to the resultant force acting on it:

$$\boldsymbol{F}_R=\sum_{sys}\boldsymbol{F}=m\boldsymbol{a}|_{sys}=m\left.\frac{\partial\boldsymbol{u}}{\partial t}\right|_{sys}\,, \tag{2.16}$$

with $\boldsymbol{F}_R$ a resultant force vector, m the system mass and $\boldsymbol{a}$ the system acceleration vector.

For a fixed control volume, (2.3) is rewritten with the general fluid property B substituted with the linear momentum vector $\mathbf{P}=m\boldsymbol{u}$ so that $\beta=\boldsymbol{u}$

$$\sum_{sys}\boldsymbol{F}=m\left.\frac{\partial\boldsymbol{u}}{\partial t}\right|_{sys}=\int_V\frac{\partial\left(\rho\boldsymbol{u}\right)}{\partial t}\,dV+\oint_S\rho\boldsymbol{u}\left(\boldsymbol{u}\cdot\boldsymbol{n}\right)\,dA\,. \tag{2.17}$$

To evaluate (2.17), all forces acting on the system defined by V need to be determined. Fluid forces can be divided into surface, body and line forces [12].

$$\sum_{sys}\boldsymbol{F}=\boldsymbol{F}_s+\boldsymbol{F}_b+\boldsymbol{F}_\sigma\,, \tag{2.18}$$

with $\boldsymbol{F}_s$, $\boldsymbol{F}_b$ and $\boldsymbol{F}_\sigma$ respectively the surface, body and line forces. Each type of force will be presented individually.

Surface forces

The force on a surface is obtained by first considering the state of stress in a fluid. The stress at a point in a fluid is represented by a second order tensor, $\boldsymbol{\tau}$. As demonstrated in Kundu [12], this tensor is symmetric and can be written

$$\boldsymbol{\tau} = -p\mathbf{I} + \mathbf{D} \tag{2.19}$$

where p is the pressure, $\mathbf{I}$ the unit tensor and $\mathbf{D}$ the deviatoric stress, or deformation tensor. Throughout this work, a Newtonian fluid will be assumed, so that the deformation tensor is given by [12, p.101]

$$\mathbf{D} = 2\,\mu\,\mathbf{S} + \lambda\,(\boldsymbol{\nabla}\cdot\boldsymbol{u})\,\mathbf{I}\,, \tag{2.20}$$

with μ the dynamic viscosity, λ the second coefficient of viscosity and $\mathbf{S}$ the fluid strain rate tensor [12, p.61]

$$\mathbf{S} = \frac{1}{2}\left(\nabla\boldsymbol{u} + (\nabla\boldsymbol{u})^T\right)\,. \tag{2.21}$$

Stokes hypothesis is often applied [81, 88, 12], so that $\lambda = -{}^2/_3\,\mu$. The stress tensor for a Newtonian fluid therefore is [12, p.103]

$$\boldsymbol{\tau} = -\left(p + \frac{2}{3}\mu\,(\boldsymbol{\nabla}\cdot\boldsymbol{u})\right)\mathbf{I} + \mu\left(\nabla\boldsymbol{u} + (\nabla\boldsymbol{u})^T\right)\,. \tag{2.22}$$

The resultant surface force, $\delta\boldsymbol{F}_s$, on a segment S of some surface in a fluid can be shown [12, p.35] to be

$$\delta\boldsymbol{F}_s = \int_S \boldsymbol{\tau}\cdot\boldsymbol{n}\;dA\,, \tag{2.23}$$

with $\boldsymbol{n}$ the outward pointing surface normal on S and $\boldsymbol{\tau}$ the stress tensor in (2.22).

The total surface force on control volume V can be obtained by integrating all along its enclosing surface S

$$\boldsymbol{F}_s = \oint_S \boldsymbol{\tau}\cdot\boldsymbol{n}\;dA = \oint_S (-p\mathbf{I} + 2\,\mu\,\mathbf{S})\cdot\boldsymbol{n}\,dA\,. \tag{2.24}$$

Note that the volumetric deformation stress is excluded here as a result of the incompressible assumption and divergence free velocity field.

Body forces

Body forces are forces that originate from some external origin. The only body force that will be considered in this work is that of gravity, which will be denoted by $\boldsymbol{g}$. Unless stated otherwise, the earth's gravity field will be used

$$\boldsymbol{g} = -g\boldsymbol{j}\,, \tag{2.25}$$

with $g \approx 9.81\,m.s^{-2}$ the gravity acceleration constant and $\boldsymbol{j}$ the unit vector pointing upwards in the vertical direction.

The gravity body force $\boldsymbol{F}_b$ can be written [12, p.94]

$$\boldsymbol{F}_b = \int_V \rho\boldsymbol{g}\,dV\,, \tag{2.26}$$

for the fixed control volume V.

Line forces

Throughout this work the only line force that will be considered is that of surface tension on the interface between two immiscible fluids. Surface tension or capillarity is a result of intermolecular forces between fluid particles. Different molecular properties on opposite sides of the interface, result in a surface energy [81, p.38]

$$dE_\Gamma = \sigma d\Gamma \,, \tag{2.27}$$

with dE_Γ the surface energy of a differential interface segment $d\Gamma$ and σ the fluid property known as the surface tension coefficient. Since there is an energy on the interface, it requires work to deform it. This idea can be used to explain the line force: one has to apply a force to an interface element for it to change area. Therefore, surface tension is modelled at the continuum level as a line force acting per unit length of interface. For a detailed derivation of the surface tension force, refer to Tryggvason *et al.* [81, p.38-39]. The surface tension force $\boldsymbol{F}_\sigma$ on a segment of interface Γ, with edge contour C is given by

$$\boldsymbol{F}_\sigma = \oint_C \boldsymbol{\tau}_\sigma \cdot \mathbf{p} \; d\ell = \int_\Gamma \boldsymbol{\nabla} \cdot \boldsymbol{\tau}_\sigma \; dS \,, \tag{2.28}$$

with $\boldsymbol{\tau}_\sigma$ the surface stress tensor and $\mathbf{p}$ the vector normal to the edge C on the osculating plane. The force per unit area $\boldsymbol{f}_\sigma$ is obtained in the limit where the area of Γ goes to zero

$$\boldsymbol{f}_\sigma = \boldsymbol{\nabla} \cdot \boldsymbol{\tau}_\sigma = \sigma\kappa \boldsymbol{n}_\Gamma + \boldsymbol{\nabla}_\Gamma \sigma \,, \tag{2.29}$$

with $\boldsymbol{\nabla}_\Gamma$ the surface gradient and $\kappa = -\boldsymbol{\nabla}_\Gamma \cdot \boldsymbol{n}_\Gamma$ the curvature of Γ, [81, p.276]. Throughout this work a constant surface tension coefficient will be assumed, so that the last term in (2.29) equals zero and the force per unit area is simply

$$\boldsymbol{f}_\sigma = \sigma\kappa \boldsymbol{n}_\Gamma \,. \tag{2.30}$$

Applied to a control volume V, the line force for the research problem is

$$\boldsymbol{F}_\sigma = \int_\Gamma \sigma\kappa \boldsymbol{n}_\Gamma \, dA = \int_V \sigma\kappa\delta_\Gamma \boldsymbol{n}_\Gamma \, dV \,, \tag{2.31}$$

where the surface integral is converted to a volume integral using (2.10).

Summary

All the forces that will be considered in the research problem can now be substituted into (2.18), so that (2.17) becomes

$$\int_V \frac{\partial (\rho \boldsymbol{u})}{\partial t} \, dV + \oint_S \rho \boldsymbol{u} \, (\boldsymbol{u} \cdot \boldsymbol{n}) \; dA = \oint_S \boldsymbol{\tau} \cdot \boldsymbol{n} \; dA + \int_V \rho \boldsymbol{g} \; dV + \int_V \sigma\kappa\delta_\Gamma \boldsymbol{n}_\Gamma \, dV \,. \tag{2.32}$$

This is the general differential form of the conservation of linear momentum. The Boussinesq approximation and its effect on (2.32) will now be presented. If a fluid has a density ρ_0 at some reference temperature T_0, it is shown in [12, p.127] that the effect of density variation on inertial terms are small when the ratio of density variation, $\rho' = \rho - \rho_0$ to the actual density is small:

$$\frac{\rho'}{\rho_0} \ll 1 \,. \tag{2.33}$$

However, the effect of temperature variation is significant on the body force term, since the ratio ρ'/ρ_0 gets multiplied by the gravity. For small temperature variations a linear relationship between the density and temperature can be assumed

$$\rho = \rho_0 \left[1 - \beta \left(T - T_0\right)\right] , \tag{2.34}$$

with β the thermal expansion coefficient given by [32, p.564]

$$\beta = -\frac{1}{\rho}\left(\frac{\partial \rho}{\partial T}\right)_p . \tag{2.35}$$

Re-writing (2.32) with this approach yields

$$\int_V \frac{\partial \left(\rho_0 \boldsymbol{u}\right)}{\partial t}\, dV + \oint_S \rho_0 \boldsymbol{u}\left(\boldsymbol{u}\cdot\boldsymbol{n}\right)\, dA = \oint_S \boldsymbol{\tau}\cdot\boldsymbol{n}\, dA + \int_V \rho \boldsymbol{g}\, dV + \int_V \sigma\kappa\delta_\Gamma \boldsymbol{n}_\Gamma\, dV , \tag{2.36}$$

with ρ_0 the reference density defined earlier and ρ the temperature dependant density that is used in the body force term.

2.5.3 Conservation of Energy

The conservation of energy from the first law of thermodynamics states that the rate of change of energy inside a system must equal the total energy crossing the system control surface. The general convention for the direction of external energy transfer across system boundaries is heat transfer to the system or work performed by it on its surroundings. Internal heat generation (for example by nuclear fission) will not be considered in this work. For a fixed control volume, V, the first law of thermodynamics can be written with the fluid property $B = E$ and $\beta = e$ in (2.3), [88, p.172]

$$\begin{aligned} \left.\frac{dE}{dt}\right|_{sys} &= \dot{Q} - \dot{W} \\ \therefore \dot{Q} - \dot{W} &= \int_V \frac{\partial \left(\rho e\right)}{\partial t}\, dV + \oint_S \rho e \left(\boldsymbol{u}\cdot\boldsymbol{n}\right)\, dA , \end{aligned} \tag{2.37}$$

with $\dot{Q}$ and $\dot{W}$ respectively the rate of heat transfer and the rate of work performed. The signs of these terms are written according to the convention given above. The specific energy (per unit mass) is denoted e and is regarded as the sum of the specific internal and kinetic energies:

$$e = e_i + e_k = e_i + {}^1/_2 \boldsymbol{u}\cdot\boldsymbol{u} , \tag{2.38}$$

where e_i and e_k are respectively the specific internal and kinetic energies. Note that potential energy is excluded from e, but it will be included as the work performed by the gravity body force, as was also done in the derivations by [12] and [81]. If $\boldsymbol{q}$ is the heat transfer rate (or heat flux) per unit area, (2.37) can be written

$$\begin{aligned} &\int_V \frac{\partial \left(\rho e\right)}{\partial t}\, dV + \oint_S \rho e \left(\boldsymbol{u}\cdot\boldsymbol{n}\right)\, dA = \\ &\int_V \rho \boldsymbol{g}\cdot\boldsymbol{u}\, dV + \int_V \boldsymbol{\nabla}\cdot\left(\boldsymbol{u}\cdot\boldsymbol{\tau}\right)\, dV - \oint_S \boldsymbol{q}\cdot\boldsymbol{n}\, dA . \end{aligned} \tag{2.39}$$

The heat flux term has a negative sign, since surface normals are positive in the outward pointing direction by convention and therefore indicates an efflux.

Thermal energy conservation

The total energy conservation in V is given by (2.39) in integral form. For the numerical solution of flow problems, it is often useful to also derive the conservation equation of thermal energy. The conservation of thermal energy can be derived by first obtaining the conservation of mechanical energy and then subtracting it from the energy equation, (2.39). This is also the approach used in [12] and [81]. The mechanical energy equation can be obtained by taking the dot product of the velocity, $\boldsymbol{u}$, with the momentum conservation equation (2.32) and using the mass conservation equation to perform some algebraic manipulation. The result is [12, p.111]

$$\begin{aligned} &\int_V \frac{\partial\left(\rho e_k\right)}{\partial t}\, dV + \oint_S \rho e_k \left(\boldsymbol{u}\cdot\boldsymbol{n}\right)\, dA = \\ &\int_V \rho\boldsymbol{g}\cdot\boldsymbol{u}\, dV + \int_V \boldsymbol{u}\cdot\left(\boldsymbol{\nabla}\cdot\boldsymbol{\tau}\right)\, dV\,. \end{aligned} \tag{2.40}$$

The conservation of thermal energy is obtained [12, p.115] when mechanical energy (2.40) is subtracted from the total energy (2.39)

$$\int_V \frac{\partial \rho e_i}{\partial t}\, dV + \oint_S \rho e_i \left(\boldsymbol{u}\cdot\boldsymbol{n}\right)\, dA = -\int_V p\left(\boldsymbol{\nabla}\cdot\boldsymbol{u}\right)\, dV - \oint_S \boldsymbol{q}\cdot\boldsymbol{n}\, dA + \int_V \Phi\, dV\,, \tag{2.41}$$

where Φ is the viscous dissipation function given by

$$\Phi = 2\mu\ \mathbf{S}:\mathbf{S} - \frac{2}{3}\mu\left(\boldsymbol{\nabla}\cdot\boldsymbol{u}\right)^2\,. \tag{2.42}$$

The colon indicates tensor matrix multiplication $\mathbf{S}:\mathbf{S} = \mathrm{S}_{ij}\mathrm{S}_{ij}$. Kundu and Cohen [12, p.127], demonstrates how the Boussinesq approximation can be applied to the thermal energy equation (2.41). With the flow speeds low, it can be shown that viscous heating is negligible [12, p.128] by comparing the orders of magnitude of the viscous heating term to the change in thermal energy

$$\frac{\Phi}{\rho c_p\, {}^{DT}/_{Dt}} \approx \frac{2\mu\mathbf{S}:\mathbf{S}}{\rho c_p\, \boldsymbol{\nabla}\cdot\left(\boldsymbol{u}T\right)} \approx \frac{\mu\ {}^{U^2}/_{L^2}}{\rho_0 c_p\, U\, {}^{\delta T}/_{L}} = \frac{\nu U}{c_p\, \delta T\, L}\,, \tag{2.43}$$

where U, δT and L are respectively the characteristic velocity, temperature change and length scale in the flow. ν is the kinematic viscosity. For many practical flows, the resulting ratio is very small (10^{-7}, [12, p.128]) such that the viscous heating can be neglected.

The heat flux is modelled using Fourier's law

$$\boldsymbol{q} = -k\boldsymbol{\nabla}T\,, \tag{2.44}$$

with k the thermal conductivity. As for other properties before, the variations of k due to temperature is negligible and a constant value will be used for each phase.

The assumption of constant specific heats along with the assumption of ideal gas behaviour allows to combine the internal energy with the pressure work term to obtain a simplified version of (2.41). The derivation is shown in Appendix A and the result is

$$\int_V \frac{\partial\left(\rho c_p T\right)}{\partial t}\, dV + \oint_S \rho c_p T\boldsymbol{u}\cdot\boldsymbol{n}\, dA = \oint_S k\boldsymbol{\nabla}T\cdot\boldsymbol{n}\, dA\,. \tag{2.45}$$

This is the final conservative, integral form of the conservation of thermal energy that will be used in this work.

2.6 Summary

In this section, the general conservation of mass, momentum and energy was derived for an generic control volume. The integral form of each equation was presented, which forms the basis for the numerical implementation.

For the flows in this work, the Boussinesq approximation is applicable. The summary of this approach from Kundu and Cohen [12, p.128] was used to present the simplified versions of the governing equations. The approximation is accurate, since the flow speed is small relative to the sound speed in the fluid. Temperature changes are also relatively small and the effect of variations in density is applied on the body force term, but is negligible elsewhere. Under these assumptions, the viscosity, heat capacities and thermal conductivity in each phase are considered constant. The resulting equations from mass, momentum and energy are

$$\begin{aligned}
\int_V \frac{\partial \rho_0}{\partial t}\, dV + \oint_S \rho_0 \left(\boldsymbol{u}\cdot\boldsymbol{n}\right)\, dA &= 0 \\
\int_V \frac{\partial \left(\rho_0 \boldsymbol{u}\right)}{\partial t}\, dV + \oint_S \rho_0 \boldsymbol{u} \left(\boldsymbol{u}\cdot\boldsymbol{n}\right)\, dA &= \oint_S \boldsymbol{\tau}\cdot\boldsymbol{n}\, dA + \int_V \rho \boldsymbol{g}\, dV + \int_V \sigma\kappa\delta_\Gamma \boldsymbol{n}_\Gamma\, dV \\
\int_V \frac{\partial \left(\rho_0 c_p T\right)}{\partial t}\, dV + \oint_S \rho_0 c_p T (\boldsymbol{u}\cdot\boldsymbol{n})\, dA &= \oint_S k \boldsymbol{\nabla} T \cdot \boldsymbol{n}\, dA\,.
\end{aligned} \tag{2.46}$$

Here ρ_0 is the constant density in each phase at some reference temperature T_0. The density ρ in the gravity term is calculated using

$$\rho = \rho_0 \left[1 - \beta \left(T - T_0\right)\right]\,, \tag{2.47}$$

with β the thermal expansion coefficient as defined before.

Further problem specific simplifications will be applied once the individual problems are introduced in Parts I and II.

Chapter 3

The PARIS code

The numerical methods that will be used in this work are all added to an existing code called PARIS . PARIS is an acronym for **PA**rallel **R**obust **I**nterface **S**imulator. It is an open-source code distributed under the GNU general public license. It solves the incompressible Navier–Stokes equations for multi-phase flow using one-fluid formulation, as described in [81] and mentioned in section 2.4.2. Interface capturing is handled with either a volume-of-fluid (VOF) [30] or front tracking [82] approach. In this work the VOF approach will be used, of which the numerical methods for the VOF advection and surface tension terms are largely based on the SURFER [37] and GERRIS [45, 46] codes. The code can be run in parallel by decomposing the domain into smaller subdomains using the MPI libraries [22]. The code has a web page at `http://parissimulator.sf.net`.

In this chapter the code will be presented. First, the numerical grid used to solve the governing equations presented in the previous chapter will be introduced. This is important detail, as the novel numerical techniques developed here are applied specifically in this existing framework. Details of the time integration and calculation of several terms in the governing equations will then be provided.

3.1 Computational grid

A numerical solution is obtained by solving the system of governing equations at discrete spatial locations for a specific instant in time. The solution space in which the problem is solved, whether it has two (2D) or three (3D) spatial dimensions, is referred to as the domain. The solution is obtained at certain discrete locations throughout the domain. These locations are formed by sub-dividing the domain into smaller volumes and then integrating the governing equations in these volumes. This process is commonly referred to as the finite volume method [83].

In PARIS and for this work, orthogonal domains are used exclusively which are subdivided into squares (2D) or cubes (3D). These squares or cubes are known as elements, computational cells or finite volumes. Henceforth they will be referred to as *cells*. By sub-dividing the domain into cells, one obtains what is commonly referred to as the computational mesh or grid. Fig. 3.1 shows a 3D domain with some of the nomenclature that will be used throughout this work. On the right hand side a 2D cut shows a 3×3 stencil with the location of variables in the cell.

For the purpose of discretizing the equations presented in the previous chapter the same type of grid will be used, sometimes referred to as the marker-and-cell (MAC) grid from the method developed by Harlow and Welch [26]. The grid is also known as a staggered grid, since discrete velocity components are located on the cell faces, while other scalar variables — like pressure,

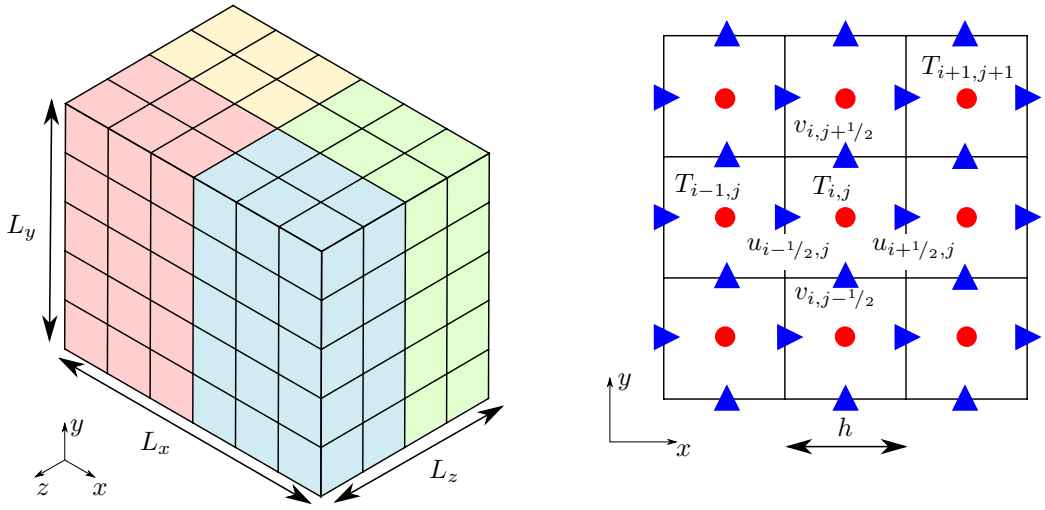

Figure 3.1: Schematic representation of a 3D flow domain on the left of dimension $L_x \times L_y \times L_z$. The domain is subdivided into $N_x \times N_y \times N_z$ cells. A typical domain decomposition for parallel processing is illustrated by the different shaded regions on the grid. Note that the amount of cells here serves as an illustration and typically a single processor domain will contain 32×32 cells, or more. On the right a 2D cut shows 3×3 computational cells with normal velocity components located on cell faces. Scalar components, like temperature T shown here, are located at cell centres.

VOF and temperature — are located at cell centres. Computational cell edges have identical lengths, which will be called h throughout this work.

3.2 Existing numerical method in PARIS

As a basis for the novel numerical methods that will be used later, a brief background on the existing numerical method used in PARIS will be given. The modifications required for the specific problems in this work will be presented as the respective problems are introduced in Parts I and II.

3.2.1 Governing equations

The existing method solves the incompressible mass conservation equation as well as the conservation of linear momentum. It uses a one-fluid formulation and includes surface tension at the interface between two-fluids that are immiscible. The resulting equations are exactly those derived in the previous chapter, but without a temperature dependent density in the gravity term of the momentum equation

$$\boldsymbol{\nabla} \cdot \boldsymbol{u} = 0 \tag{3.1a}$$

$$\rho \left(\frac{\partial \boldsymbol{u}}{\partial t} + \boldsymbol{u} \cdot \boldsymbol{\nabla} \boldsymbol{u} \right) = -\boldsymbol{\nabla} p + \boldsymbol{\nabla} \cdot (2\mu \mathbf{S}) + \rho \boldsymbol{g} + \sigma \kappa \delta_s \boldsymbol{n_s} \tag{3.1b}$$

with $\boldsymbol{u}$, ρ, p and μ respectively the fluid velocity, density, pressure and viscosity. The body force vector is given by $\boldsymbol{g}$ and $\mathbf{S}$ is the deformation (or strain rate) tensor such that $\mathrm{S}_{ij} = \frac{1}{2}\left(\frac{\partial u_i}{\partial x_j} + \frac{\partial u_j}{\partial x_i}\right)$. The last term is used to include capillary effects with the continuum surface force approach [6]. σ and κ are respectively the surface tension and interface curvature with δ_s a dirac function for the interface position and $\boldsymbol{n_s}$ the surface normal on the interface.

Immiscible phases are distinguished by using either the VOF method or front tracking. In this work we use the VOF method. The VOF scalar c, as its name suggests, indicates the volume-of-fluid of some reference fluid contained inside some control volume V_c. It can be defined mathematically by using the Heaviside function to track the reference phase. The VOF scalar c is then

$$c = \frac{1}{V_c}\int_{V_c} H\left(\boldsymbol{x}, t\right)\, dV\,. \tag{3.2}$$

From the equation above, it can be deduced that $0 \leq c \leq 1$. For V_c completely filled by the reference, or tracked fluid $c = 1$ and $c = 0$ when there is no reference fluid inside V_c.

The VOF scalar adheres to an advection equation

$$\frac{\partial c}{\partial t} + \boldsymbol{\nabla}\cdot(c\boldsymbol{u}) = 0\,. \tag{3.3}$$

The one-fluid density and dynamic viscosity inside a cell are determined as a volume weighted average of c. The simple arithmetic average or the harmonic mean can also be used. The simple arithmetic average for the density and viscosity is respectively given by

$$\rho(c) = \rho_2 c + (1-c)\rho_1 \tag{3.4a}$$
$$\mu(c) = \mu_2 c + (1-c)\mu_1 \tag{3.4b}$$

with the subscripts indicating the fluid parameters for a specific phase. In this case the tracked phase is phase 2. The choice of tracked phase If required, filtering is available to smooth the VOF field. However, this will not be used in this work.

3.2.2 Numerical method

The above system of equations is solved numerically using a projection method [11]. Time integration can be done using an explicit first order or a second order Crank–Nicolson type scheme. The following equations will be given in discrete form for an explicit first order time integration, to illustrate the numerical procedure.

It is assumed that the velocity field adheres to (3.1a). First, the VOF scalar is advected

$$\frac{c^{n+1} - c^n}{\Delta t} + \boldsymbol{\nabla}^h\cdot(c^n\boldsymbol{u}^n) = 0\,, \tag{3.5}$$

with $\boldsymbol{\nabla}^h$ the discrete gradient operator and Δt the time step size. This equation is solved in two steps: reconstruction of the interface as a plane in each grid cell and then its advection with the computation of the reference phase fluxes across the cell boundary. The use of planes to reconstruct the interface is accredited to de Bar [14]. In the first part of the reconstruction step, the interface normal $\boldsymbol{n}_s$ is computed with the "mixed Youngs-centered" (MYC) method [3]. Then the position of a plane, representing the interface in the cell, is determined using elementary geometry [55]

$$\boldsymbol{n}_s\cdot\boldsymbol{x} = n_{sx}x + n_{sy}y + n_{sz}z = \alpha\,, \tag{3.6}$$

where the scalar α characterizes the position of the interface. For the computation of the reference phase fluxes we can use the Lagrangian explicit CIAM scheme [39] or the strictly conservative Eulerian scheme of Weymouth and Yue [87].

The fluid density and viscosity field can now be updated

$$\begin{aligned} \rho^{n+1} &= \rho_2 c^{n+1} + (1 - c^{n+1})\rho_1 \\ \mu^{n+1} &= \mu_2 c^{n+1} + (1 - c^{n+1})\mu_1 \end{aligned} \tag{3.7}$$

The momentum equation is split into two steps. First, a temporary velocity $\boldsymbol{u^*}$ is obtained by taking into account the viscous and surface tension forces

$$\rho^n \left(\frac{\boldsymbol{u}^* - \boldsymbol{u}^n}{\Delta t} + \boldsymbol{u}^n \cdot \boldsymbol{\nabla}^h \boldsymbol{u}^n \right) = \boldsymbol{\nabla}^h \cdot (2\mu^n \mathbf{S}) + \rho^n \boldsymbol{g} + (\sigma \kappa \delta_s \boldsymbol{n})^{n+1} \,, \tag{3.8}$$

The advection term $\boldsymbol{u} \cdot \boldsymbol{\nabla} \boldsymbol{u}$ is discretised in a standard fashion for staggered grids using a choice of schemes, including ENO [27], QUICK [38] and WENO [59]. The diffusion term can be calculated explicitly ($\mu^n \mathbf{S}^n$) or implicitly ($\mu^{n+1} \mathbf{S}^{n+1}$).

The second step of the momentum equation is written by including the contribution of the pressure term:

$$\frac{\boldsymbol{u}^{n+1} - \boldsymbol{u}^*}{\Delta t} = -\frac{1}{\rho^{n+1}} \boldsymbol{\nabla}^h p^{n+1} \,. \tag{3.9}$$

The continuity equation requires that

$$\boldsymbol{\nabla}^h \cdot \boldsymbol{u}^{n+1} = 0 \,. \tag{3.10}$$

By taking the divergence of (3.9) and using this equation, a Poisson equation is obtained relating the pressure and predicted velocities:

$$\boldsymbol{\nabla}^h \cdot \left[\frac{\Delta t}{\rho^{n+1}} \boldsymbol{\nabla}^h p^{n+1} \right] = \boldsymbol{\nabla}^h \cdot \boldsymbol{u}^* \,. \tag{3.11}$$

The sequence for each time step will be to first solve (3.8) to obtain the temporary velocity field $\boldsymbol{u^*}$. The pressure is found by solving the Poisson equation (3.11). The temporary velocity field is then corrected with the pressure in (3.9) to satisfy (3.10) for the velocity at the next time step $\boldsymbol{u^{n+1}}$.

The user has at his/her disposal a method based on the trapezoidal rule of integration to increase the convergence order of time integration. This method computes two consecutive, explicit time steps for each variable, after which the final value is halved. This is similar to the technique presented in [81, p.53] and applied by [19, 71]. Let us consider for example the velocity field, $\boldsymbol{u}$:

$$\begin{aligned} \boldsymbol{u}^* &= \boldsymbol{u}^n + \Delta t \, \mathfrak{L}(\boldsymbol{u}^n) \\ \boldsymbol{u}^{**} &= \boldsymbol{u}^* + \Delta t \, \mathfrak{L}(\boldsymbol{u}^*) \\ \boldsymbol{u}^{n+1} &= \frac{1}{2}(\boldsymbol{u}^{**} + \boldsymbol{u}^n) \,, \end{aligned} \tag{3.12}$$

where Δt indicates a discrete time step and $\mathfrak{L}$ is some linear operator that represents the spatial discretization of the governing equations. The intermediate results produced by explicit time marching is indicated by a * superscript.

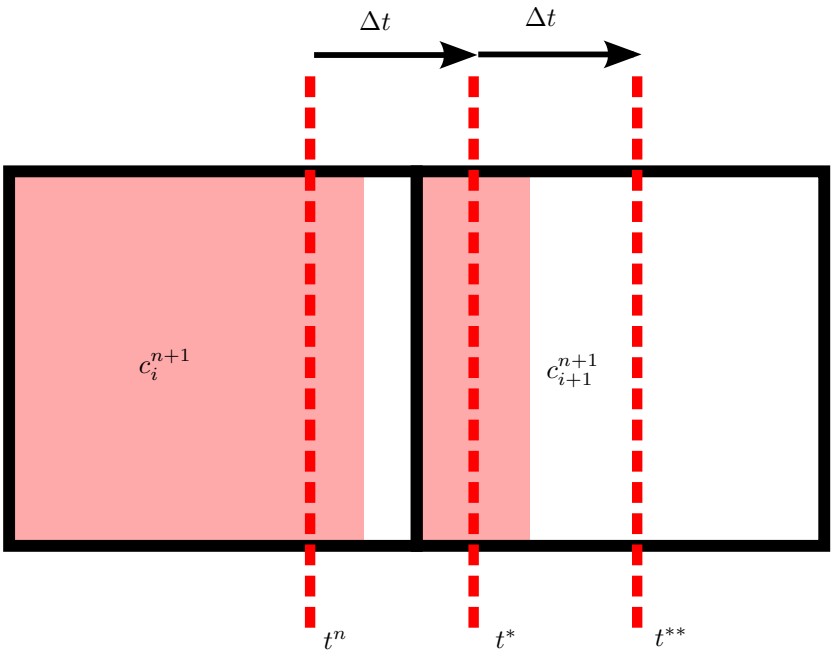

Figure 3.2: Illustration of artificial gap that forms in the tracked phase when the higher order time scheme is used. A uniform velocity advects the interface from left to right. The interface position is indicated with the dashed red line at time steps n, $*$ and $**$. The resulting VOF values in the respective cells are shown after the discrete values are halved.

It should be noted that when this method of time integration is applied in conjunction with VOF, there are sometimes artificial gaps formed in the tracked phase. This can be illustrated with a simple one dimensional test problem. In Fig. 3.2.

In this illustration, a uniform velocity advects the VOF function from left to right. The resulting interface positions are shown as dashed lines after two consecutive explicit time steps. The shaded regions indicate the resulting VOF values after the respective halving operation $c_i^{n+1} = {}^1\!/_2(c^{**} + c^n)$ is done. The result is the remainder of the opposite phase in the right of the cell on the left, i. In general, this may disappear after a few time steps as the flow advects it out, but will cause problems when the plane reconstruction is used to determine the location of the phase interface and is used for calculations there.

3.3 Summary

This chapter provided an introduction to PARIS . More developments to the code will be presented in the numerical method chapters in Parts I and II.

Part I

Bubble clouds in cavitation

Chapter 4

Introduction: Part I

This chapter will introduce the problem that will be studied in Part I of this work. The background on the process of micro-spall failure will be provided along with examples of some of the research that has been undertaken to study it. This research includes theoretical modelling and experimental studies.

Cavitation is the process when a liquid changes phase and becomes a vapour. It is similar to boiling, but instead of a temperature increase causing phase change, it occurs due to a pressure decrease sufficient for the system pressure to fall below the saturated vapour pressure, [7]. A classical example of cavitation is the tip vortex in ship propellers [88, p.34] or the formation and collapse of cavitating bubbles in pump rotors [7].

The process of cavitation plays an important role in the failure of materials during micro-spall [61]. A brief introduction on cavitation and related numerical studies will be given. To better understand the complex process of micro-spall, a model problem will be defined. This problem aims to provide more insight into one of the aspects of micro-spall.

A hypothesis will be made and some research questions will be posed, which will form the guideline for the study in Part I. The method to investigate the model problem will be introduced.

4.1 Background

4.1.1 Micro-spall

Micro-spall refers to a specific type of spallation fracture when fragmentation occurs in parts of a material that has already been melted during shock loading [61]. Andriot [2] is cited by Signor [60, 61] as the first to have used the term *microspalling*.

One way of studying micro-spall is by conducting experiments. Typically, some material sample is subjected to projectile impact [62, 66] or laser irradiation [13, 63]. The micro-spall process is described by Signor [61]: Dynamic stress loading on material samples create a compression wave that propagates through it. Upon reflection from the free surface of the sample, tensile stresses are created in the material that cause the nucleation of cavities. These cavities may grow up to coalescence and lead to fine droplets of melted material being formed as the material fails catastrophically, [60]. A schematic representation of this process is taken from [62] and shown in Fig. 4.1.

Micro-spall has also been the topic of diverse theoretical investigations. Stebnovskii have conducted several investigations, including the formation conditions for vapour bubbles during cavitation [68], a shear deformation model [70] and a rheological model of the media during

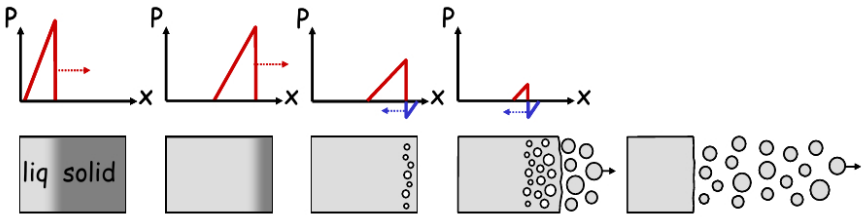

Figure 4.1: A schematic representation of the micro-spall process, taken from [62]. A compression wave is shown by the pressure plot at the top and moves from left to right through the material sample. As the wave reaches the free surface on the right, it is reflected and vapour bubbles are nucleated from the resulting tension in the material. If bubbles grow sufficiently large to percolation, droplets are formed that get ejected by the residual momentum in the material post shock.

cavitation [69]. Numerical simulations have also been conducted, like the study conducted by Durand and Soulard [17] on the properties of ejecta using molecular dynamics.

In this work, the focus will be on the cavitation process inside the melted material. Cavitation has been identified as a key aspect [61] that leads to the failure of a sample undergoing micro-spall.

4.1.2 Cavitation and bubble interactions

In [61], Signor proposes a hollow sphere model to investigate the dynamics of cavities. Typical liquid dilatation rates for typical shock loading times are applied to the hollow sphere model and the evolution of the total porosity is studied. The main question he poses is whether the kinetic energy transferred to the liquid from the loading is sufficient to lead to percolation. The kinetic energy is dissipated by viscous forces and increasing surface energy in the vapour bubbles due to surface tension. It is this competition that forms the basis for the problem that will be studied here.

4.2 Problem definition

In this section the model problem will be introduced. A simplified model of the actual dilatation process will be proposed with the underlying assumptions made to model the flow.

4.2.1 Model problem

The problem considered here will be the dynamics of vapour bubbles contained in a liquid that is subjected to a tensile stress, resulting in expansion of the flow volume. A three dimensional domain will be considered. The liquid will be assumed incompressible and, additionally, a perfect fluid will be assumed so that viscous effects will not be accounted for. A physical argument for this will be presented later in the text. Surface tension at the vapour-liquid boundary will be accounted for, as this will be the main mechanism resisting expansion of vapour bubbles in the expanding liquid. Thermal effects are not considered in this idealized problem and the carrier fluid density and surface tension coefficient are treated as constants. The effect of gravity is considered negligble.

The nucleation process will not be modelled. Instead, small spherical vapour bubbles will be initialised in the carrier liquid. As a first step towards modelling the tensile loading on the material, a constant rate of expansion in the liquid will be assumed.

4.2.2 Method of investigation

The method that will be used to investigate the problem is numerical simulation. Direct numerical simulation (DNS) has been an increasingly popular method of studying two-phase flows [54, 80]. For multi-phase DNS in general some interface tracking or capturing method is employed, which determines the fluid density and viscosity by a tracked indicator function.

In our problem we cannot apply the incompressible assumption to both phases, as the cavitation process causes gas bubbles to change in volume. One approach is to indeed solve an additional energy equation and then use the temperature field to calculate the mass transfer at the interface between the two otherwise incompressible, immiscible fluids [79]. The mass transfer between the fluids results in a volume source at the interface. This will be the method that will be applied in Part II of this work to study boiling. In this part, however, temperature effects are neglected and a different approach will be applied to model the cavitation process.

The approach that will be used on the micro-spall model problem is to assume an incompressible liquid, where mass and momentum conservation are enforced by the incompressible Navier-Stokes equations. The gas phase, however, is left unsolved. Instead, a free-surface condition is applied on the interface and the gas phase only effects the flow through its pressure. This is an accurate approach when the density ratio is high and has been used extensively. More details on this approach will be given in the next chapter.

An early example of a numerical simulation using a free surface approach is the marker code of Harlow and Welch [26] and a modified version of this code to study water waves [10]. An example of an industrial application of this approach is the study of the ink ejection process in an inkjet printer head [75]. The next section will give an overview of previous work on numerical simulations on bubble clouds or vapour bubble collapse during cavitation.

4.2.3 Previous work

Bubble clouds during cavitation or its interactions with shocks have been the topic of investigation in several theoretical studies employing mathematical models. A prominent example is the study of pressure wave propagation in liquids filled with bubbles in the dilute limit by Watanabe and Prosperetti [84]. Another example is the study by Fuster *et al.* [21], where the interaction between bubble clouds and a carrier liquid under tension is investigated from the perspective of the potential energy in the system. There are several other theoretical investigations, but this work will adopt a DNS approach. Examples of three dimensional DNS studies on bubbles are relatively rare, compared to theoretical investigations.

Studies on single bubbles have been performed using different interface tracking techniques. Popinet used marker particles to study the collapse of vapour bubbles [47] in an incompressible liquid. He also used a free surface approach to model vapour bubbles and studied the effect that viscosity has on the formation of jets during bubble collapse. A combined level set and VOF method (CLSVOF) was developed by Sussman [71], which he showed to have second order convergence in space and time. Can and Prosperetti [8] used a level set method and studied the evolution of a vapour bubble in a microtube.

A DNS study of the propagation of shock waves in an incompressible liquid containing multiple compressible gas bubbles was performed by Delale *et al.* [15] using front tracking to capture the liquid-vapour interface. In terms of high performance computing, Rosinelli *et al.* [48] performed

a very large simulation on the collapse of vapour bubbles. A numerical grid of 13×10^{12} grid points was used to simulate the collapse of around 15000 bubbles. This was a study focussing on high performance computing aspects of CFD and, however impressive it is, it presented very limited results of the flow physics and the details of the boundary conditions were not mentioned. Additionally, no capillary effects were included in the governing equations.

This study will similarly use a free surface approach to model multiple, compressible bubbles in an incompressible carrier liquid. It will use a VOF method, coupled with the PLIC interface representation to, for the first time, study the capillary effects on bubble clouds in a liquid under tension.

4.2.4 Research hypothesis

When pre-nucleated bubbles in an incompressible and inviscid carrier liquid are exposed to a constant volumetric expansion, a bubble competition will appear between the bubbles as a result of capillary effects.

4.2.5 Research questions

The main research questions for this part of the work include:

1. How can the model problem be solved numerically?
2. Is there observable competition between bubbles in a bubble cloud under conditions described in the model problem?
3. Can a correlation be drawn to characterise bubble competition?

The next section will provide the mathematical formulation for the problem.

Chapter 5

Mathematical Formulation

5.1 Introduction

In this chapter, the mathematical formulation for the problem described in 4.2.1 will be presented. A free surface approach will be adopted, which will be detailed in the next section. Thereafter a control volume analysis will be performed to derive the governing equations. Simplifying assumptions will be introduced as the equations are derived. The general equations for conservation of mass and momentum from chapter 2.5 will be used as a basis, with some additional simplifications.

5.1.1 Free surface approach

As explained in the introduction, a free surface approach will be adopted to model the vapour cavities in the problem. The free surface boundary condition is a typical boundary condition applied to flows with interfaces, [88, p.246]. The idea is to allow the interface to move freely. The flow in only one phase — the carrier phase — is solved according to the governing equations that apply to it.

The flow in the opposite phase, however, is not considered. Instead, the pressure in the unresolved phase is assumed to be constant in space and is applied as a Dirichlet boundary condition at the interface to the carrier phase. This unresolved phase will henceforth be referred to as the cavity. An example is the study of oceanic flows, where the interface between the ocean and the atmosphere is regarded as a free surface. The atmospheric pressure is applied as a boundary condition to the flow in the ocean.

An important consideration for the purpose of this work is that surface tension can still be accounted for when using a free surface approach. The pressure jump caused by capillarity can be added to the pressure in the cavity. This pressure jump is sometimes referred to as the Laplace pressure jump. Let the pressure in the carrier fluid be p_ℓ and the pressure in the opposite phase p_c. The pressure jump at the interface due to surface tension can be shown to be [12, p.9]

$$p_\ell - p_c = \sigma \left(\frac{1}{R_1} + \frac{1}{R_2} \right) = \sigma\kappa \,. \tag{5.1}$$

Here the principle radii of curvature of the interface surface are denoted R_1 and R_2, σ is the surface tension coefficient and κ is the mean curvature. Note that the curvature is calculated here with the normal pointing from the liquid phase into the unsolved phase. A bubble in

the neglected phase will have a higher pressure than the liquid, since the curvature will have a negative sign in (5.1).

5.1.2 Control volume definition

A specific control volume for the free surface problem will be introduced here. Similar to the control volume analysis presented earlier, the governing equations can then be derived by considering the rate of change of fluid properties inside this control volume.

The control volume for the problem is shown in Fig. 5.1. It shows a liquid volume V_ℓ , that is bounded by a free surface Γ and a control surface S_ℓ. The carrier fluid velocity field, $\boldsymbol{u} = u\boldsymbol{i} + v\boldsymbol{j} + w\boldsymbol{k}$, is assumed continuous, with $\boldsymbol{i}, \boldsymbol{j}, \boldsymbol{k}$ the respective unit vectors in directions x, y, z in a standard Cartesian coordinate system.

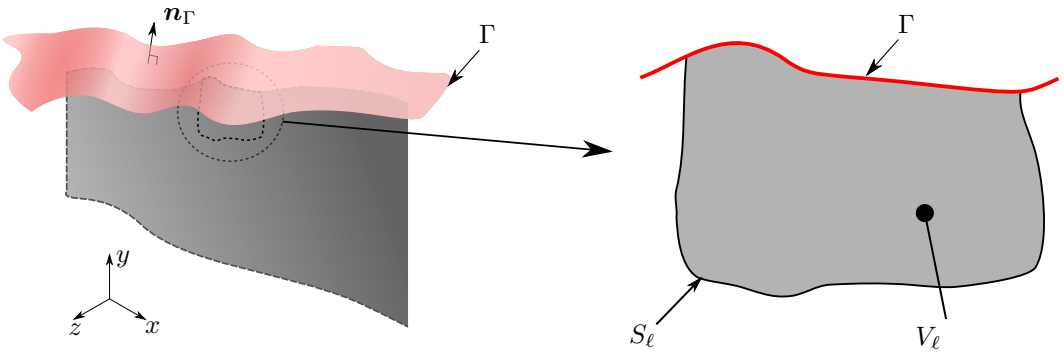

Figure 5.1: The control volume under consideration in Part I is shown on the left with the free surface Γ in red shading. The liquid carrier phase is shown in grey on an arbitrary plane. A normal projection on this plane is shown on the right to indicate the liquid control volume V_ℓ, bounded by a fixed control surface S_ℓ and the free surface Γ.

The free surface, Γ is a material boundary moving with the carrier fluid. The control surface S_ℓ has an outward pointing normal $\boldsymbol{n}$. An important convention that will be used in the remainder of Part I is that the control surface S_ℓ – which is a boundary to V_ℓ – is a surface parallel to the interface on the liquid side of it at an infinitesimal distance. Practically this means that the pressure on the boundary S_ℓ is the static pressure in the liquid with the Laplace pressure jump across the interface already accounted for.

5.2 Governing equations

The governing equations for the liquid will be presented here, from the derivation in section 2.5 and including some simplifying assumptions.

5.2.1 Mass conservation

The incompressible mass conservation equation was derived in chapter 2. The difference here is that the equation will only be applied in the liquid volume. The conservation of mass in V_ℓ can be written

$$\frac{d}{dt}\left(\int_{V_\ell}\rho\,dV\right)+\oint_S\rho\,(\boldsymbol{u}_r\cdot\boldsymbol{n})\;dA=0 \tag{5.2}$$

In the last term $\boldsymbol{u}_r=\boldsymbol{u}-\boldsymbol{u}_S$ is the relative velocity between the fluid and the control surface S, which consists of the control surface S_ℓ and the free surface Γ. With Γ a material surface and S_ℓ fixed, the flux term can be written

$$\oint_S\rho\,(\boldsymbol{u}_r\cdot\boldsymbol{n})\;dA=\int_{S_\ell}\rho\,(\boldsymbol{u}\cdot\boldsymbol{n})\;dA\,, \tag{5.3}$$

since there is no flux across the free surface. The volume integral can be written as the sum of a the rate of change of mass inside a volume frozen in time and the flux out of it as the material boundary moves. This is similar to the rate of change of some property in a material volume, derived in [12, p.84]

$$\frac{d}{dt}\left(\int_{V_\ell}\rho\,dV\right)=\int_{V_\ell}\frac{\partial\rho}{\partial t}\,dV+\int_\Gamma\rho\,(\boldsymbol{u}\cdot\boldsymbol{n}_\Gamma)\;dA\,. \tag{5.4}$$

Substituting (5.3) and (5.4) into (5.2) and applying the the incompressible assumption (with thermal effects neglected), the same continuity equation is obtained as earlier, which is valid everywhere in the carrier phase

$$\boldsymbol{\nabla}\cdot\boldsymbol{u}=0\,. \tag{5.5}$$

5.2.2 Momentum conservation

The momentum conservation derived in Chapter 2, (2.32) will be used here as a starting point. For the model problem no thermal effects will be considered and body forces are regarded as negligible. Viscous effects will also be neglected here. This is motivated by the relatively small Ohnesorge number encountered in micro-spall experiments with Tin samples. Typical Tin samples have a thickness of the order of $100\mu m$. If the length scale of the small debris in Laser irradiation and plate impact experiments were to be considered as a reference length, $L\approx 10\mu m$ [62], the Ohnesorge number, Oh is

$$Oh=\frac{\mu}{\sqrt{\rho\sigma L}}=5.5\times10^{-3} \tag{5.6}$$

with $\mu=10^{-3}\ Pa.s$, $\rho=6.5\times10^3\ kg.m^{-3}$ and $\sigma=0.5\ N.m^{-1}$ the dynamic viscosity, density and surface tension of liquid Tin.

The resulting momentum conservation equation in the liquid is then

$$\frac{\partial\boldsymbol{u}}{\partial t}+\boldsymbol{u}\cdot\nabla\boldsymbol{u}=-\frac{\nabla p}{\rho}\,, \tag{5.7}$$

with ρ and $\boldsymbol{u}$ respectively the liquid density and velocity. p is the pressure in the liquid. Note that the surface tension term is excluded here. The reason is that it is included in the boundary condition on the free surface. The pressure of the unresolved phase can be determined from an equation of state. In this case adiabatic conditions are assumed and a polytropic gas law is applied [74] to define the pressure of the cavity phase

$$p_c=p_0\left(\frac{V_0}{V_c}\right)^\gamma\,, \tag{5.8}$$

where V_c is the total volume of the cavity at pressure p_c. p_0 and V_0 are the respective reference pressure and volume of the cavity phase and γ is the heat capacity ratio.

Surface tension is accounted for at the free surface through the pressure jump caused by it. If p_s is the pressure at the free surface on the liquid side, this is related to the cavity pressure using (5.1)

$$p_s = p_c + \sigma\kappa\,, \tag{5.9}$$

where σ is the surface tension coefficient, assumed to be constant. The interface curvature is given by κ. The interface is captured using a volume-of-fluid [30] approach, that considers a *colour* function, c. This function c represents the volume fraction or volume-of-fluid of a reference phase present in the spatial domain. For control volume V_ℓ, c is then given by

$$c = \frac{1}{V_\ell}\int_{V_\ell} H\left(\boldsymbol{x}, t\right)\, dV \tag{5.10}$$

where $H\left(\boldsymbol{x}, t\right)$ is the Heaviside function, satisfying $H = 1$ inside the carrier phase and $H = 0$ outside.

The VOF scalar c is governed by the following advection equation

$$\frac{\partial c}{\partial t} + \nabla \cdot \left(c\,\boldsymbol{u}\right) = 0\,. \tag{5.11}$$

Chapter 6

Numerical Method

The computational grid in PARIS was introduced in 3.1. The governing equations presented in the previous chapter are discretized on this equi-spaced Cartesian mesh in the so-called MAC arrangement [26]. Scalar values (p and c) are located in the center of computational cells, while scalar components of velocity are located on cell faces.

The above system of equations is solved numerically using the same projection method [11] introduced in 3.2.2. There are a few differences in how the method is applied and in the numerical approximation of some of the terms. The first main difference is that only the liquid phase is solved. Another difference is that the continuum surface force method to calculate the surface tension term is not included in the first step of the projection method in (3.8). The pressure gradient is instead modified in (3.11) to include the effect of surface tension at the interface. This will be detailed in the following section.

6.1 Treatment at the free surface

At the interface to the cavity phase, a Dirichlet boundary condition for the pressure needs to be applied to include the effects of the cavity pressure and surface tension on the liquid flow. The method used in this work is inspired by the idea of Fedkiw and Kang [20, 34], often referred to as the ghost fluid method. First, the cavity pressure is found from (5.8). In this equation, p_0 and V_0 are known gas quantities. The volume V needs to be found in order to allow for the correct application of (5.8) in each individual cavity.

This is done by identifying continuous volumes of gas inside the domain using the colour function, c and a numerical algorithm based on the work by Herrmann [28]. A viral tagging procedure is used to mark computational cells containing the desired phase, after which connected cells are agglomerated into a single volume. The procedure is compatible with domain decomposition in parallel processing.

With the value of p_c calculated for each cavity, special care is required in the discretization of (3.11) for liquid cells near the interface. Cells that contain mostly gas are simply excluded from the solution, so that only cells where $c < 0.5$ are solved, with $c = 0$ in the liquid.

Fig. 6.1 shows a representation of a 2D grid with a section of an interface. The grey area represent a vapour-filled cavity. Cells that contain a filled circle are included in the pressure solution, while cells without a marker are excluded. The finite volume discretisation of the left

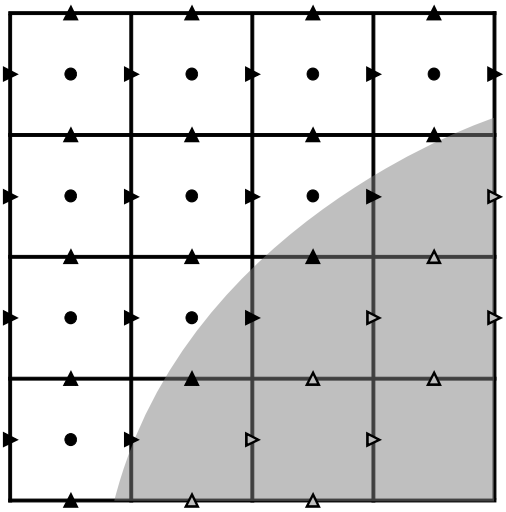

Figure 6.1: A 2D section of the numerical grid, showing part of a gas bubble in grey. Circles represent computational cell nodes, where pressure is calculated. Triangles indicate scalar velocity components on the computational cell faces. Filled triangles indicate values which are found by solving the governing equations, while unfilled triangles represent boundary values found by extrapolation.

hand side of (3.11) for a bulk liquid cell in 2D, shown in Fig. 6.2a is written

$$\begin{aligned}
&\frac{\Delta t}{V_{i,j}} \int_{V_{i,j}} \boldsymbol{\nabla} \cdot \left[\frac{\boldsymbol{\nabla}^h p^{n+1}}{\rho} \right] dV \\
&\approx \frac{\Delta t}{\rho} \left(\frac{\nabla_y^h p_{i,j+1/2} - \nabla_y^h p_{i,j-1/2}}{\Delta y} + \frac{\nabla_x^h p_{i+1/2,j} - \nabla_x^h p_{i-1/2,j}}{\Delta x} \right) \\
&= \frac{\Delta t}{\rho} \frac{p_{i,j+1} + p_{i,j-1} + p_{i+1,j} + p_{i-1,j} - 4p_{i,j}}{h^2} \,,
\end{aligned} \tag{6.1}$$

where the i and j subscripts are integer indices for the discrete computational cell with volume $V_{i,j}$. Since the equation above is only applied in the liquid phase and by neglecting thermal effects, the liquid density is assumed constant. Furthermore, for cubic cells $\Delta x = \Delta y = \Delta z = h$, where h is the constant grid spacing.

The stencil for the pressure gradient components has to be changed near the interface when a neighbouring pressure in expression (6.1) falls inside the gas phase. This point must be disregarded and its pressure substituted by a surface pressure. We apply the same approach as Chan [10]. As an example, the approximation for the pressure gradient components for the cell with indices i and j in Fig. 6.2b is written

$$\boldsymbol{\nabla}_x^h p_{i+1/2,j} = \frac{p_{s,i+1,j} - p_{i,j}}{\delta_{i+1/2,j}} \;; \quad \boldsymbol{\nabla}_y^h p_{i,j-1/2} = \frac{p_{i,j} - p_{s,i,j-1}}{\delta_{i,j-1/2}} \,, \tag{6.2}$$

where δ is the distance between the pressure node under consideration and the intersection with the interface. The pressure p_s on the liquid side of the interface is found by adding to p_c the Laplace pressure jump. The pressure p_c inside each cavity is known from (5.8). The interface

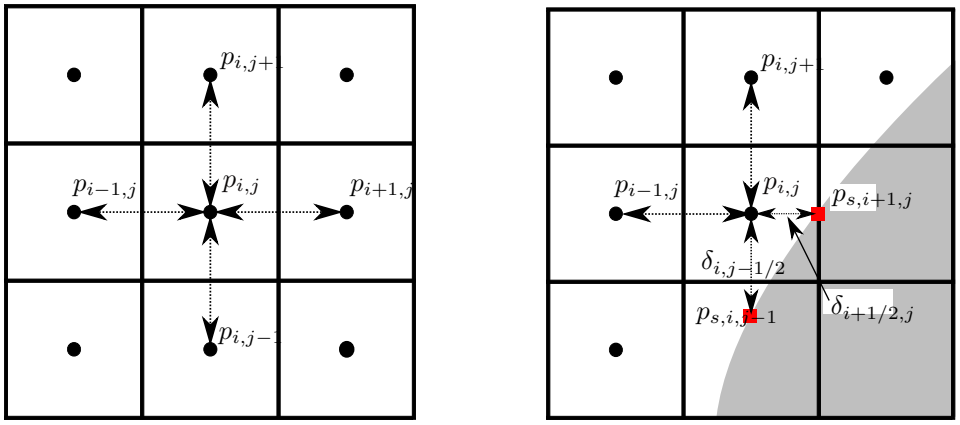

(a) Standard discretisation of the pressure equation in the liquid bulk

(b) Discretisation of the pressure equation near the interface

Figure 6.2: Schematic representation of the Poisson equation discretisation.

pressure in the x-direction will then be

$$p_{s,i+1,j} = p_{c,i+1,j} + \sigma \frac{\kappa_{i,j} + \kappa_{i+1,j}}{2} . \tag{6.3}$$

From (6.3) and (6.2) it is clear that accurate interface curvature as well as an accurate prediction of the interface location are important parameters to ensure the accuracy of the pressure solution.

The interface curvature is computed with the height function method in a way similar to that implemented in the Gerris code [46]. The height function is an approximate distance to the interface from a reference cell node and is calculated by summing the cell VOF values in a column aligned with one of the principal coordinate directions, called a height stack. The principal curvature can then be obtained by using finite difference approximations for the first and second derivatives of the height function. This method has been shown to produce second order accuracy for the curvature [46].

It is not always possible to find all the required heights to calculate a curvature. In this case a parabolic fit is made through the plane centroids of interface cells, which is then used to estimate the curvature.

Since the height function is the approximate interface distance from some reference cell in a given direction, it is used for δ. When the interface configuration is such that a height cannot be obtained in the required direction, the distance is approximated by using a plane reconstruction of the interface in the staggered volume. This is shown in Fig. 6.3.

First, the staggered VOF fractions are obtained by considering the plane reconstruction in centered cells. A similar procedure is then used in the staggered cells than in the centered cells to reconstruct the interface as a plane. With the plane constant known, the interface distance is then calculated.

The finite difference discretization of the left hand side of (3.11) for cell i, j in Fig. 6.2b will

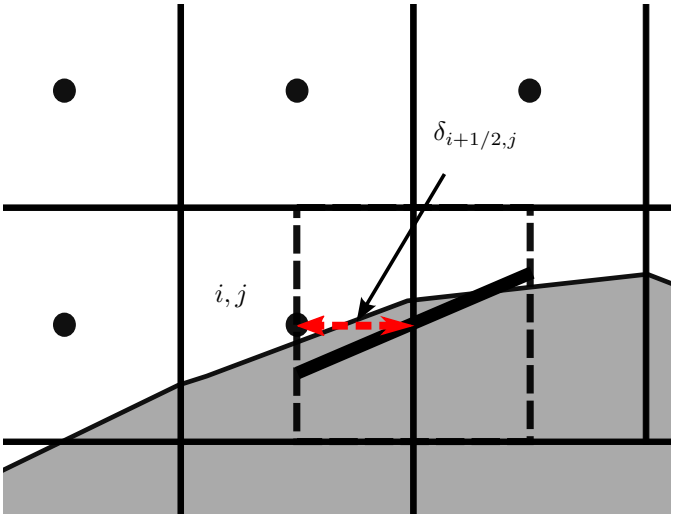

Figure 6.3: Cell i,j will typically not have a height available due to the interface configuration. A plane reconstruction (thick black line) is made in the staggered volume indicated with dashed lines and this reconstruction is used to obtain $\delta_{i+1/2,j}$.

then be

$$\begin{aligned}
&\frac{\Delta t}{\rho}\boldsymbol{\nabla}\cdot\left[\boldsymbol{\nabla}^h p^{n+1}\right] \\
&\quad\approx \frac{\Delta t}{\rho}\left(\frac{\nabla_y^h p_{i,j+1/2}-\nabla_y^h p_{i,j-1/2}}{1/2\left(\Delta y_{j+1/2}+\Delta y_{j-1/2}\right)}+\frac{\nabla_x^h p_{i+1/2,j}-\nabla_x^h p_{i-1/2,j}}{1/2\left(\Delta x_{i+1/2}+\Delta x_{i-1/2}\right)}\right) \\
&\quad= \frac{\Delta t}{\rho}\left(\quad\frac{2}{h+\delta_{i,j-1/2}}\left(\frac{p_{i,j+1}-p_{i,j}}{h}-\frac{p_{i,j}-p_{s,i,j-1}}{\delta_{i,j-1/2}}\right)\right. \\
&\qquad\left.+\frac{2}{\delta_{i+1/2,j}+h}\left(\frac{p_{s,i+1,j}-p_{i,j}}{\delta_{i+1/2,j}}-\frac{p_{i,j}-p_{i-1,j}}{h}\right)\quad\right).
\end{aligned} \tag{6.4}$$

The implementation in 3D is included in PARIS .

6.2 Extrapolation of the velocity field

The previous section dealt with the treatment of the pressure at the interface. The solution of the pressure Poisson equation, (3.11) is used in (3.9) to correct the predicted velocities obtained in (3.8). This section will deal with the velocity field required for the momentum contribution on the right hand side of (3.8). The term $\boldsymbol{u}\cdot\boldsymbol{\nabla}\boldsymbol{u}$ is discretized using a choice of schemes, including QUICK [38], ENO [27] and WENO [59].

For all these schemes, the discretization of $\boldsymbol{u}\cdot\boldsymbol{\nabla}\boldsymbol{u}$ may require a velocity stencil including neighbours up to two grid spacings away, depending on the upwind direction. The discrete pressures included in the solution have been explained previously, but since we are on a staggered grid, we need to do the same for velocity components. The velocities included are all those which are on a face that has a resolved pressure directly neighbouring it in any direction. Otherwise stated, all velocities which have a pressure gradient associated with it will be resolved. These are all velocity components that are marked with filled markers in Fig. 6.1.

As mentioned earlier, the resolved velocity components right next to the interface will require neighbours in the gas phase to discretize the momentum advection term. These values in the gas phase can be seen as boundary values to the resolved velocities. In order to find neighbours in the gas phase, we extrapolate the resolved velocities similarly to Popinet [47].

After calculating $\boldsymbol{u}^{n+1}$ in (3.9), we have a field of resolved velocities. To find the boundary velocities for the next time step, the closest two velocity neighbours inside the gas are extrapolated from the field of resolved liquid velocities using a linear least square fit. Let's assume the velocity field can be described as a linear combination

$$\boldsymbol{u}(\boldsymbol{x}) = \boldsymbol{A} \cdot (\boldsymbol{x} - \boldsymbol{x_0}) + \boldsymbol{u_0} \tag{6.5}$$

where the components of the tensor $\boldsymbol{A} = \nabla \boldsymbol{u}$ and of the vector $\boldsymbol{u_0}$ are the unknowns.
If we now take a 5×5 stencil around the unknown gas velocity at location $\boldsymbol{x_0}$, we can find the extrapolated velocity $\boldsymbol{u_0}$ by minimizing the functional

$$\mathcal{L} = \sum_{k=1}^{N} \left| \boldsymbol{A} \cdot (\boldsymbol{x_k} - \boldsymbol{x_0}) + \boldsymbol{u_0} - \boldsymbol{u_k} \right|^2 \tag{6.6}$$

This is done first for all locations closest to the resolved velocities $\boldsymbol{u_k}$ ("first neighbours"), whereafter it is repeated for the "second neighbours". Note that only resolved velocity components are included in the cost function, therefore the number N can vary depending on the shape of the interface. Furthermore, because of the staggered grid, only one velocity component of $\boldsymbol{u_0}$ is computed at location $\boldsymbol{x_0}$.

6.3 Ensuring volume conservation

The extrapolation of liquid velocities into the gas phase was explained in the previous section. An additional step is required to ensure that the extrapolated velocities are divergence free. This is required to ensure that the advection of the colour function (5.11) is conservative.

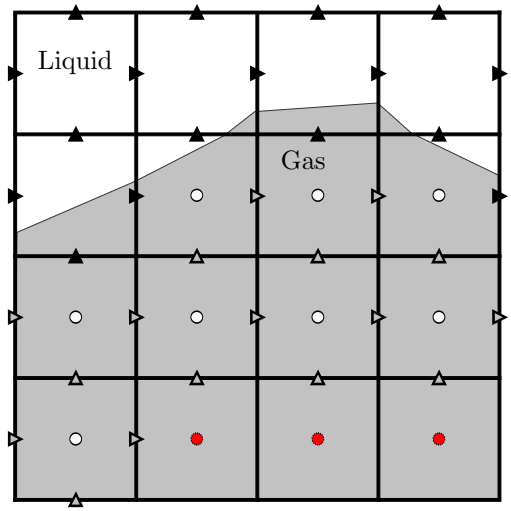

Figure 6.4: 2D example of the problem to correct the extrapolated velocities (unfilled triangles). A Poisson problem is solved in the cells marked with an unfilled circle.

A similar approach to Sussman [71] is used. Only the first two layers of cells inside the gas phase are considered and all other cells are disregarded. A 2D example is presented in Fig. 6.4.

Similar to the projection step explained earlier, a "phantom" pressure is obtained in these cells by solving a Poisson equation

$$\nabla^h \cdot \left(\nabla^h \hat{P} \right) = \nabla^h \cdot \tilde{\boldsymbol{u}} \,, \tag{6.7}$$

where $\hat{P}$ is the "phantom" pressure and $\tilde{\boldsymbol{u}}$ is the velocity on the faces of the first two gas neighbours. $\hat{P}$ is only calculated in the cells represented by unfilled nodes in Fig. 6.4. On the liquid side of these cells, the solved velocities (filled triangles) are used as a velocity boundary condition with the pressure gradient on this face set to zero. On the gas side outside the calculated cells (red filled circles), a fixed pressure is prescribed. Only the extrapolated velocities (unfilled triangles) are then corrected by the pressure gradient $\nabla \hat{P}$, which was found by solving (6.7)

$$\tilde{\boldsymbol{u}}^{n+1} = \tilde{\boldsymbol{u}} - \nabla^h \hat{P} \tag{6.8}$$

to ensure non-divergence of velocity in the first two layers of cells just inside the gas.

Chapter 7

Results

This chapter will present a validation test for the implemented numerical method presented in the previous chapter. The results from several multiple bubble tests will then be presented.

7.1 Single bubble validation with Rayleigh-Plesset

A widely-used [8, 47, 71] validation test for volume changing bubbles in an incompressible liquid, is to compare a numerical simulation of a single gas bubble with a fixed liquid pressure at infinity to the solution of the Rayleigh-Plesset equation [44]. This equation describes the evolution of a bubble of radius R in an incompressible liquid, assuming spherical symmetry with some fixed pressure at infinity. A derivation for this equation is given in Appendix B.1. Neglecting viscous effects, the Rayleigh-Plesset equation is written for the evolution of the radius R of a gas bubble, exposed to a pressure p_∞ at infinity

$$\begin{aligned} \ddot{R}R + \frac{3}{2}\dot{R}^2 &= \frac{p_s - p_\infty}{\rho_l} \\ &= \frac{p_c - \frac{2\sigma}{R} - p_\infty}{\rho_l} \end{aligned} \tag{7.1}$$

where R is the bubble radius, p_s the pressure on the liquid side of the interface, p_∞ the pressure at infinity, σ the surface tension coefficient and ρ_l the liquid density. The bubble pressure, p_c, is obtained from a polytropic gas law

$$p_c(t) = p_0 \left(\frac{V_0}{V(t)} \right)^\gamma \tag{7.2}$$

where $\gamma = 1.4$ is the isentropic gas coefficient, V_0 is the bubble volume at some reference pressure p_0 and $V(t)$ is the bubble volume.

7.1.1 Simulation setup

A bubble of radius R is placed in the center of a cubic domain. The initial bubble radius is chosen such that the bubble is not in equilibrium with p_∞ and will expand or shrink as a result.

The application of boundary conditions to the problem is not trivial, since some finite flow domain must be created, but the Rayleigh-Plesset is derived with a pressure at an infinite distance. This problem is addressed by using the solution of (7.1) to obtain an expression for the pressure

Cell size, h $[\times 10^{-3}]$	**Vol., t=0.075** $[\times 10^{-3}]$	**Vol. Rel. Error** [%]	**t at** V_{min}	**t Rel. Error** [%]
15.63	7.004	7.16	0.1187	4.27
7.813	7.065	6.35	0.1191	3.95
3.906	7.141	5.35	0.1195	3.63

Table 7.1: The cavity volume at t=0.075 is compared to the theoretical value (7.5446×10^{-3}) for three different grid resolutions. The time at which the volume reaches a minimum is also compared to the theoretical value (0.124).

$$p(r,t) = p_s - \rho_l \left(\frac{\dot{R}^2 R^4}{2r^4} - \frac{\ddot{R}R^2 + 2R\dot{R}^2}{r} + \ddot{R}R + \frac{3}{2}\dot{R}^2 \right) . \tag{7.3}$$

The derivation is shown in Appendix B.2. The solution for the Rayleigh-Plesset equation (7.1) is obtained numerically with a fifth order Runge-Kutta integration method. The time step size for the numerical solution of (7.1) is deliberately chosen to coincide with that of the PARIS simulation, to ensure that the pressure calculated from (7.3) is applied consistently at the boundary. A zero normal gradient is applied for the velocity on the boundary.

A test case is set up with the following parameters: A bubble with radius $R(t_0) = 0.15$ is placed in the center of a cubic domain, containing liquid with density $\rho_l = 1.0$ and a surface tension coefficient $\sigma = 0.05$. The bubble is assumed to be at rest at t_0: $\dot{R}(t_0) = 0$. The bubble has a radius R_0 at reference pressure $p_0 = 1.0$ and the pressure at infinity is $p_\infty = 1.5$.

First, a time convergence study was performed to determine a fixed time step size. The solution was deemed converged in time for a time step of $\Delta t = 10^{-5}$ on a grid with $N_x \times N_y \times N_z = 64^3$ grid points.

Three simulations were completed for one oscillation cycle with 64^3, 128^3 and 256^3 grid points and time step sizes $\Delta t = 10^{-5}$, $\Delta t = 5 \times 10^{-6}$ and $\Delta t = 2.5 \times 10^{-6}$ respectively.

Fig. 7.1 shows a comparison between the results in PARIS and a numerical solution of the Rayleigh-Plesset equation. In Table 7.1, some quantitative results are given. More specifically, the cavity volume at time t=0.075 is compared to the theoretical volume and the relative error is calculated. The time at which the cavity reaches its minimum volume is also compared to the theoretical value.

A relatively good agreement was achieved, but the rate of convergence in space is slow, which may suggest that the solution is close to being converged in space. Another important factor to consider in this test case, is the boundary effect which is caused by applying a zero normal gradient on the velocity. The actual velocity field is spherically symmetric. One way to compensate for this effect is to increase the ratio of the domain length to mean bubble radius, $L/\overline{R}$, where $\overline{R}$ is the mean radius. To study this effect, the same test case was used, but with varying domain sizes L. Three cases were tested, with $L = 0.5$, $L = 1.0$ and $L = 2.0$ respectively. The same grid size is used ($h = 7.813 \times 10^{-3}$) and the time step size is kept constant, $\Delta t = 5 \times 10^{-6}$. The result is shown in Fig. 7.2 and the relative errors for the same criteria as in 7.1 are presented in Table 7.2.

It can be seen from this result that the solution in Fig. 7.1 likely suffered from the boundary effect. To further illustrate this point, a second test was created where the initial radius of the bubble, $R(t_0) = 0.10$, is chosen 50% smaller than the previous test. The remaining parameters are selected such that the bubble radius decreases significantly more than in the previous test, thereby ensuring that the ratio $L/\overline{R}$ is much higher. The surface tension is $\sigma = 0.10$, $p_\infty = 0.5$ and the reference pressure $p_0 = 1.0$ at a radius $R_0 = 0.9$ This test case was run on a domain

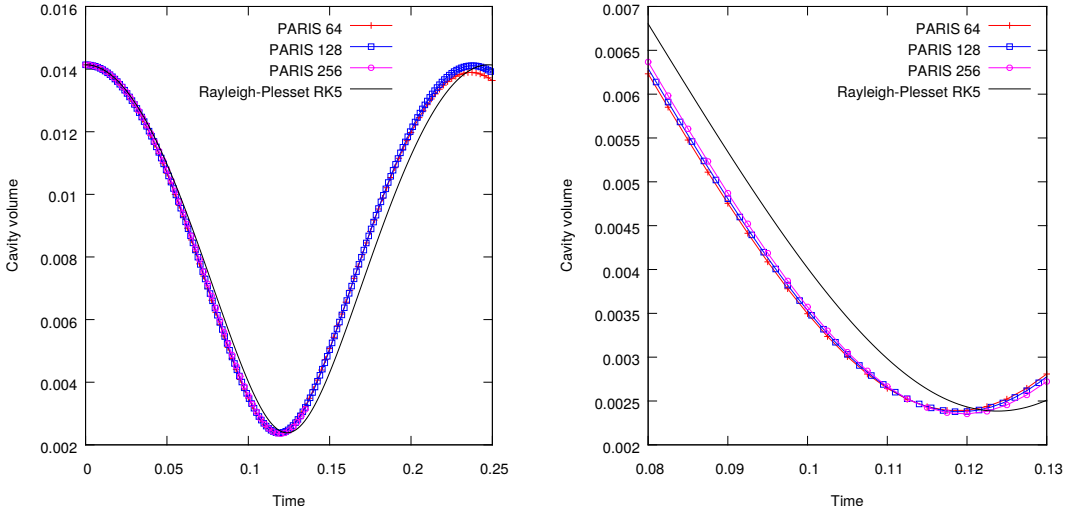

Figure 7.1: Comparison of results of a single oscillating gas bubble simulated by PARIS and the Rayleigh-Plesset equation.

$^{L}/_{\overline{R}}$ **ratio**	**Volume, t=0.075** $[\times 10^{-3}]$	**Volume Rel. Error** [%]	**time at** V_{min}	**time Rel. Error** [%]
4.29	6.032	20.05	0.1105	10.89
8.59	7.065	6.35	0.1191	3.95
17.18	7.411	1.77	0.1225	1.21

Table 7.2: The relative errors are calculated using the same criteria as in 7.1, but for three different ratios of $^{L}/_{\overline{R}}$.

with $L = 1.0$ with 128^3 grid points. The result for two complete bubble oscillations is shown in Fig. 7.3.

An improved agreement is obtained. Note that the grid resolution in this problem was $\Delta x = {}^{1}/_{128}$, which is double the resolution of the finest grid in the previous case. This gives confidence that a large portion of the error is attributable to the boundary effect. Further convergence studies become prohibitively expensive without the use of adaptive meshing. However, the agreement achieved is considered sufficient to proceed with the study of the model problem.

7.2 Multiple bubble tests

In this section the results of model problem simulations containing multiple pre-nucleated bubbles are presented. The setup of the numerical simulations will be described and some non-dimensional numbers will be defined by which the flow can be characterized. A parametric study will then be performed.

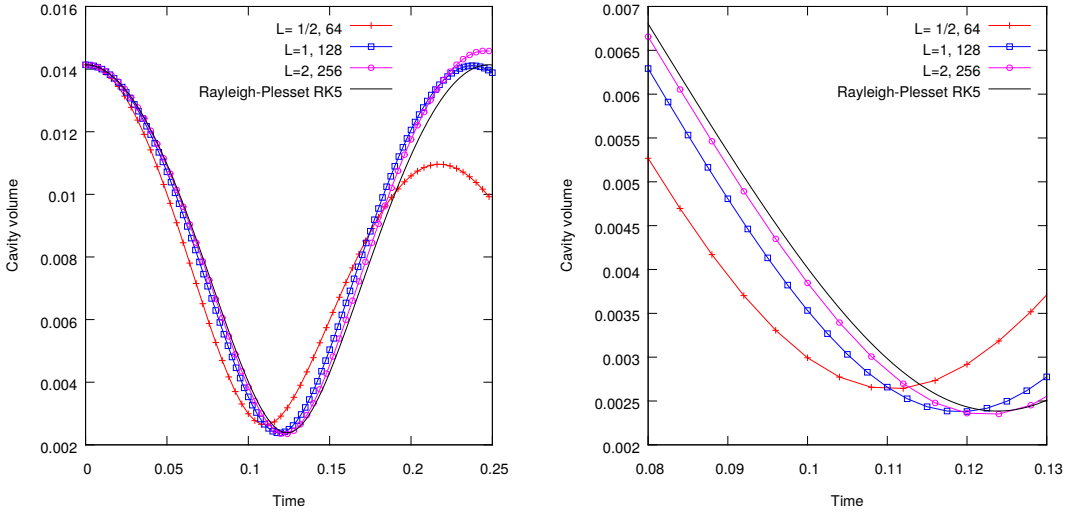

Figure 7.2: Results of the same test case for three $^{L}/_{R}$ ratios.

7.2.1 Simulation setup

As mentioned in Section 4.2.1, the shock wave effect in the liquid will be modelled with a constant rate of expansion, ω. This is imposed by applying a constant outflow velocity, U_n, normal to all faces of the cubic domain, so that

$$\omega = \frac{6U_n}{L}\,, \tag{7.4}$$

with L the length of the cube.

All simulations are started with bubbles pre-nucleated at some finite size. Bubbles are seeded in a face centered cubic (FCC) lattice. The bubble positions can correspond to the exact lattice nodes, or with some random displacement around this position. Fig. 7.4 shows a 2D slice of a typical simulation setup. Bubbles are placed in a central zone, referred to as the bubble zone. An all-liquid zone along the domain boundaries form a liquid layer between the bubbles and the outflow faces. The size of this zone is chosen conservatively such that only liquid exits the domain up to a void fraction of approximately 30%. The inter-bubble distance, ℓ_D, is given by

$$\ell_D = \left(\frac{L^3}{N_0}\right)^{\frac{1}{3}}\,, \tag{7.5}$$

with N_0 the number pre-nucleated bubbles. Bubbles are initialized with a radius R_0 and the parameter $\Delta R_0/R_0$ describes the variance in the initial bubble diameter R_0 so that $R_{min} < R_0 < R_{min} + \Delta R_0$. Once the center position and radius of each bubble have been generated, the colour function field can be easily and accurately initialized with the VOFI library [4].

To a characterize the problem, a Weber number is introduced based on the fluid density, ρ, surface tension σ and the inter-bubble distance given above

$$We = \frac{\rho \ell_D^3 \omega^2}{\sigma}\,. \tag{7.6}$$

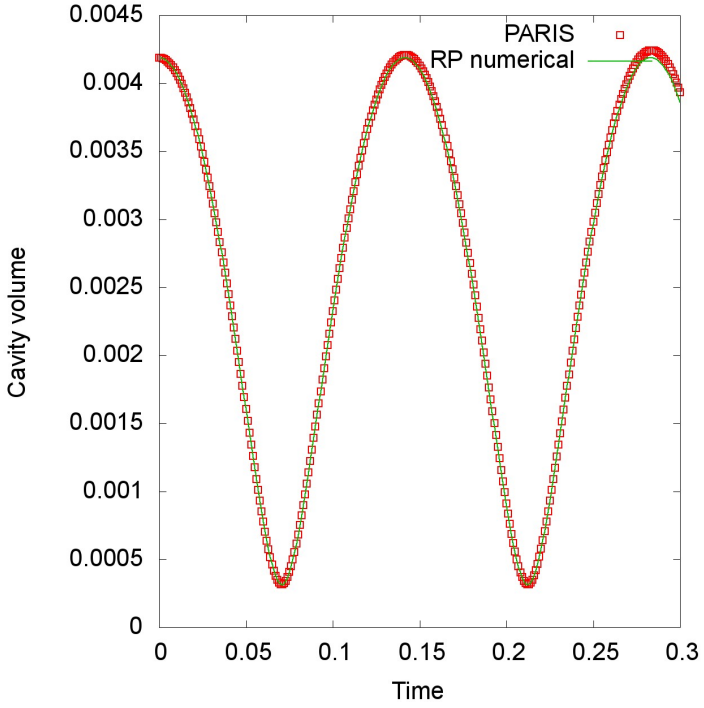

Figure 7.3: Results of the second test case.

Considering the Weber number, two extremes in the type of flows exist: In the $We \to 0$ limit, surface tension dominates (is infinite) over expansion. In the opposite case, the expansion dominates or surface tension and $We \to \infty$. First, the $We = 0$ limit is studied and then some cases with increasing We will be presented.

7.2.2 Zero Weber

A test case will be presented for the case when $We \to 0$. This case is created by defining a simulation where periodic boundary conditions are used on a unit cube, instead of using an outflow velocity. There are 172 bubbles pre nucleated with $R_0 = 0.025$ and $\Delta R_0/R_0 = 0.5$. The bubble zone is an inner cube with length 0.75.

A volume evolution plot is shown in Fig. 7.5. A time scale based on the bubble radius can be defined as

$$\tau_R = \left(\frac{\rho R^3}{\sigma} \right)^{\frac{1}{2}}, \tag{7.7}$$

with $\rho = 1000$ and $\sigma = 0.01$ in this case. It is clear from the plot on the right that this time scale is the time scale of bubble collapse.

A plot of the pressure in Fig. 7.6 shows how the average pressure decreases in the domain as the bubble competition tends to minimize the surface energy.

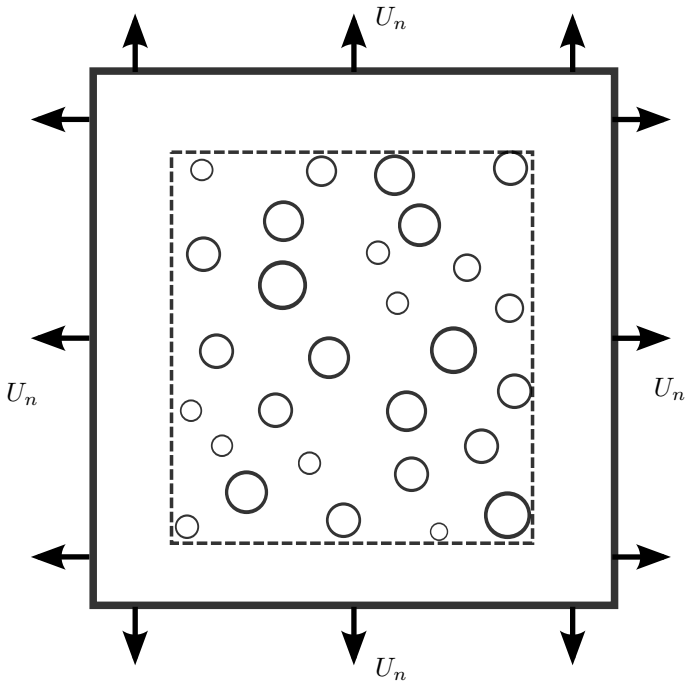

Figure 7.4: 2D slice through domain showing typical simulation setup. A uniform velocity outflow rate is specified on the domain faces. Bubbles are initialised in an internal bubble zone, surrounded by a layer of pure liquid.

7.2.3 Multiple bubbles

Table 7.3 gives the simulation parameters used for a series of tests.

In this section the results of three test cases with $N_0 = 365$ initial bubbles in an expanding domain will be given. By varying the normal outflow velocity U_n, different expansion rates, ω are obtained. Three velocities are considered, 5.5×10^{-3}, 2.75×10^{-2} and 1.75×10^{-1}, corresponding to the three Weber numbers, 5×10^{-4}, 1.3×10^{-2} and 0.54, of Table 7.3.

The effect of We on the simulation results can be appreciated in Fig. 7.8, where individual bubble volumes are plotted against the total void fraction. Since constant outflow rates are used, the void fraction is directly proportional to time.

It is observed that the higher the Weber number, the later bubble collapse occurs. The number of bubble collapses at a given total void fraction decreases with increasing We. Fig. 7.9 shows screen shots at progressive time steps. A bubble competition is therefore observed: some larger bubbles tend to grow at the demise of smaller ones. The two-dimensional slices on the right show bubbles with a pressure heat map. With the vanishing vapour pressure model, a pressure gradient is formed in the liquid from large to small bubbles. This is the effect of surface tension. The average pressure also decreases with time, similar to the effect observed in the zero We case. An average pressure evolution plot is presented in Fig. 7.7 for the average pressure in the three cases.

The bubble radius distribution is presented in Fig. 7.10. Initially all bubbles expand for the high We case.

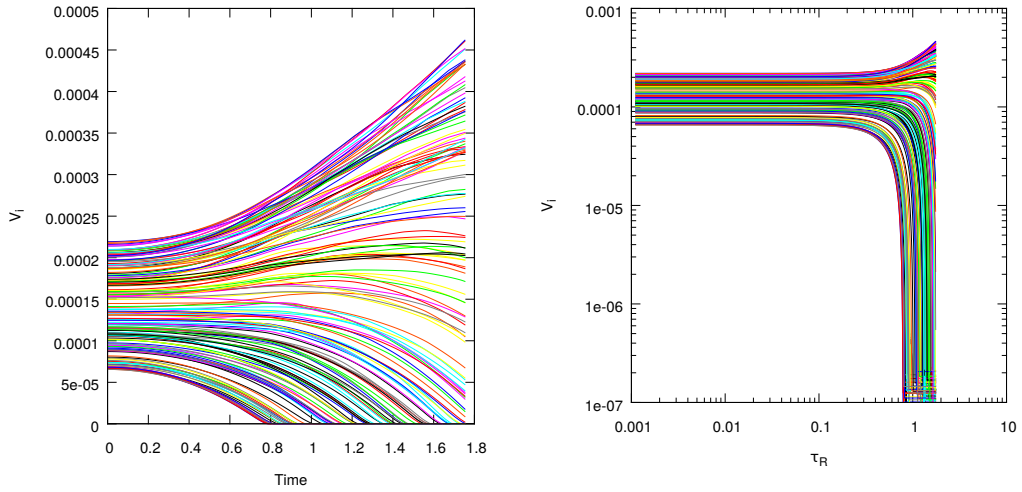

Figure 7.5: The volume evolution of individual bubbles are shown for the $We = 0$ case. On the right, the τ_R time scale is used with a logarithmic scale.

Parameter	**Value**
Buffer to domain length ratio	0.12
Expansion rate ω	0.033, 0.165, 1.05
Initial bubbles N_0	365
Grid points	512^3
We	$5 \cdot 10^{-4}$, 0.013, 0.54
$\Delta R_0/R_0$	0.5
$\Delta \ell_D/\ell_D$	0, 0.2

Table 7.3: Simulation parameters for multiple bubble tests.

7.2.4 Bubble interaction

In this section a proportionality between the time scale of pore competition and the Weber number is formulated. Since the liquid is incompressible, the fluid outflow with a constant velocity is balanced by an overall volume expansion of the bubbles in the computational domain. If we assume that bubbles are of the same radius, we can write

$$\omega L^3 = \sum_{i=1}^{N} 4\pi R_i^2 \dot{R}_i \tag{7.8}$$

The sum of the volume expansion of each bubble is written in terms of the volume expansion of an average bubble of radius $\overline{R}$ with an average rate of change of its radius $\dot{\overline{R}}$

$$\sum_{i=1}^{N} 4\pi R_i^2 \dot{R}_i = N 4\pi \overline{R}^2 \dot{\overline{R}}\,. \tag{7.9}$$

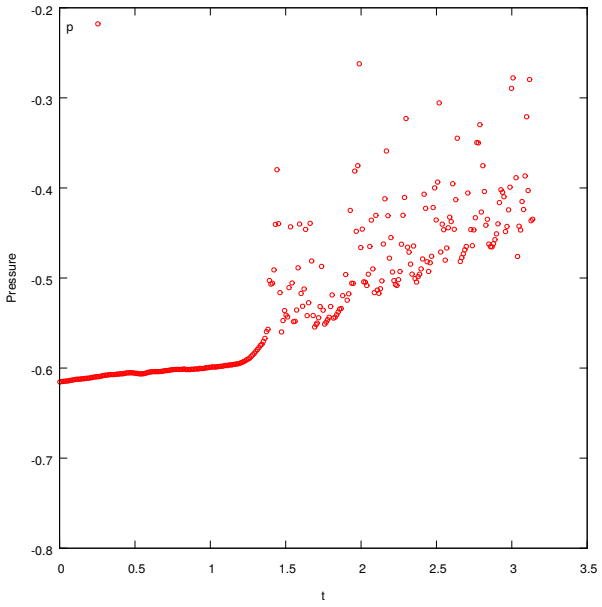

Figure 7.6: The average pressure in the domain for the $We = 0$ case. Note that the negative pressures are not of concern, as the actual value does not have a meaning in incompressible flow. The reason for the negative values is the zero vapour pressure in cavities.

Using these averaged bubbles, (7.8) is integrated to obtain an average radius evolution equation

$$\overline{R}^3(t) = \frac{3\omega L^3 t}{4\pi N} \tag{7.10}$$

Here it is inherently assumed that $R_0 \ll 1$, which is true since bubbles are initialised to be as small as possible.

Let $t_{1/2}$ be the time at which half of the bubbles have collapsed. Using dimensional analysis and assuming that bubble collapse happens on a time scale dictated by the bubble radius length scale, we write

$$t_{1/2} = \left(\frac{\rho \overline{R}(t_{1/2})^3}{\sigma} \right)^{1/2} . \tag{7.11}$$

If (7.10) is substituted in and rearranged, this becomes

$$t_{1/2}\omega = \frac{3\omega^2 \rho\, \ell_D^3}{4\pi\sigma} = \frac{3}{4\pi} We_{\ell_D} . \tag{7.12}$$

This was tested for three cases of different We and the results are given in Fig. 7.11. The time $t_{1/2}$ was measured by either considering all the bubbles inside the domain, or by excluding the outermost ones. It is interesting to note that the measured times differ, especially for the higher We case. This indicates a buffering effect exerted by the outermost bubbles leading to different evolution rates for the bubbles towards the interior. The relationship is at least qualitatively linear, but should be confirmed with tests at a wide range of Weber numbers.

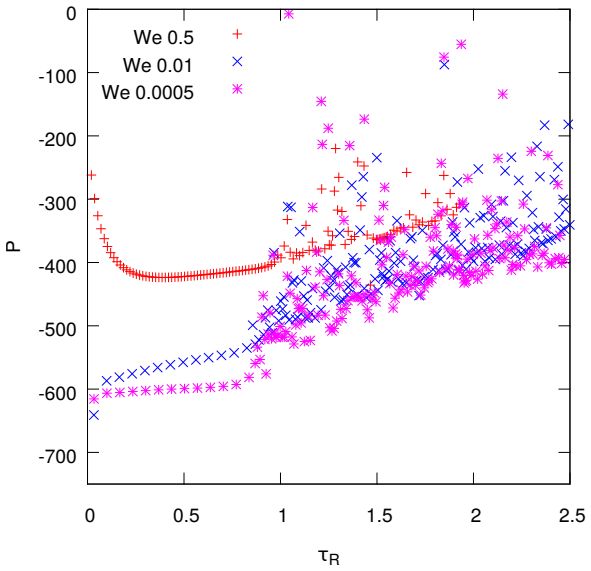

Figure 7.7: The average pressure in the domain for the three cases of different We.

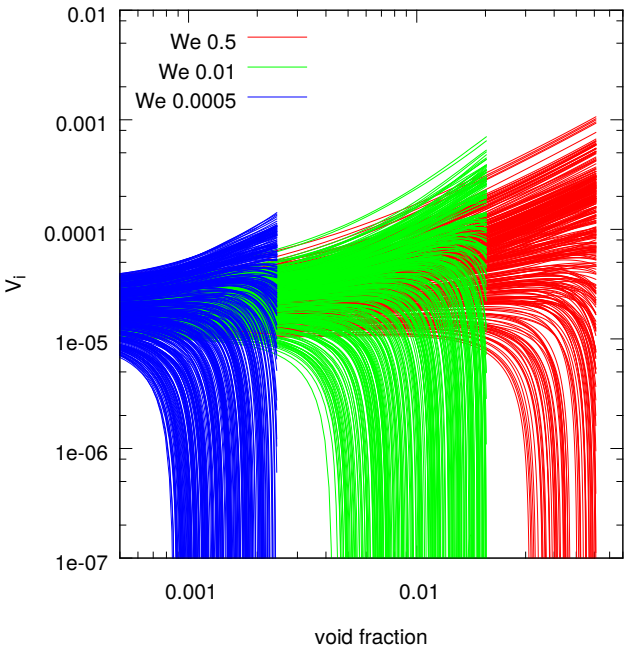

Figure 7.8: Comparison of individual bubble volumes for varying We. Bubble collapse is delayed with increasing We as the domain expansion counters capillary effects. Individual bubble volumes are plotted as function of total void fraction.

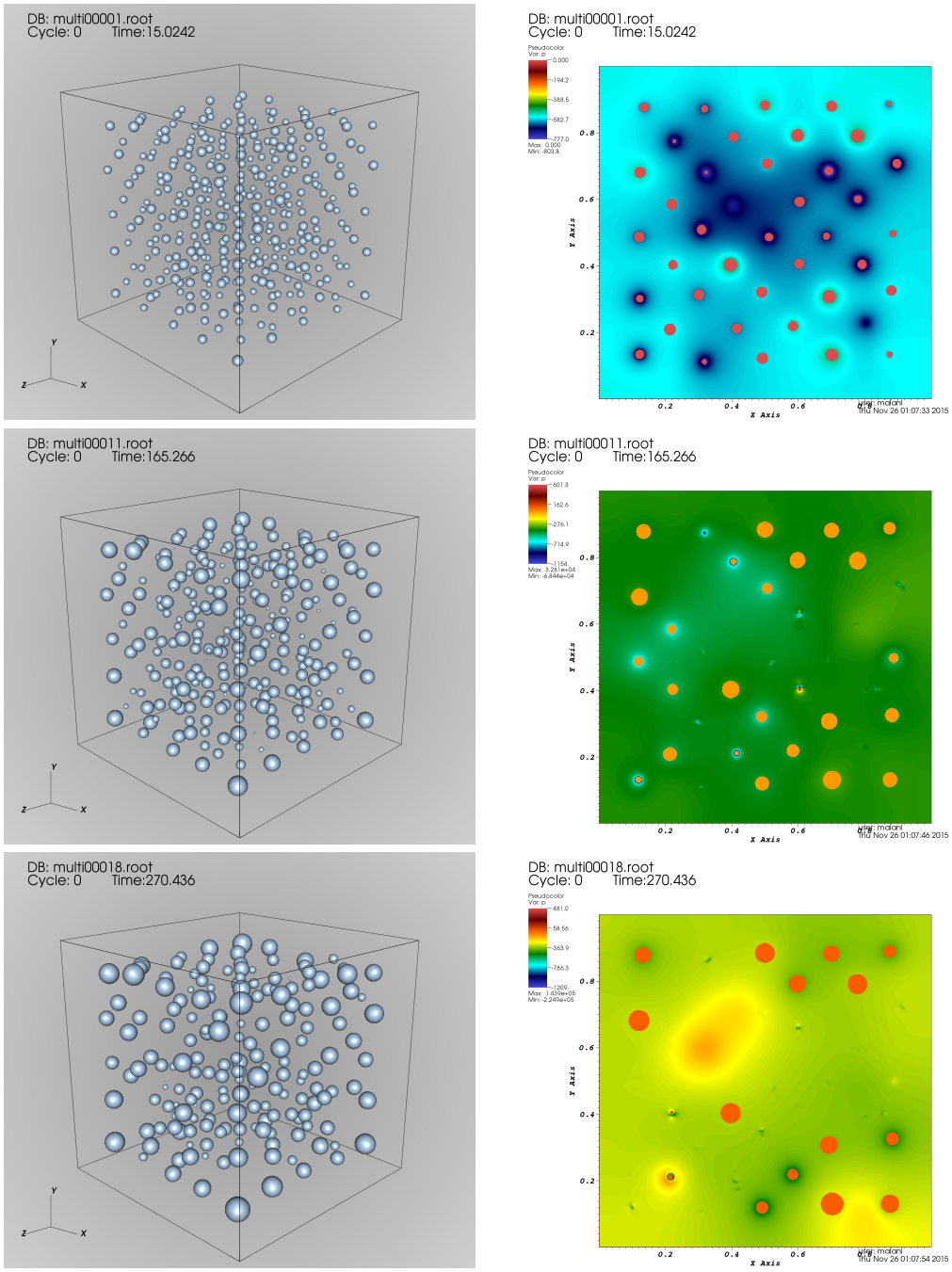

Figure 7.9: VisIt screenshots of a simulation with 365 initial bubbles at $We = 0.1$. The left shows a 3D view of bubbles at progressive time steps. The images on the right show the pressure distribution at the same instances for a section at $z = 0.5$.

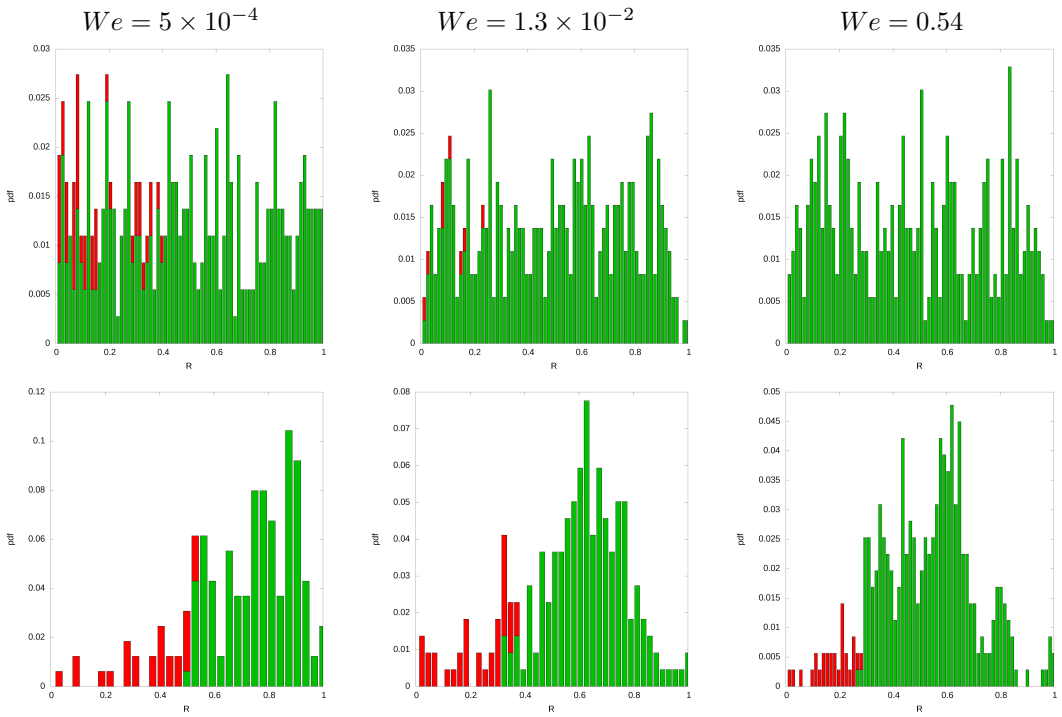

Figure 7.10: Distribution of bubble radii, with growing bubbles shown in green. The first row shows the initial distribution and the second after 3000 time steps.

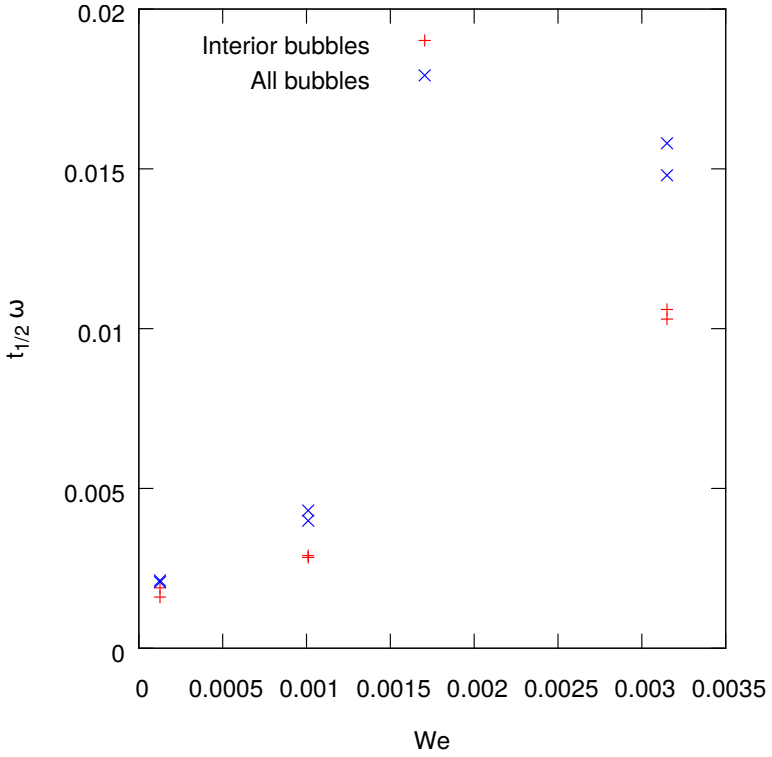

Figure 7.11: Comparison of non-dimensional collapse time for half the initial bubbles, $t_{1/2}\omega$ for three We cases.

Chapter 8

Conclusion: Part I

This chapter presented a numerical method to study compressible bubble clouds in an incompressible liquid under tension. This was a pre-defined model problem for the percolation of cavities in liquid metals under shock loading, also known as micro-spall failure.

A free surface approach was used to allow for volume variations in pre-nucleated cavities. The cavity pressure was assumed constant in space and was determined using a polytropic gas law. The VOF method was used to locate the interface to track its movement and to calculate surface tension effects. Surface tension was accounted for in the pressure, of which the gradient calculation at the interface received special care to apply a pressure on the free surface that accounts for surface tension and the cavity phase pressure. Additionally, the velocity field was extrapolated across the interface and ensured to be divergence-free to serve as boundary values for the numerical schemes that calculate momentum change and VOF advection.

The numerical implementation was validated against the result of the Rayleigh-Plesset equation, which describes the evolution of the radius of a single bubble in response to a distant, non-equilibrium pressure. It was found that the effect of a boundary condition that is not spherically symmetric contributes significantly to the error. Otherwise, a reasonable agreement with the theoretical solution was obtained.

Multiple bubble tests were undertaken as a model for the large micro-spall problem. A parametric study was conducted in which the carrier liquid expansion rate was varied along with the surface tension between simulations. The hypothesis of bubble competition was observed: Larger bubbles were expanding faster than the average fluid expansion rate, at the expense of smaller bubbles.

Part II

Phase change

Chapter 9

Introduction: Part II

In this chapter the phase change problem that will be studied in Part II will be presented. The background to the problem will lead to a problem statement. The method of investigation will be presented, with a review of previous work. Next, the original contribution that is made by this work will be stated followed by a hypothesis and some research questions that will be addressed throughout Part II.

9.1 Background

In this part of the work, the focus will specifically be on two-phase flows where phase change occurs. Flows with phase change are particularly important to mankind with application in a multitude of industrial processes. A good example is the generation of electricity. For a large portion of the global production of energy, a Rankine cycle is used where steam is generated with some heat source, including coal, gas, nuclear or concentrated solar rays. The steam is then passed through a turbo-generator, after which it is condensed back to a liquid. The understanding of these phase change processes is of great importance for the efficient and safe operation of these type of plants. The power generation example is only one of many in a host of industrial applications. Another example is the process of distillation, which is used from petro-chemical refineries to breweries.

It is probably due to a combination of the usefulness of flows with phase change and the complexity of the physics thereof that it is a popular research topic. Research methods are just as vast as the physical processes they are studying. There are analytical studies using mathematical modelling, experimental methods and numerical studies. The latter may be system level solutions, where empirical or mathematical flow models (or some combination of the two) are used to set up a model of the system. These equations are then solved with the aid of different kind of computer solvers. Another approach may be direct numerical simulation (DNS), where the governing equations are derived from first principles and solved without any additional models to account for unresolved physics.

In this work, a DNS method to study flows with phase change is developed. The problem statement will be given in the next section, followed by details of the research methodology.

9.1.1 Method of investigation

The governing equations for this problem will be described in the following chapter. Novel aspects of the mathematical formulation will be added to PARIS . There are several test cases available

with analytical solutions, which are often used to validate numerical simulations of boiling. In this work, the same approach will be used and the validation results will be presented in 12. Note that when the term "phase change" is used throughout Part II, it refers specifically to phase change of pure substances.

Before a problem statement is formulated, a review of previous numerical methods for the simulation of flows with phase change will be given. This follows next

9.2 Previous work

There have been a significant amount of methods developed to study flows with phase change. An overview of some of the most cited work will be given here. The different methods will be grouped according to the method used to track the interface.

Level-Set methods

The Level-Set (LS) method is attributed to Osher and Sethian [43], with a prominent publication by Sussman *et al.* [73] following a few years later.

Son and Dhir used a Level-Set method in various numerical studies on flows with phase change. In [64] a numerical study on the bubble release pattern during film boiling is presented. A study on the heat transfer during nucleate boiling was also performed by these authors along with Ramanujapu [65]. Here a single bubble nucleation site was used along with a micro-layer model for heat transfer beneath the growing bubble.

Gibou *et al.* developed a method to simulate flows with phase change based on a LS method developed earlier [23] and a Ghost-Fluid method [41]. A similar method was used by Tanguy [76] to simulate an evaporating droplet in air and Sagan [50] to study nucleate boiling for the application of cryogenic fuel tanks. Huber *et al.* recently performed a study on nucleate boiling with large microscopic contact angle [31].

Level-Set methods are often combined with VOF methods to create a hybrid calculation method, referred to as Couple Level-Set and Volume-Of-Fluid (CLSVOF). Different calculations (like the interface curvature or mass advection) are calculated with different methods. An early publication on this method was by Bourlioux [5]. Later, Sussman *et al.* demonstrated the capability of the method for flows with topological changes and surface tension [72]. To simulate flows with phase change, Tomar *et al.* proposed a method [77], which was later used to study film boiling [78].

Front tracking methods

Tryggvason *et al.* have published several studies using a Front Tracking (FT) method [82]. With Juric, [33] a FT method is developed that uses a one-fluid formulation to simulate flows with phase change. The paper also includes a detailed discussion on the interface temperature. Two dimensional film boiling is studied after validation with a one dimensional test case. Esmaeeli and Tryggvason studied explosive boiling in micro-gravity [18] and three dimensional film boiling [19] using similar numerical methods.

Constrained interpolation profile methods

Sato and Ničeno developed a Constrained Interpolation Profile method (CIP) that uses an interface sharpening technique to deal with diffusion of the interface [52]. This framework was used for phase change problems, including nucleate boiling of a single bubble [53] and multiple bubbles using an empirical model for nucleation site density [51].

VOF methods

Volume-Of-Fluid methods for phase change can be classified using several calculation techniques. One of the distinguishing factors is how interface properties are calculated. These properties include the interface location, its curvature and mass transfer rate. Another aspect to consider in VOF methods which is non-trivial is the advection of the VOF function. The advection is typically done in two ways: Either a geometric reconstruction of the interface is performed, which is used to calculate surface fluxes for advection purposes, or an algebraic advection method is used. Welch and Wilson developed a VOF method for phase change [86]. They solve conservation of mass, momentum and energy on a staggered (MAC) grid. The interface is reconstructed using piecewise linear segments, based on the method of Youngs [89]. A split time geometric advection technique from the same author [89] is used to advect the interface. The technical details of this advection is described very briefly in the paper. Welch and Rachidi [85] expanded this method to study film boiling with conjugate heat transfer with the heated wall. Agarwal *et al.* [1] used the Welch method in [86] with the addition of temperature dependence on fluid properties.

Schlottke and Weigand used a geometric based method to study evaporating droplets [57]. They developed an intricate iterative method to deal with the calculation of a volume source due to mass transfer in which they make the assumption that the interface moves at the same velocity as the liquid phase.

There have also been some methods where an algebraic method is used for advection of the VOF function. Kunkelmann [36] used the OpenFOAM framework and implemented a micro-layer and contact angle model to simulate nucleate boiling on arbitrary meshes. The interface mass transfer was modelled by a smearing technique, where source terms are redistributed some distance from the interface. Guedon [24] attempted to apply a sharp interface approach, using a similar VOF advection method and interface mass transfer term calculation as Kunkelmann, also in the OpenFOAM environment. A ghost-fluid approach was used at the interface to treat discontinuities. He reported difficulties from spurious currents due to unbalanced surface tension models.

9.2.1 Discussion

The VOF method is a well-established method for the DNS of multi-phase flows. For flows with phase change there have been some methods proposed, but there are non-trivial aspects that are not well described in literature. One aspect is the VOF advection method. Algebraic methods have improved, but often suffer from diffusion of the VOF function. For phase change problems this may require additional effort to simulate interface physics. For geometric advection methods, the details of how the method functions in a discontinuous velocity field is largely unanswered. Welch and Wilson applied a technique to solve for mass conservation and then to use the updated mass to calculate the VOF function. However, the details of how the mass flux was calculated is unclear.

Additionally, the advection of the VOF function also directly influences mass and energy conservation. In the thermal energy conservation equation, the ratio of total specific heats between phases is more than 3000 for water at atmospheric conditions. If a simple volume weighted approach is used to calculate the heat capacity, coupled with a naive algebraic advection discretisation of the energy and momentum fluxes, there can be very large numerical diffusion around the interface.

The above aspects are pertinent to VOF methods for phase change using an incompressible assumption, but they often also apply to other interface capturing methods.

9.3 Problem statement

The goal in this Part of this work is to develop a novel numerical method to solve flows with phase change. More specifically, a DNS approach will be used in a VOF framework with planar interface reconstruction (PLIC) and a one-fluid description of the governing equations, assuming incompressible flow. The method will also assume small temperature variations and low flow speeds, such that the Boussinesq approximation can be applied, as explained in section 2.2.3. The interface will be treated as sharp (infinitely thin), separating immiscible fluids.

9.4 Contribution in this work

A novel geometric VOF advection method will be proposed to deal with discontinuities that arise from mass transfer at a sharp interface. The VOF advection technique will be applied consistently to the calculation of the energy advection term.

The mathematical formulation of the problem described in the previous section requires several interface properties. These properties include the interface location, the area of interface segments and gradients of fluid variables on either side of the interface. The method proposed in this work will use the geometric (PLIC) representation to calculate these interface properties.

9.4.1 Research Hypothesis

The VOF method for two-phase flows with phase change at a sharp interface can be used for DNS purposes by using local geometric reconstructions of the interface for consistent, conservative advection and to calculate interface properties by only using the VOF function.

9.4.2 Research questions

- How can the VOF funcion be advected using a geometric representation when there are discontinuities in the velocity field?
- Can the other advection terms be treated similarly, ensuring consistency?
- What is the accuracy on benchmark test cases?

Chapter 10

Mathematical Formulation

A general mathematical formulation for the governing equations of fluid flow was presented in Chapter 2, along with some general simplifying assumptions that were made in the process of deriving them. The mathematical formulation for the phase change problem will now be presented, using the general formulation presented earlier as a starting point. First, a problem specific control volume will be defined, which introduces an important difference to the control volume presented in Fig. 2.1.

10.1 Control volume definition

Similar to the previously defined control volume, Fig. 10.1 shows a problem specific control volume, V, which is completely enclosed by surface S, can be of arbitrary shape and is fixed in space. An important new feature is that Γ is no longer a material surface, but can move at its own velocity $\boldsymbol{u}_\Gamma$, which in general will differ from the velocity of neighbouring fluids. Volume V is divided into volumes V_ℓ and V_g by interface Γ, where the subscripts ℓ and g indicate the liquid and gas phases, respectively. Similarly, S is divided into S_ℓ and S_g. The convention used throughout for the interface normal, $\boldsymbol{n}_\Gamma$, is that it points outward from the liquid into the gas.

10.1.1 Interface mass transfer

With mass transfer possible at the interface, a difference in velocity between the fluids and the interface Γ is present and it is no longer assumed that the velocity field across Γ is smooth. This difference in velocity can be explained by considering a certain finite sized fluid packet of one phase that neighbours a packet of the opposite phase, Fig. 10.2. If this specific packet changes phase, the interface shifts the size of that packet, since the interface is per definition the boundary in between phases. The interface velocity relative to the fluid packet is the rate at which the resulting shift occurs.

10.1.2 Control volume analysis

The general control volume analysis for a fluid property B in a fixed volume (2.3) still applies to V, since surface S is fixed in space. It is repeated here for later reference

$$\left.\frac{dB}{dt}\right|_{sys} = \int_V \frac{\partial\left(\rho\beta\right)}{dt}\, dV + \oint_S \rho\beta\left(\boldsymbol{u}\cdot\boldsymbol{n}\right)\, dA\,, \tag{10.1}$$

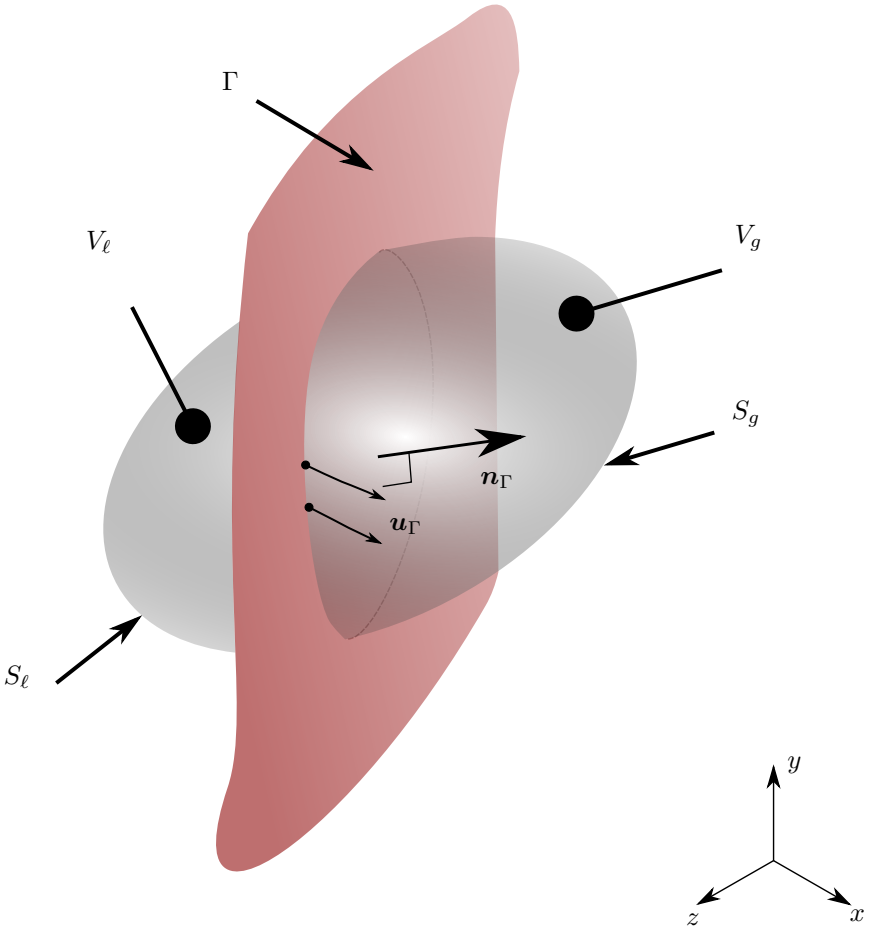

Figure 10.1: The control volume under consideration in this part contains a sharp interface Γ (red shading) that moves at its own velocity $\boldsymbol{u}_\Gamma$, other than the control volume used in Chapter 2. The outer surfaces S_ℓ and S_g are fixed in space.

where the nomenclature is the same as introduced earlier.

10.2 Governing equations

The governing equations that apply to this problem will be given here, along with jump conditions that may be present due to the evolution of the interface and phase change.

10.2.1 Mass conservation

The general integral form for mass conservation derived in Chapter 2 is still valid, since it was also derived for a fixed control volume

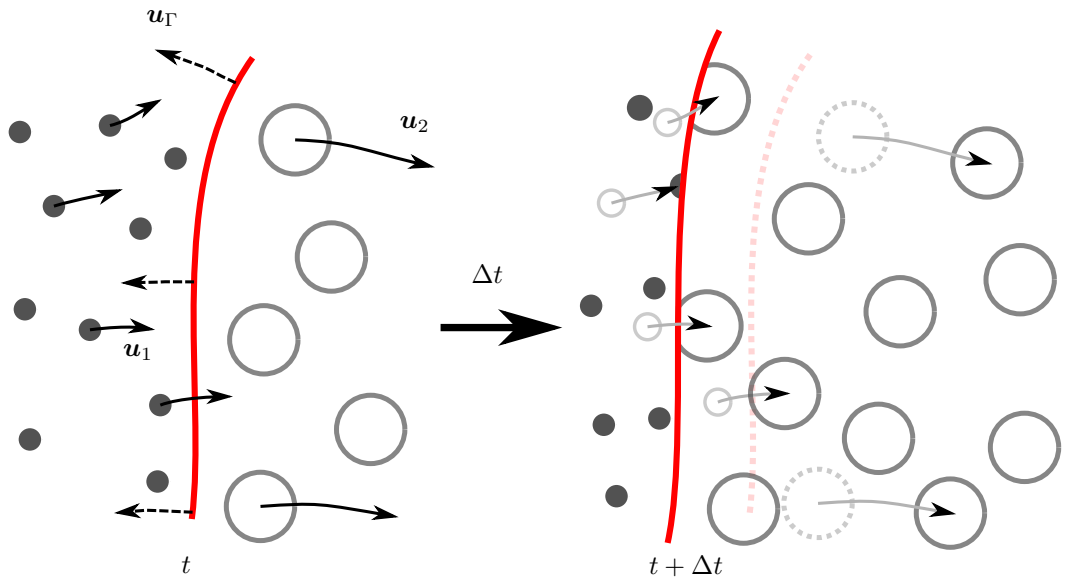

Figure 10.2: A zoom of the interface is presented on the left at time t, followed by time $t+\Delta t$ on the right. On the right, the previous positions of some fluid packets are shown in a faded shade, with the previous interface position indicated by the dotted line.

$$\int_V \frac{\partial \rho}{\partial t}\, dV + \oint_S \rho\, (\boldsymbol{u} \cdot \boldsymbol{n})\, dA = 0\,. \tag{10.2}$$

However, care should be taken at the interface since there may now be a discontinuity in velocity, as introduced in section 10.1.1. The interface jump conditions will be derived next, followed by the general one-fluid formulation for mass conservation when the incompressible assumption is applied.

Interface jump condition

In 10.1.1 the existence of an interface velocity, $\boldsymbol{u}_\Gamma$, which differs from the liquid and gas velocities on either side, was introduced. The effect of this relative velocity at the interface will now be evaluated using the principle of mass conservation in the separate phase volumes V_ℓ and V_g. Due to the potential presence of a discontinuity in velocity across the interface, the velocity fields in the respective phases will be denoted as $\boldsymbol{u}_\ell$ and $\boldsymbol{u}_g$ respectively. The same applies to the density ρ. Mass conservation for each phase can be written using (10.2)

$$\frac{d}{dt}\left(\int_{V_\ell} \rho_\ell\, dV \right) + \int_{S_\ell} \rho_\ell\, (\boldsymbol{u}_\ell \cdot \boldsymbol{n})\, dA + \int_\Gamma \rho_\ell\, (\boldsymbol{u}_\ell - \boldsymbol{u}_\Gamma) \cdot \boldsymbol{n}_\Gamma\, dA \;= 0 \tag{10.3}$$

$$\frac{d}{dt}\left(\int_{V_g} \rho_g\, dV \right) + \int_{S_g} \rho_g\, (\boldsymbol{u}_g \cdot \boldsymbol{n})\, dA - \int_\Gamma \rho_g\, (\boldsymbol{u}_g - \boldsymbol{u}_\Gamma) \cdot \boldsymbol{n}_\Gamma\, dA \;= 0 \tag{10.4}$$

Note that the surface integral for the interface Γ still calculates the efflux based on the relative velocity $\boldsymbol{u}_r = \boldsymbol{u} - \boldsymbol{u}_\Gamma$, which can be non-zero. The negative sign for the surface integral over Γ

in phase 2 comes from the convention that the interface normal $\boldsymbol{n}_\Gamma$ points outward from phase 1 into phase 2.

By recognizing that

$$\frac{d}{dt}\left(\int_{V_\ell}\rho_\ell\,dV\right)+\frac{d}{dt}\left(\int_{V_g}\rho_g\,dV\right)=\int_V\frac{\partial\rho}{\partial t}\,dV \tag{10.5}$$

and

$$\int_{S_\ell}\rho_\ell\boldsymbol{u}_\ell\cdot\boldsymbol{n}\,dA+\int_{S_g}\rho_g\boldsymbol{u}_g\cdot\boldsymbol{n}\,dA=\oint_S\rho\left(\boldsymbol{u}\cdot\boldsymbol{n}\right)\,dA\,, \tag{10.6}$$

equations (10.3) and (10.4) can be added and then mass conservation (10.2) can be applied. The result is a mass balance at the interface

$$\int_\Gamma\rho_\ell\left(\boldsymbol{u}_\ell-\boldsymbol{u}_\Gamma\right)\cdot\boldsymbol{n}_\Gamma\,dA=\int_\Gamma\rho_g\left(\boldsymbol{u}_g-\boldsymbol{u}_\Gamma\right)\cdot\boldsymbol{n}_\Gamma\,dA\,. \tag{10.7}$$

The physical interpretation is that the total amount of mass traversing the interface from one phase equals the mass gained by the other. The mass transfer per unit area of interface is defined as

$$\dot{m}''=\rho_\ell\left(\boldsymbol{u}_\ell-\boldsymbol{u}_\Gamma\right)\cdot\boldsymbol{n}_\Gamma=\rho_g\left(\boldsymbol{u}_g-\boldsymbol{u}_\Gamma\right)\cdot\boldsymbol{n}_\Gamma \tag{10.8}$$

From the simultaneous equations in (10.8) one can eliminate $\boldsymbol{u}_\Gamma$. The result is the velocity jump condition across the interface due to mass transfer:

$$\left(\boldsymbol{u}_\ell-\boldsymbol{u}_g\right)\cdot\boldsymbol{n}_\Gamma=\dot{m}''\left(\frac{1}{\rho_\ell}-\frac{1}{\rho_g}\right)\,. \tag{10.9}$$

Note that the inverse density is the specific volume, $v={}^1\!/_\rho$, which implies that different specific volumes in neighbouring phases cause a difference in velocity across the interface when phase change occurs. As a finite amount of one phase changes into another phase, it contracts or expands and therefore a relative velocity to the remainder of its original phase is created.

General integral form

To obtain the integral form of the mass conservation governing equation for the problem here, the mass conservation for each phase is reconsidered, (10.3) and (10.4). However, instead of considering the full phase volume up to the interface Γ, a fixed boundary is introduced parallel to the interface at an infinitesimal distance on each side of the interface. These interfaces will be called $\hat{\Gamma}_\ell$ and $\hat{\Gamma}_g$ for the fixed boundaries introduced on the sides of phases 1 and 2 respectively.

Since the velocity fields $\boldsymbol{u}_\ell$ and $\boldsymbol{u}_g$ are continuous everywhere in the new volumes $\hat{V}_\ell$ and $\hat{V}_g$ and all boundaries are fixed, we can apply Gauss's divergence theorem without needing consideration for relative velocities at any control surface.

$$\int_{\hat{V}_\ell}\frac{\partial\rho_\ell}{\partial t}+\boldsymbol{\nabla}\cdot\left(\rho_\ell\boldsymbol{u}_\ell\right)\,dV\;=0 \tag{10.10}$$

$$\int_{\hat{V}_g}\frac{\partial\rho_g}{\partial t}+\boldsymbol{\nabla}\cdot\left(\rho_g\boldsymbol{u}_g\right)\,dV\;=0\,. \tag{10.11}$$

Applying the assumption of incompressible flow, these equations become

$$\int_{\hat{V}_\ell} \boldsymbol{\nabla} \cdot \boldsymbol{u}_\ell \, dV = 0 \tag{10.12}$$

$$\int_{\hat{V}_g} \boldsymbol{\nabla} \cdot \boldsymbol{u}_g \, dV = 0 \,. \tag{10.13}$$

The differential form of the mass conservation equation can now be compiled by considering the control volume V as the sum of three volumes

$$V = \hat{V}_\ell + \hat{V}_g + \delta V \tag{10.14}$$

with δV the infinitesimal control volume around the interface, sandwiched between $\hat{V}_\ell$ and $\hat{V}_g$.

With the mass conservation for each phase volume $\hat{V}_\ell$ and $\hat{V}_g$ known, volume δV still needs to be calculated. This is done by taking the limit when δV tends to zero, or when $\hat{\Gamma}_\ell$ and $\hat{\Gamma}_g$ tend to Γ from both sides of the interface. When writing mass conservation in δV for an incompressible flow, only the surface fluxes through $\hat{\Gamma}_\ell$ and $\hat{\Gamma}_g$ remain:

$$\int_{\hat{\Gamma}_g \to \Gamma} \boldsymbol{u}_g \cdot \boldsymbol{n}_\Gamma \, dA - \int_{\hat{\Gamma}_\ell \to \Gamma} \boldsymbol{u}_\ell \cdot \boldsymbol{n}_\Gamma \, dA = \int_\Gamma \dot{m}'' \left(\frac{1}{\rho_g} - \frac{1}{\rho_\ell} \right) dA = \int_{\delta V} \boldsymbol{\nabla} \cdot \boldsymbol{u} \, dV \,, \tag{10.15}$$

The mass conservation in V is now evaluated as the sum of individual volumes (10.14), using (10.12), (10.13) and (10.15)

$$\int_V \boldsymbol{\nabla} \cdot \boldsymbol{u} \, dV = \int_\Gamma \dot{m}'' \left(\frac{1}{\rho_g} - \frac{1}{\rho_\ell} \right) dA = \int_V \dot{m}'' \left(\frac{1}{\rho_g} - \frac{1}{\rho_\ell} \right) \delta_\Gamma \, dV \,, \tag{10.16}$$

Here equation (2.10) was again used to convert the surface integral over Γ to a volume integral. This is the integral form of mass conservation for incompressible fluids with mass transfer at the interface. The delta function indicates that the divergence of velocity is zero everywhere, except on the interface where there is a divergence caused by the difference in specific volume of phases as mass is transferred. Note that the velocity divergence will be zero in V for the trivial case when $\dot{m}'' = 0$ or when $\rho_\ell = \rho_g$.

10.2.2 Momentum conservation

Conservation of linear momentum was derived in Chapter 2, including the effect of surface tension as a line force on the interface and a temperature dependant density in the gravity force

$$\int_V \frac{\partial \left(\rho_0 \boldsymbol{u} \right)}{\partial t} \, dV + \oint_S \rho_0 \boldsymbol{u} \left(\boldsymbol{u} \cdot \boldsymbol{n} \right) \, dA = \oint_S \boldsymbol{\tau} \cdot \boldsymbol{n} \, dA + \int_V \rho \boldsymbol{g} \, dV + \int_V \sigma \kappa \delta_\Gamma \boldsymbol{n}_\Gamma \, dV \,, \tag{10.17}$$

Interface jump condition

Since the rate of change of linear momentum in a system equals the resultant force acting on it, a force balance on the interface can be made to derive the interface jump condition. This is done by integrating (10.17) in a δV, defined in the previous section and the resulting force balance at the interface is

$$\rho_\ell \boldsymbol{u}_\ell \left(\boldsymbol{u}_r \cdot \boldsymbol{n}_\ell\right) + \rho_g \boldsymbol{u}_g \left(\boldsymbol{u}_r \cdot \boldsymbol{n}_g\right) = \boldsymbol{\tau_\ell} \cdot \boldsymbol{n_\ell} + \boldsymbol{\tau_g} \cdot \boldsymbol{n_g} + \sigma\kappa \boldsymbol{n}_\Gamma \,, \tag{10.18}$$

with the relation between the outward pointing normals relative to each phase subject to the convention $\boldsymbol{n}_\Gamma = \boldsymbol{n}_\ell = -\boldsymbol{n}_g$. The resulting surface gradient term is equal to zero here, due to the assumption of a constant surface tension coefficient. Using this convention and the mass transfer jump condition, the general interface jump condition can be written

$$\dot{m}'' \left(\boldsymbol{u}_\ell - \boldsymbol{u}_g\right) = \left(p_g \mathbf{I} - \mathbf{D}_g - p_\ell \mathbf{I} + \mathbf{D}_\ell\right) \cdot \boldsymbol{n}_\Gamma + \sigma\kappa \boldsymbol{n}_\Gamma \,. \tag{10.19}$$

It is useful to take the normal and tangential components of this equation. The jump condition in the normal direction is obtained by projecting (10.19) in the direction of $\boldsymbol{n}_\Gamma$

$$p_g - p_\ell = \boldsymbol{n}_\Gamma \cdot \mathbf{D}_g \cdot \boldsymbol{n}_\Gamma - \boldsymbol{n}_\Gamma \cdot \mathbf{D}_\ell \cdot \boldsymbol{n}_\Gamma + \left(\dot{m}''\right)^2 \left(\frac{1}{\rho_\ell} - \frac{1}{\rho_g}\right) - \sigma\kappa \,. \tag{10.20}$$

In the tangential direction, the jump condition is obtained by projecting (10.19) in the direction of $\boldsymbol{t}_{\Gamma,d}$, [81, p.40]. Here $\boldsymbol{t}_{\Gamma,d}$ are d unit tangent vectors to Γ. In three dimensional geometry, two vectors are required to define the jump condition, therefore $d = 1, 2$.

$$\boldsymbol{t}_{\Gamma,d} \cdot \mathbf{D}_g \cdot \boldsymbol{n}_\Gamma - \boldsymbol{t}_{\Gamma,d} \cdot \mathbf{D}_\ell \cdot \boldsymbol{n}_\Gamma = \dot{m}'' \left(\boldsymbol{u}_g - \boldsymbol{u}_\ell\right) \cdot \boldsymbol{t}_{\Gamma,k} \,, \tag{10.21}$$

Here it is noted again that the surface gradient term is zero due to the assumption of constant surface tension. With the kinematic condition of no slip between phases, the terms on the right hand side in (10.21) are zero and only the shear stress terms remain

$$\boldsymbol{t}_{\Gamma,d} \cdot \mathbf{D}_g \cdot \boldsymbol{n}_\Gamma = \boldsymbol{t}_{\Gamma,d} \cdot \mathbf{D}_\ell \cdot \boldsymbol{n}_\Gamma \,. \tag{10.22}$$

This is the kinematic condition on the interface that stipulates continuity of shear stress.

10.2.3 Energy conservation

The conservation of thermal energy derived previously with the Boussinesq approximation will be applied to the present problem

$$\int_V \frac{\partial \left(\rho c_p T\right)}{\partial t} \, dV + \oint_S \rho c_p T \boldsymbol{u} \cdot \boldsymbol{n} \, dA = \oint_S k \boldsymbol{\nabla} T \cdot \boldsymbol{n} \, dA \,. \tag{10.23}$$

The interface jump condition will be derived and presented in the following section.

Interface jump condition

The jump condition of the thermal energy conservation is derived here by integrating (10.23) in the control volume δ. For a more detailed derivation, refer to the works of Delhaye [16] and Kataoka [35].

$$\int_{\hat{\Gamma}_\ell \to \Gamma} \rho_\ell c_{p,\ell} \, T_\Gamma \left(\boldsymbol{u}_\ell - \boldsymbol{u}_\Gamma\right) \cdot \boldsymbol{n}_\Gamma \, dA - \int_{\hat{\Gamma}_g \to \Gamma} \rho_g c_{p,g} \, T_\Gamma \left(\boldsymbol{u}_g - \boldsymbol{u}_\Gamma\right) \cdot \boldsymbol{n}_\Gamma \, dA =$$
$$\int_\Gamma \left(k_g \boldsymbol{\nabla} T \cdot \boldsymbol{n}_\Gamma - k_\ell \boldsymbol{\nabla} T \cdot \boldsymbol{n}_\Gamma\right) \, dA$$

$$\int_\Gamma \dot{m}''\,(c_{p,\ell}-c_{p,g})\,T_\Gamma\,dA = \int_\Gamma \left(k_g\nabla_{n_\Gamma}T|^g - k_\ell\nabla_{n_\Gamma}T|^\ell\right)\,dA$$
$$\int_\Gamma \dot{m}''h_{fg}\,dA = \int_\Gamma \left(k_g\nabla_{n_\Gamma}T|^g - k_\ell\nabla_{n_\Gamma}T|^\ell\right)\,dA\,. \tag{10.24}$$

Note that in the equation above, the assumption of thermal equilibrium was made. By this assumption the interface temperature is assumed to equal the saturated temperature at prevailing system conditions. This assumption is accurate when the characteristic length scale of the flow is much larger than that of the thermodynamic conditions [81, p.250]. This is the case for the flows considered in this work, therefore, in (10.24) we have that $T_\Gamma = T_{sat}$.

The latent heat of vaporization, h_{fg} was introduced and is the difference of enthalpies at the interface $h_{fg} = \hat{h}_\ell - \hat{h}_g$. Note that the signs for the heat flux terms are written according to the convention of $\boldsymbol{n}_\Gamma$ pointing outward from the liquid into the gas.

The last line in (10.24) is a thermal energy balance between the heat conduction to the interface and the enthalpy change due to the latent heat of vaporization. Let $\dot{q}_\Gamma$ be the the heat source due to latent energy release during phase change, so that

$$\int_\Gamma \dot{m}''h_{fg}\,dA = \int_V \dot{q}_\Gamma\delta_\Gamma\,dV\,, \tag{10.25}$$

where we have used (2.10).

It should be noted that the resulting thermal energy jump condition neglects the jump in kinetic energy across the interface. To evaluate this assumption, let us assume that $\boldsymbol{u_g} \gg \boldsymbol{u_\ell}$. The interfacial jump in kinetic energy can then be approximated with

$$[e_k] \approx \dot{m}''u_g^2 \approx (\dot{m}'')^3\left(\frac{1}{\rho_g}-\frac{1}{\rho_\ell}\right)^2\,, \tag{10.26}$$

where (10.9) was used along with the previous assumption that $\boldsymbol{u_g} \gg \boldsymbol{u_\ell}$. The relative importance of the kinetic energy jump can be evaluated by considering the ratio

$$\frac{(\dot{m}'')^3\left(\frac{1}{\rho_g}-\frac{1}{\rho_\ell}\right)^2}{\dot{m}''h_{fg}} = \frac{(\dot{m}'')^2\left(\frac{1}{\rho_g}-\frac{1}{\rho_\ell}\right)^2}{h_{fg}}\,. \tag{10.27}$$

For the problems under consideration in this work, this ratio is $< 10^{-6}$ and it is therefore reasonable to neglect the kinetic energy contribution.

10.3 Conclusion and summary

This section will present a summary of all the assumptions and models applied during the derivation of the governing equations that will be used in the research problem.

10.3.1 Summary of flow hypotheses used in this work

A continuum approach is used in three dimensional space to describe the motion of incompressible fluids. Up to two separate phases can be modelled with a phase indicator function allowing for a one-fluid approach and describing the interface location using consecutive multiplication of one-dimensional delta functions distributed along the interface. Separate phases are immiscible

and are separated by a sharp interface across which there may be mass transfer during a phase change process. No slip is allowed between phases at the interface.

All fluids are considered to be Newtonian. Gravity will be included as a body force and surface tension effects on the interface are accounted for with the assumption that the surface tension coefficient is constant all along the interface.

No internal heat generation sources are considered and heating by viscous dissipation is considered negligible. Heat conduction is modelled using Fourier's law and no radiative heat transfer is taken into account. A Boussinesq approach is adopted, based on small temperature variations. By this approximation, all fluid properties (density, viscosity, specific heat capacity, thermal conductivity) are assumed constant, with the exception of the density in the gravity force term of the momentum equation. In this case, a linear density variation with temperature is adopted. Thermal equilibrium is assumed, such that the temperature is continuous across the interface and the interface temperature is the saturated temperature at prevailing conditions.

10.3.2 System of governing equations

The integral forms of the governing equations for the problem are:

Mass conservation

$$\int_V \boldsymbol{\nabla} \cdot \boldsymbol{u}\, dV = \int_V \dot{m}'' \left(\frac{1}{\rho_g} - \frac{1}{\rho_\ell} \right) \delta_\Gamma \, dV \tag{10.28}$$

Momentum conservation

$$\int_V \frac{\partial \left(\rho_0 \boldsymbol{u} \right)}{\partial t} \, dV + \oint_S \rho_0 \boldsymbol{u} \left(\boldsymbol{u} \cdot \boldsymbol{n} \right) \, dA = \oint_S \boldsymbol{\tau} \cdot \boldsymbol{n} \, dA + \int_V \rho \boldsymbol{g} \, dV + \int_V \sigma \kappa \delta_\Gamma \boldsymbol{n}_\Gamma \, dV \tag{10.29}$$

Thermal energy conservation

$$\int_V \frac{\partial \left(\rho c_p T \right)}{\partial t} \, dV + \oint_S \rho c_p T \boldsymbol{u} \cdot \boldsymbol{n} \, dA = \oint_S k \boldsymbol{\nabla} T \cdot \boldsymbol{n} \, dA + \int_V \dot{q}_\Gamma \delta_\Gamma \, dV \tag{10.30}$$

These equations will be discretized on a specific numerical grid to be solved with the aid of a computer. The next chapter will describe the numerical method that will be implemented for this purpose.

Chapter 11

Numerical Method

This chapter details the numerical method that is employed to solve the system of governing equations provided in the previous chapter. Importantly, several novel numerical techniques that are used to simulate phase change flows are introduced. These techniques, implemented into PARIS as part of this work, include:

- a geometric (PLIC) based mass transfer rate calculation
- a simple yet elegant geometric VOF advection method that is expanded to deal with a velocity discontinuity at the interface
- and the addition of a thermal energy conservation equation with a consistently calculated advection term.

The numerics of each contribution will be detailed, followed by the complete time integration technique of the set of governing equations for the phase change problem.

11.1 Calculating the mass transfer rate

In the previous section the mass conservation for the present problem was derived and is repeated here for readability

$$\int_V \boldsymbol{\nabla} \cdot \boldsymbol{u}\, dV = \int_V \dot{m}'' \left(\frac{1}{\rho_g} - \frac{1}{\rho_\ell} \right) \delta_\Gamma \, dV \,. \tag{11.1}$$

To implement this equation in the numerical scheme, the mass transfer rate needs to be calculated in all cells containing the interface, known as mixed cells. The equation used to do so comes from the jump condition at the interface (10.24) and is written in discrete form for cell i, j, k

$$\dot{m}''_{i,j,k} = \frac{k_g}{h_{fg}} \nabla^h_{n_\Gamma} T|^g_{i,j,k} - \frac{k_\ell}{h_{fg}} \nabla^h_{n_\Gamma} T|^\ell_{i,j,k} \,, \tag{11.2}$$

where $\nabla^h_{n_\Gamma}$ indicates a discrete gradient either side of the interface. To find $\dot{m}''$, we therefore need to determine the temperature gradients at the interface for each phase. To calculate these in a mixed cell, the temperature in that same cell cannot be used, since it is some average of the two phase temperatures in the computational cell. A method to address this is presented in the next section.

11.1.1 Interface heat flux calculation

The heat flux from each phase required in (11.2) inside a mixed cell is calculated as the weighted average of the heat fluxes from pure cells (containing only one phase) neighbouring the mixed cell. This is similar to the approach of Kunkelmann [36], which was also applied by Guedon [24]. The heat flux in a pure cell is calculated using a finite difference

$$k_p \nabla^h_{n_p} T = k_p \frac{T_{i,j,k} - T_\Gamma}{d_\Gamma} \,, \tag{11.3}$$

with d_Γ the normal distance from the temperature node (at the cell center) to the interface and $p = \ell, g$ a phase indicator. Recall that it is assumed that $T_\Gamma = T_{sat}(p_{sys})$. The temperature $T_{i,j,k}$ is known from the solution of thermal energy conservation, so that the only remaining unknown in (11.3) is the interface normal distance d_Γ.

To calculate the interface normal distance, the PLIC plane reconstruction in each interface cell is used. The interface is defined locally in a cell as a plane given by the implicit equation

$$\alpha = \boldsymbol{m} \cdot \boldsymbol{x} \,, \tag{11.4}$$

with α a constant and $\boldsymbol{m} = \langle m_1, m_2, m_3 \rangle$ the interface normal vector, which is scaled locally for the purposes of interface reconstruction such that

$$|m_1| + |m_2| + |m_3| = 1 \,. \tag{11.5}$$

The normal $\boldsymbol{m}$ is calculated using the VOF function with the Mixed Youngs-centered method (MYC), [3] and α is obtained by using geometrical volume calculations [55]. In the local cell coordinate system, the distance to the interface from the local cell origin can be found by normalizing (11.4)

$$d_{i,j,k} = \frac{\boldsymbol{m}}{||\boldsymbol{m}||} \cdot \boldsymbol{x} = \boldsymbol{n}^h_\Gamma \cdot \boldsymbol{x} \,, \tag{11.6}$$

with $d_{i,j,k}$ the local interface normal distance in a mixed cell and $\boldsymbol{n}^h_\Gamma$ the reconstructed planar interface normal vector. Note that for the interface normal gradient we adopt a convention here to always calculate the finite difference in the outward direction from the interface to the cell, so that $\boldsymbol{n}_g = \boldsymbol{n}_\Gamma = -\boldsymbol{n}_\ell$.

To obtain the distance to any neighbouring cell, this local distance equation is used and a coordinate transformation is applied. Let $\Delta\boldsymbol{x}$ be the translation vector from the mixed cell under consideration to the desired location. The normal distance at $\boldsymbol{x}+\Delta\boldsymbol{x}$ to the planar reconstruction of the interface is then

$$d_\Gamma = d_{i,j,k} - \boldsymbol{n}^h_\Gamma \cdot \Delta\boldsymbol{x} \,. \tag{11.7}$$

Inside a pure cell, one can imagine that through the transformation in (11.7), the distance can be obtained to the interface representation in various mixed cells, depending on the interface geometry, see Fig. . In this case the collinearity of the plane normal in the mixed cell and the translation vector is used

$$\xi = |\boldsymbol{n}^h_\Gamma|_{i,j,k} \cdot \Delta\boldsymbol{x}| \,. \tag{11.8}$$

The neighbour with the maximum value of ξ is used to determine d_Γ.

The interface heat flux can now be calculated in the pure cell using (11.3). This is done for all pure cells that are first or second neighbours to mixed cells.

Finally, the fluxes required to compute phase change in (11.2) are now computed by using a weighted average of pure cell heat fluxes. This is done by considering all the first and second,

pure cell neighbours in the desired phase. The example of liquid is given here, but the same applies for the gas phase:

$$\nabla^h_{n_\ell} T|^\ell_{i,j,k} = \sum_{\hat{i},\hat{j},\hat{k}} \chi_{\hat{i},\hat{j},\hat{k}} \frac{T^\ell_{\hat{i},\hat{j},\hat{k}} - T_\Gamma}{d_{\Gamma,\hat{i},\hat{j},\hat{k}}}\,, \tag{11.9}$$

where the hat indices indicate the stencil with two neighbours, taking the i-direction as an example $i-2 \leq \hat{i} \leq i+2$. The normalized weighting factor χ is given by

$$\chi_{\hat{i},\hat{j},\hat{k}} = \frac{\gamma_{\hat{i},\hat{j},\hat{k}}}{\sum\limits_{\hat{i},\hat{j},\hat{k}} \gamma_{\hat{i},\hat{j},\hat{k}}}\,, \tag{11.10}$$

with γ in its turn determined by the collinearity of the neighbour and the square of its distance from the mixed cell

$$\gamma_{\hat{i},\hat{j},\hat{k}} = \frac{\xi_{\hat{i},\hat{j},\hat{k}}}{||\Delta \boldsymbol{x}_{\hat{i},\hat{j},\hat{k}}||^2} \tag{11.11}$$

This is calculated for each phase, which then allows us to calculate $\dot{m}''$ using (11.2) individually for all mixed cells.

11.2 Geometric VOF advection for phase change

The Volume-Of-Fluid was defined in Chapter 3 and is denoted c in this work. By definition, it is confined to the range $0 \leq c \leq 1$. Geometric VOF advection methods solve an advection equation for c using interface reconstructions and calculating the flux terms based on these reconstructions.

For phase change problems, the VOF advection equation is written

$$\frac{\partial c}{\partial t} + \nabla \cdot (\boldsymbol{u} c) = -\frac{\dot{m}''}{\rho_\ell} \delta_\Gamma\,. \tag{11.12}$$

The source term on the right hand side accounts for the volume change generated during phase change at the interface, which is caused by a difference in specific volumes between phases. When $\dot{m}'' = 0$, the standard VOF advection equation in an incompressible flow is obtained. Note that the tracked phase here is the liquid, as per convention. The equation above is symmetrical for the opposite phase. To illustrate this, assume $c' = 1 - c$. It can then be shown that

$$\frac{\partial c'}{\partial t} + \nabla \cdot (\boldsymbol{u} c') = \frac{\dot{m}''}{\rho_g} \delta_\Gamma\,. \tag{11.13}$$

The geometric VOF advection methods available to the user in PARIS are the Lagrangian Explicit method of Li [39], sometimes referred to as *CIAM* or *LE* and the conservative method of Weymouth and Yue [87]. A consideration to note with standard geometric advection schemes, is that they rely fundamentally on a velocity field that is divergence free ($\boldsymbol{\nabla} \cdot \boldsymbol{u} = 0$) in order to ensure conservation. This poses a problem for phase change problems that clearly have a divergence in the velocity field around the interface, which is evident in the equation for mass conservation (11.1). For more details on the geometric methods to advect VOF functions in divergence free velocity fields, the reader can also refer to [56],[81, p.95].

A novel method is proposed in this work to deal with geometric VOF advection in a discontinuous velocity field. It uses two steps: First, an advection equation is solved for the liquid VOF using a divergence free velocity field, $\boldsymbol{u_\ell}$.

$$\frac{\tilde{c} - c^n}{\Delta t} + \nabla \cdot (\boldsymbol{u}_{\boldsymbol{\ell}}^n c^n) = 0\,. \tag{11.14}$$

This equation can be solved using the geometric advection methods mentioned above.

In the second step, the interface shift due to phase change is then included

$$\frac{c^{n+1} - \tilde{c}}{\Delta t} + \frac{\dot{m}''|^n}{\rho_\ell} = 0\,. \tag{11.15}$$

This equation essentially accounts for phase change by applying a shift of the interface in the normal direction. Each of the two steps will be detailed individually, starting with the first step.

11.2.1 Advecting with a divergence-free liquid velocity

The first step of the procedure is to advect c with the liquid phase velocity, as required by (11.14). The main problem now becomes finding $\boldsymbol{u}_\ell$ in mixed cells. In this work, a novel, yet elegant and robust method was developed for this purpose. Elegance stems from the fact that it is easily implementable into an existing pressure projection solver by adding an additional solve step. The new technique is outlined next and the process is shown schematically in Fig. 11.1.

First, a predicted velocity is obtained by calculating an explicit time step of the momentum terms at time step n in the usual manner, excluding the pressure term

$$\frac{\boldsymbol{u}^* - \boldsymbol{u}^n}{\Delta t} = \frac{1}{\rho_0^n}\left(\boldsymbol{u}^n \cdot \boldsymbol{\nabla}^h \boldsymbol{u}^n + \boldsymbol{\nabla}^h \cdot 2\mu\mathbf{S} + \sigma\kappa^{n+1}\delta_\Gamma^{n+1}\boldsymbol{n}_\Gamma^{n+1}\right) + {}^{\rho}/_{\rho_0}\boldsymbol{g}\,. \tag{11.16}$$

A pressure Poisson equation is now solved to obtain the pressure

$$\boldsymbol{\nabla}^h \cdot \left[\frac{\Delta t}{\rho^{n+1}}\boldsymbol{\nabla}^h p^{n+1}\right] = \boldsymbol{\nabla}^h \cdot \boldsymbol{u}^* - \dot{m}''|^{n+1}\left(\frac{1}{\rho_g} - \frac{1}{\rho_\ell}\right)\delta_\Gamma\,. \tag{11.17}$$

The predicted velocity is corrected to ensure mass conservation

$$\frac{\boldsymbol{u}^{n+1} - \boldsymbol{u}^*}{\Delta t} = -\frac{1}{\rho^{n+1}}\boldsymbol{\nabla}^h p^{n+1}\,. \tag{11.18}$$

This will result in

$$\boldsymbol{\nabla}^h \cdot \boldsymbol{u}^{n+1} = \dot{m}''|^{n+1}\left(\frac{1}{\rho_g} - \frac{1}{\rho_\ell}\right)\delta_\Gamma\,, \tag{11.19}$$

since the system solved in (11.17) was obtained by taking the divergence of (11.18) and using mass conservation (11.1).

The velocity $\boldsymbol{u}$ in the equations above is the one-fluid velocity, which can be seen as some combination of a gas and liquid velocity on mixed cell faces. To obtain $\boldsymbol{u}_\ell$, a simple, yet robust and elegant technique is used. Key to this is the isolation of the phase change contribution to the velocity field, denoted $\tilde{\boldsymbol{u}}^{n+1}$ in a simple, yet conservative and robust manner. We commence by constructing a sub-domain around the interface, with all values taken at time n. A 2D example of this sub-domain construction is showed in Fig 11.2. The sub-domain is delimited on the liquid side of the interface by defining all the cell faces between mixed and liquid cells as domain boundaries on which a no-slip boundary condition is applied. On the other side of the interface,

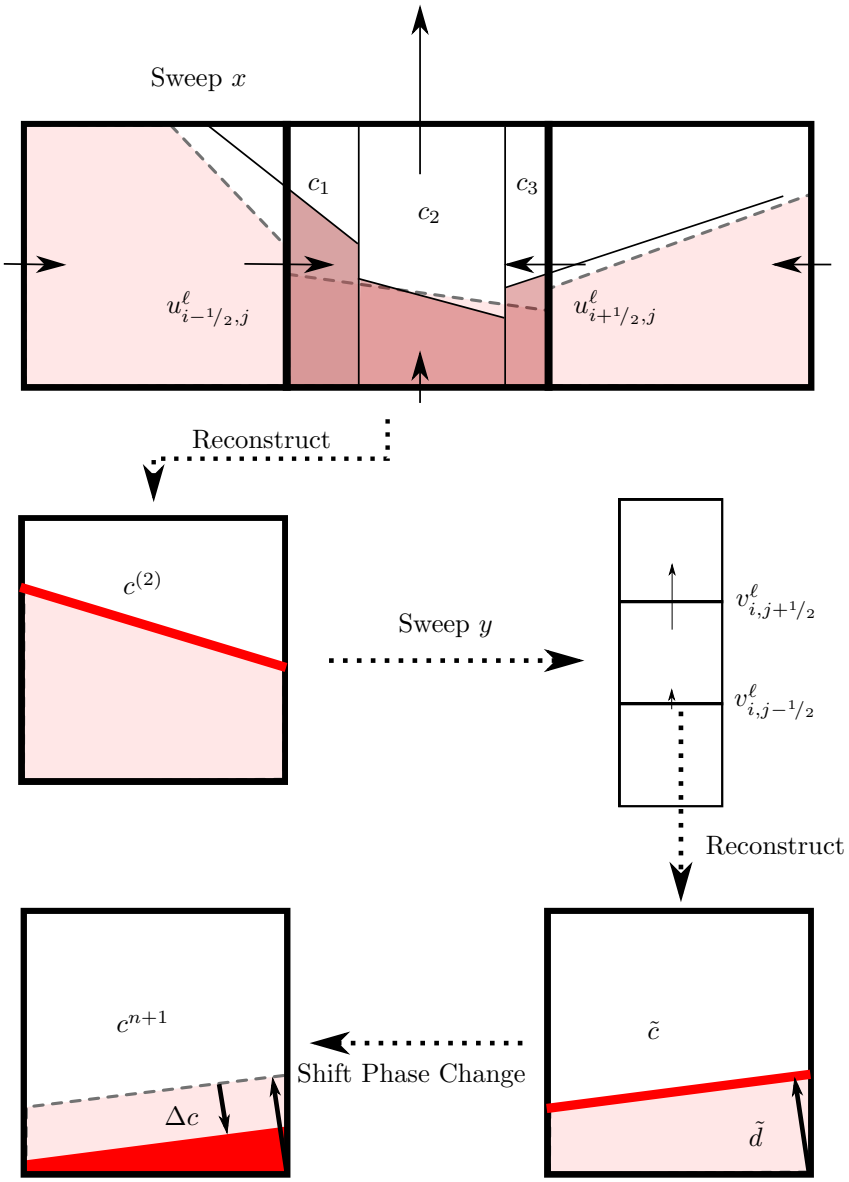

Figure 11.1: Schematic illustration of the VOF advection procedure for phase change. The geometric VOF fluxes are calculated in a split fashion, similar to existing geometric advection techniques, using the liquid velocity $\boldsymbol{u}_{\boldsymbol{\ell}}$. The flux in one direction is accounted for (cell row at the top), after which the interface is reconstructed (middle left). The process is then repeated in the next sweep direction (middle right) and fluxes are calculated based on the newly reconstructed interface after the previous sweep. This process is repeated until all directions have been completed and field $\tilde{c}$ is the result (bottom right). The relative movement of the interface to the liquid is accounted for in the last step by shifting the interface along its normal, resulting in the new VOF field c^{n+1} (bottom left).

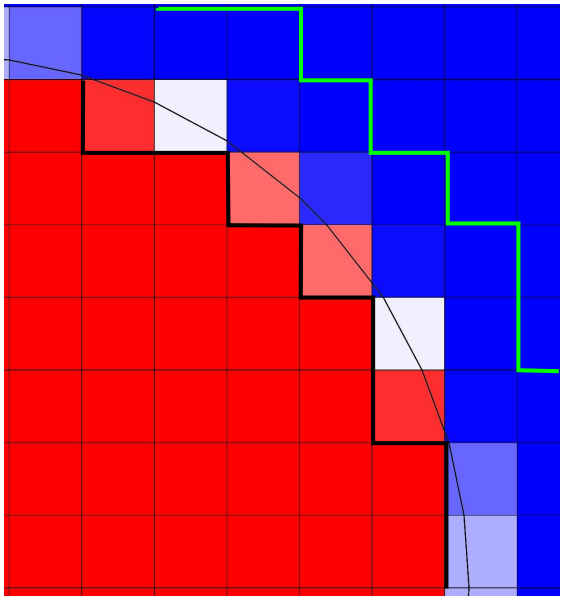

Figure 11.2: A 2D example of the sub-domain construction used to compute $\boldsymbol{u}_\ell$. The colours represent the VOF function: The red is liquid and blue gas. A wall boundary is imposed on the black lines and a free-flow boundary on the bright green lines. A Poisson problem is solved in between these boundaries.

all the cell faces between first and second pure gas cell neighbours are considered as free-flow faces where a fixed pressure is applied with a zero velocity gradient as boundary conditions.

A Poisson problem is set up using the same matrix as in (11.17)

$$\boldsymbol{\nabla}^h \cdot \left[\frac{\Delta t}{\rho^{n+1}} \boldsymbol{\nabla}^h \tilde{p} \right] = \dot{m}''|^{n+1} \left(\frac{1}{\rho_g} - \frac{1}{\rho_\ell} \right) \delta_\Gamma \,, \tag{11.20}$$

with the same phase change source term, but of opposite sign. This equation is solved with the same convergence tolerance as for the previous problem and a velocity field is now obtained on the cell faces of the newly defined sub-domain by using the pressure $\tilde{p}$ from the solution and a similar velocity correction to the one in (11.18)

$$\tilde{\boldsymbol{u}}^{n+1} = -\frac{\Delta t}{\rho^{n+1}} \boldsymbol{\nabla}^h \tilde{p}^{n+1} \,. \tag{11.21}$$

with $\tilde{\boldsymbol{u}}$ a newly obtained velocity field that represents the phase change component in the one-fluid velocity. It is obtained everywhere on the cell faces inside the sub-domain. Note that the value of $\tilde{\boldsymbol{u}}$ before the correction was set to zero, which is also valid everywhere else in the original domain. The divergence free liquid velocity field is now simply obtained by

$$\boldsymbol{u}_\ell^{n+1} = \boldsymbol{u}^{n+1} + \tilde{\boldsymbol{u}} \,. \tag{11.22}$$

By the construction of the sub-domain, the velocity of the tracked phase is extended across the interface for a couple of cells. It also ensures that the velocity field in mixed cells is divergence free. This can easily be shown, since

$$\boldsymbol{\nabla} \cdot \boldsymbol{u}_\ell = \boldsymbol{\nabla} \cdot \boldsymbol{u}^{n+1} + \boldsymbol{\nabla} \cdot \tilde{\boldsymbol{u}} = \dot{m}''' \left(\frac{1}{\rho_g} - \frac{1}{\rho_\ell} \right) \delta_\Gamma - \dot{m}'' \left(\frac{1}{\rho_g} - \frac{1}{\rho_\ell} \right) \delta_\Gamma = 0 \,. \tag{11.23}$$

The first step of the advection procedure (11.14) can now be calculated.

11.2.2 Accounting for phase change

The second step is to account for the change in VOF as a result of phase change. This is illustrated by the last step in 11.1. Another way to think of this is to account for the movement of the interface relative to the liquid phase, bearing in mind that the liquid is the tracked phase. The relative velocity $(\boldsymbol{u}_\Gamma - \boldsymbol{u}_\ell) \cdot \boldsymbol{n}_\Gamma$ comes from the mass conservation interface jump condition

$$\begin{aligned} \rho_\ell \left(\boldsymbol{u}_\ell - \boldsymbol{u}_\Gamma\right) \cdot \boldsymbol{n}_\Gamma &= \dot{m}'' \\ \therefore \left(\boldsymbol{u}_\Gamma - \boldsymbol{u}_\ell\right) \cdot \boldsymbol{n}_\Gamma &= -\frac{\dot{m}''}{\rho_\ell}\,, \end{aligned} \tag{11.24}$$

which explains the origin of the equation for the second step

$$\frac{c^{n+1} - \tilde{c}}{\Delta t} + \frac{\dot{m}''}{\rho_\ell}\delta_\Gamma = 0\,. \tag{11.25}$$

It can now be seen that the equation above can be satisfied by shifting the interface in the normal direction, since the relative velocity at the interface is in the normal direction. Let Δd be the shift of the interface

$$\Delta d = \left(\boldsymbol{u}_\Gamma - \boldsymbol{u}_\ell\right) \cdot \boldsymbol{n}_\Gamma = \frac{\dot{m}''}{\rho_\ell}\frac{\Delta t}{h}\,, \tag{11.26}$$

with h the cell length, which is used here to re-scale the velocity to the local cell coordinate system in which the plane constant is defined.

The new VOF c^{n+1} can now be obtained by rescaling Δd to the local cell coordinate system and using the geometric VOF library in PARIS based on [55]

$$\begin{aligned} \alpha^{n+1} &= \tilde{\alpha} - ||\boldsymbol{m}||\Delta d \ldots 0 \leq \alpha^{n+1} \leq 1 \\ c^{n+1} &= \; f(\alpha^{n+1}, \boldsymbol{m})\,. \end{aligned} \tag{11.27}$$

It is noted here that the movement is capped to avoid over- and undershoots and respect $0 \leq c^{n+1} \leq 1$. When they do occur, the clipped amount is accounted for in the neighbour that is located in the direction of interface movement and mass conservation is still respected.

When this step is completed, (11.12) is now satisfied. In the context of phase change modelling of a pure substance, the energy equation is to be solved in a consistent manner with the above. The discretization and solution of the thermal energy conservation equation is detailed next.

11.3 Energy conservation

A thermal energy conservation equation was added to PARIS to facilitate the simulation of phase change flows. The thermal energy equation was derived in the previous chapter

$$\int_V \frac{\partial\left(\rho c_p T\right)}{\partial t}\, dV + \oint_S \rho c_p T \boldsymbol{u} \cdot \boldsymbol{n}\, dA = \oint_S k \boldsymbol{\nabla} T \cdot \boldsymbol{n}\, dA + \int_V \dot{q}_\Gamma \delta_\Gamma\, dV \tag{11.28}$$

The numerical treatment of the advection and diffusion terms will next be presented separately. The advection term will be discussed first, since it is strongly related to the two step VOF advection method presented in the previous section.

Phase	**Density** $\rho\ [kg.m^3]$	**Specific heat capacity** $c_p\ [kJ.kg^{-1}.K^{-1}]$	**Vol. heat capacity** $C_p\ [kJ.m^{-3}.K^{-1}]$
Gas (vapour)	0.6	2.080	1.248
Liquid	958	4.216	4.039×10^3

Table 11.1: Properties for saturated water at atmospheric conditions

11.3.1 Calculating the energy advection term

A discrete version of (11.28) is written with an explicit time step to illustrate the procedure used in this work to calculate the advection term

$$C_p^{n+1}T^{n+1} - C_p^n T^n|_{adv} = -\Delta t \sum_f C_p^n|_f \, T_f^n u_f^n A_f \,, \tag{11.29}$$

where subscript *adv* indicates that the advection component is considered. The product of density and specific heat capacity was lumped together into a heat capacity per unit volume $C_p = \rho c_p$. The last term represents the thermal energy flux calculated at all f faces, with the area $A_f = h^2$ and face velocity $u_f = \boldsymbol{u} \cdot \boldsymbol{n}_f$ already known in the MAC grid.

The unknowns in (11.29) are therefore $C_p^n|_f \, T_f^n$, the heat capacity and face temperature. It is important to note at this point that care needs to be taken when these face values are calculated. The reason is that the volumetric heat capacity ratio can become very high. Consider the properties of water at atmospheric conditions in Table 11.1. In this case ${}^{C_{p,\ell}}/_{C_{p,g}} \approx 3200$. The energy change in V due to advection (11.29) will therefore be greatly affected by the value used for $C_p|_f$.

A flux-consistent, geometric advection technique is proposed here to deal with this issue. The term flux-consistent is used, since the flux terms in (11.29) are calculated using the same geometric advection procedure as for the VOF function. This process will now be described and is shown schematically in Fig. 11.3. Note that the flux-consistent implementation here is inspired by a similar method already present in PARIS , but applied to the momentum term.

Exactly like the VOF advection, three consecutive sweeps are performed, one for each coordinate direction. Let s be the intermediate sweep counter, so that $s = 1$ corresponds to time step n, $s = 1, 4$ and $s = 4$ corresponds to time step $n + 1$. Before the sweeps start, a thermal energy e_t is calculated for every cell

$$e_t^{(s=1)} = e_t^n = C_p^n T^n \,, \tag{11.30}$$

where the cell temperature is known from the solution at time step n and the volumetric heat capacity in a cell is obtained by using a volume average of the phase heat capacities

$$C_p^{(s=1)} = C_p^n = C_{p,\ell}\, c + C_{p,g}\,(1 - c) \,. \tag{11.31}$$

The direction sweeping process can now commence with the first direction sweep. The starting direction is alternated every time step, just like the VOF advection:

1. The face temperatures, shown as blue dots in Fig. 11.3, are obtained by using a fifth order WENO reconstruction scheme [59], which was freshly implemented in PARIS for the purposes in this work.

2. With the face temperatures known, the geometric process kicks off. Note that the face temperature at the ${}^{-1}/_2$ staggered index is denoted T_f^- and $+$ for the opposite face. The

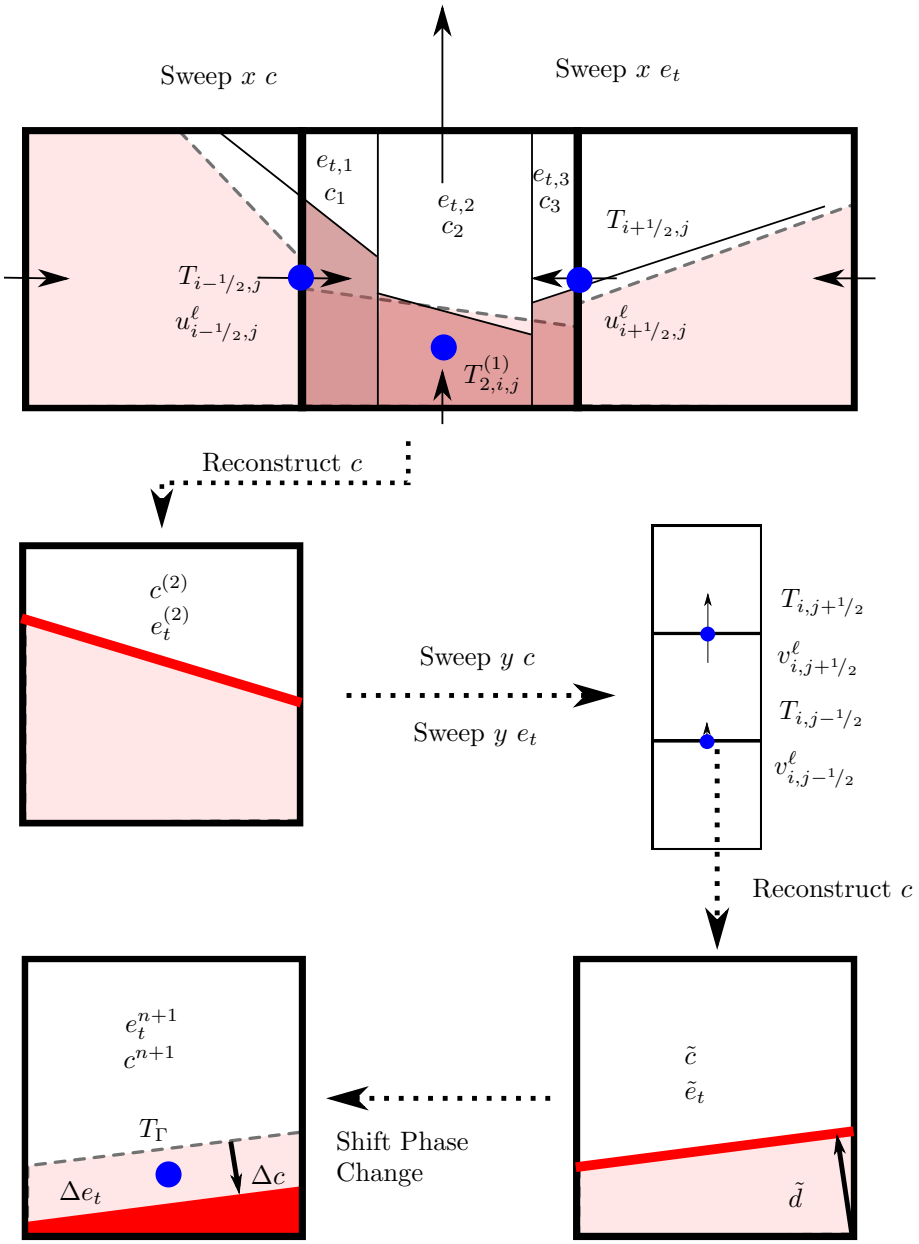

Figure 11.3: Schematic illustration of the consistent VOF and thermal energy advection procedure for phase change. Temperatures are calculated on faces and are indicated with a blue dot. When the interface shift is performed, the interface temperature $T_\Gamma = T_{sat}$ is used to calculate Δe_t.

new cell thermal energy $e_t^{(s+1)}$ is calculated for every sweep and is the sum of three contributions:

$$e_t^{(s+1)} = e_t^1 + e_t^2 + e_t^3 = T_f^- C_{p,1} + T_2^{(s)} C_{p,2} + T_f^+ C_{p,3} \tag{11.32}$$

with the volumetric heat capacities in each volume given by

$$C_{p,b} = C_{p,\ell} c_b + C_{p,g} \left(1 - c_b\right) , \tag{11.33}$$

where $b = 1, 3$ indicates the three volumes. The temperature in the central volume is calculated by using the thermal energy and heat capacity from the previous sweep step

$$T_2^{(s)} = \frac{e_t^{(s)}}{C_p^{(s)}} , \tag{11.34}$$

3. An important remark is that the thermal energy and VOF sweeps are done in tandem for every sweep direction, in the interest of consistency. Before the next direction is swept, the interface is reconstructed from the newly calculated intermediate VOF $c^{(s+1)}$, along with the thermal energy at the same sweep $e_t^{(s+1)}$. This ensures that the heat capacity that is used at each fluxing step is exactly the same as the VOF function. The face temperatures are calculated by using the updated temperature field after each sweep.

After the three coordinate directions have been swept using $\boldsymbol{u}_\ell$, the energy change due to phase change is calculated by

$$\Delta e_t = \Delta c \left(C_{p,\ell} - C_{p,g}\right) T_\Gamma \tag{11.35}$$

Note that in the schematic, a two-dimensional example is given so that two sweeps will be performed. The procedure for the third dimension is identical to the aforementioned two.

11.3.2 Calculating the energy diffusion term

The heat diffusion term needs to be evaluated to integrate (11.28) in time. This is calculated implicitly using a similar approach to Sato and Ničeno [53]. The saturation temperature at the interface is applied directly by solving the diffusion term separately for each phase. By using this technique, the latent heat term does not have to be calculated. The reason is simply that the interface jump condition is satisfied inherently, as the heat flux at the interface is calculated by using the interface temperature, T_Γ. The interface is treated as a boundary, where a Dirichlet boundary condition is specified for the temperature. This is equivalent to solving two heat diffusion equations with constant fluid properties, with the interface an arbitrary boundary separating the two phases in which each respective problem is solved.

First, the phase of a specific node is determined by simply evaluating the VOF function: A cell node is determined to be inside the liquid whenever $c \geq 0.5$, otherwise it is in the gas. Fig. 11.4 shows two 2D stencils used to compute the diffusion term for a liquid (left hand side) and gas (right hand side) node.

Consider the liquid node on the left as an example. The finite volume discretiation of the diffusion term for the 2D cell at position i, j is approximated using the irregular stencil as shown on the left in Fig. 11.4

$$\int_{V_{i,j}} \boldsymbol{\nabla} \cdot \left(k \boldsymbol{\nabla} T\right) dV \approx k_\ell \left(\frac{\nabla_y^h T_{i,j+1/2} - \nabla_y^h T_{i,j-1/2}}{1/2 \left(h + \theta^\ell_{i,j-1/2}\right)} + \frac{\nabla_x^h T_{i+1/2,j} - \nabla_x^h T_{i-1/2,j}}{1/2 \left(\theta^\ell_{i+1/2,j} + h\right)} \right) , \tag{11.36}$$

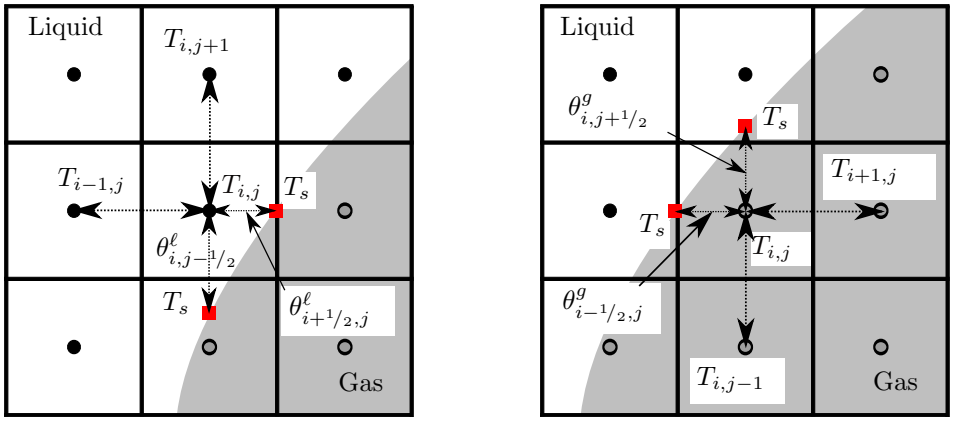

Figure 11.4: Discretisation for temperature neighbouring the interface. On the left the computational stencil for a liquid cell is shown, with the stencil for its neighbour in the gas on the right.

noting that $\Delta x = \Delta y = h$ and $k = k_\ell$ since we are only considering the liquid.

The temperature gradient is approximated using a finite difference. Consider again the liquid node:

$$\boldsymbol{\nabla}^h_x T_{i+1/2,j} = \frac{T_\Gamma - T_{i,j}}{\theta^{\ell}_{i+1/2,j}} \; ; \quad \boldsymbol{\nabla}^h_x T_{i-1/2,j} = \frac{T_{i,j} - T_{i-1,j}}{h} \, . \tag{11.37}$$

For the temperature gradient to the right of the node in question, the interface distance θ^ℓ is used to calculate the finite difference. A standard finite difference is used when the temperature gradient is approximated between two nodes in the same phase.

The distance to the interface from a node is simply taken as the height function in that direction. When the interface configuration is such that a height cannot be obtained in the required direction, the distance is approximated by using a plane reconstruction of the interface in the staggered volume. This is shown in Fig. 11.5. First, the staggered VOF fractions are obtained by considering the plane reconstruction in centered cells. An interface reconstruction is then performed in the staggered cells. With the plane constant known, the interface distance is then calculated with a simple algebraic equation for the intercept of the line connecting the neighbouring nodes and the plane. The distance is capped so that $\epsilon h \leq \theta \leq h$, with a value of $\epsilon = 10^{-3}$ typically used.

11.4 Momentum conservation

Before proceeding to present the solution process, a word is due on the numerical treatment of the momentum conservation equation.

As mentioned before, the idea of calculating the face fluxes in the energy advection equation consistently with the VOF function comes from a similar scheme in PARIS , but applied to the momentum advection term. For the purpose of this work, the two-step advection process was not applied to this momentum conserving scheme due to additional numerical challenges it poses. One challenge is the fact that the momentum control volume is staggered to the pressure and thermal energy control volumes in the MAC grid.

The error introduced with the use of a non-conservative discretization of the momentum equation is only present around the interface, since the phase densities are constant. The effect

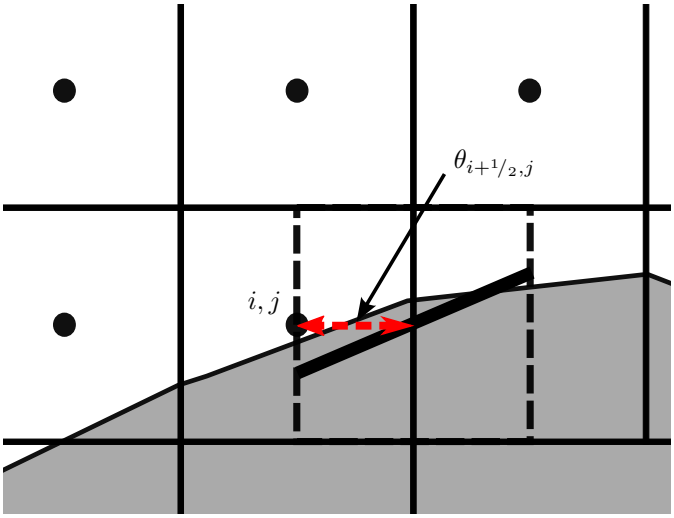

Figure 11.5: Cell i,j will typically not have a height available due to the interface configuration. A plane reconstruction (thick black line) is made in the staggered volume indicated with dashed lines and this reconstruction is used to obtain $\theta_{i+1/2,j}$.

of the error can be seen in the force balance on the interface, (10.18). Without digressing too much from the flow in this chapter, the short summary when this is analyzed is that an incorrect vapour recoil pressure is obtained. However, it is noted that the vapour recoil pressure for water at atmospheric conditions is very small compared to the surface tension pressure jump for typical length scales in phase change flows. The standard non-conservative discretization for momentum in PARIS is therefore used in this work.

The solution procedure for phase change is presented next.

11.5 Phase change solution process

This section provides the time integration procedure and serves to illustrate the order in which the various steps (described above) are taken. Assume that all variables are known at some time step n. When $n = 0$, initial values are provided for the problem.

The time integration scheme used for phase change problems is an explicit, first order time integration scheme. The reason that the second order scheme was not used, was detailed in Chapter 3. The explicit order time integration scheme simply marches in discrete time steps by using variables at time step n to obtain the solution at $n+1$. There are exceptions here, eg. the implicit solution of pressure as well as the energy diffusion term. The viscous diffusion term in the momentum equation can also be solved implicitly.

The time integration order used to solve the governing equations is as follow:

1. The mass transfer rate at the interface, $\dot{m}''|^{n+1}$ is calculated, as explained in Section 11.1.

2. The Energy advection term is calculated with the flux-consistent geometric method presented in 11.3.1. The VOF advection is done simultaneously, so that c^{n+1} is known. All material properties that depend on c can now be calculated (ρ^{n+1}, μ^{n+1}, C_p^{n+1}, κ^{n+1}, δ_Γ^{n+1}, $\boldsymbol{n}_\Gamma^{n+1}$).

3. The contribution of the energy diffusion term is added to the thermal energy equation by solving an implicit form of it. This concludes the thermal energy calculation and T^{n+1} is obtained.

4. The predicted velocity $\boldsymbol{u}^*$ in the momentum equation is calculated, as described in Chapter 3:

$$\frac{\boldsymbol{u}^* - \boldsymbol{u}^n}{\Delta t} = \frac{1}{\rho_0^n}\left(\boldsymbol{u}^n \cdot \boldsymbol{\nabla}^h \boldsymbol{u}^n + \boldsymbol{\nabla}^h \cdot 2\mu\mathbf{S} + \sigma\kappa^{n+1}\delta_\Gamma^{n+1}\boldsymbol{n}_\Gamma^{n+1}\right) + {}^{\rho}/_{\rho_0}\boldsymbol{g}\,. \tag{11.38}$$

   Note that the viscous term can be calculated explicitly $\boldsymbol{\nabla}^h \cdot 2\mu\mathbf{S}|^n$ or implicitly $\boldsymbol{\nabla}^h \cdot 2\mu\mathbf{S}|^{n+1}$.

5. A pressure Poisson equation is then solved for the pressure at $n+1$

$$\boldsymbol{\nabla}^h \cdot \left[\frac{\Delta t}{\rho^{n+1}}\boldsymbol{\nabla}^h p^{n+1}\right] = \boldsymbol{\nabla}^h \cdot \boldsymbol{u}^* - \dot{m}''|^{n+1}\left(\frac{1}{\rho_g} - \frac{1}{\rho_\ell}\right)\delta_\Gamma \tag{11.39}$$

6. The same matrix is used as in the previous step, with an opposite velocity source term coefficient, to obtain $\tilde{p}$

$$\boldsymbol{\nabla}^h \cdot \left[\frac{\Delta t}{\rho^{n+1}}\boldsymbol{\nabla}^h \tilde{p}^{n+1}\right] = \dot{m}''|^{n+1}\left(\frac{1}{\rho_g} - \frac{1}{\rho_\ell}\right)\delta_\Gamma\,, \tag{11.40}$$

7. The one fluid velocity $\boldsymbol{u}$ is obtained with a correction step using p^{n+1}

$$\frac{\boldsymbol{u}^{n+1} - \boldsymbol{u}^*}{\Delta t} = -\frac{1}{\rho^{n+1}}\boldsymbol{\nabla}^h p^{n+1} \tag{11.41}$$

8. In a similar way $\tilde{\boldsymbol{u}}^{n+1}$ is obtained from a correction step using $\tilde{p}$

$$\tilde{\boldsymbol{u}}^{n+1} = -\frac{\Delta t}{\rho^{n+1}}\boldsymbol{\nabla}^h \tilde{p}^{n+1}\,. \tag{11.42}$$

9. The divergence free liquid velocity that is used for the flux-consistent VOF and energy advection can then be obtained from

$$\boldsymbol{u}_\ell^{n+1} = \boldsymbol{u}^{n+1} + \tilde{\boldsymbol{u}}\,. \tag{11.43}$$

All variables have now been solved at time step $n+1$ and the cycle can repeat for the next time step. The numerical method presented here has been implemented in PARIS with full parallel processing capability for three dimensional flow.

Chapter 12

Results

In this chapter the results will be presented of validation tests performed with the novel numerical method for phase change modelling. The test cases will involve 2D and 3D cases. Both accuracy and robustness will be demonstrated. The numerical method was implemented in PARIS with full parallel processing capability in three spatial dimensions using the MPI libraries [22].

12.1 Buoyancy driven flow

The conservation of thermal energy is a novel addition to PARIS , which allows the simulation of buoyancy driven flows using the Boussinesq approximation. Before proceeding to quantitative benchmark tests, a case is set up to demonstrate the ability of PARIS to simulate buoyancy driven flows as well as to verify the robust operation of the numerical implementation. The case models a so-called *lava lamp*: A container, filled with two fluids is heated from the bottom. The one wax-like fluid has a larger density than the other at room temperature, but also has a larger thermal expansion coefficient. This causes a buoyancy force when the fluid temperature surpasses some critical point and causes the wax-like fluid to rise. As it moves away from the bottom, it cools again due to thermal conduction through the container walls to the environment. Eventually is will cool enough so that it is no longer buoyant and will descend back down to the bottom of the domain. The process then repeats.

Gyüre and Jánosi studied such a process experimentally [25], to evaluate its validity as a model for convection in the Earth's mantle. They used a Silicone fluid in NaCl solution. The fluid parameters from their study is used and is presented in Table 12.1.

Property	**Units**	**NaCl solution**	**Silicone fluid**
Density ρ	$[kg.m^3]$	1074	1080
Specific heat c_p	$[kJ.kg^{-1}.K^{-1}]$	3993	1591
Viscosity μ	$[Pa.s]$	1.08×10^{-3}	0.50
Thermal conductivity k	$[W.m^{-1}.K^{-1}]$	0.596	0.146
Surface tension* σ	$[N.m^{-1}]$	0.001	0.001
Gravitational constant, $\boldsymbol{g}$	$[m.s^{-2}]$	$(0\boldsymbol{i}, -9.81\boldsymbol{j}, 0\boldsymbol{k})$	$(0\boldsymbol{i}, -9.81\boldsymbol{j}, 0\boldsymbol{k})$

Table 12.1: Fluid properties from Gyüre and Jánosi for the buoyancy driven flow problem. *Note that the surface tension coefficient was not mentioned in their paper and this value was randomly selected.

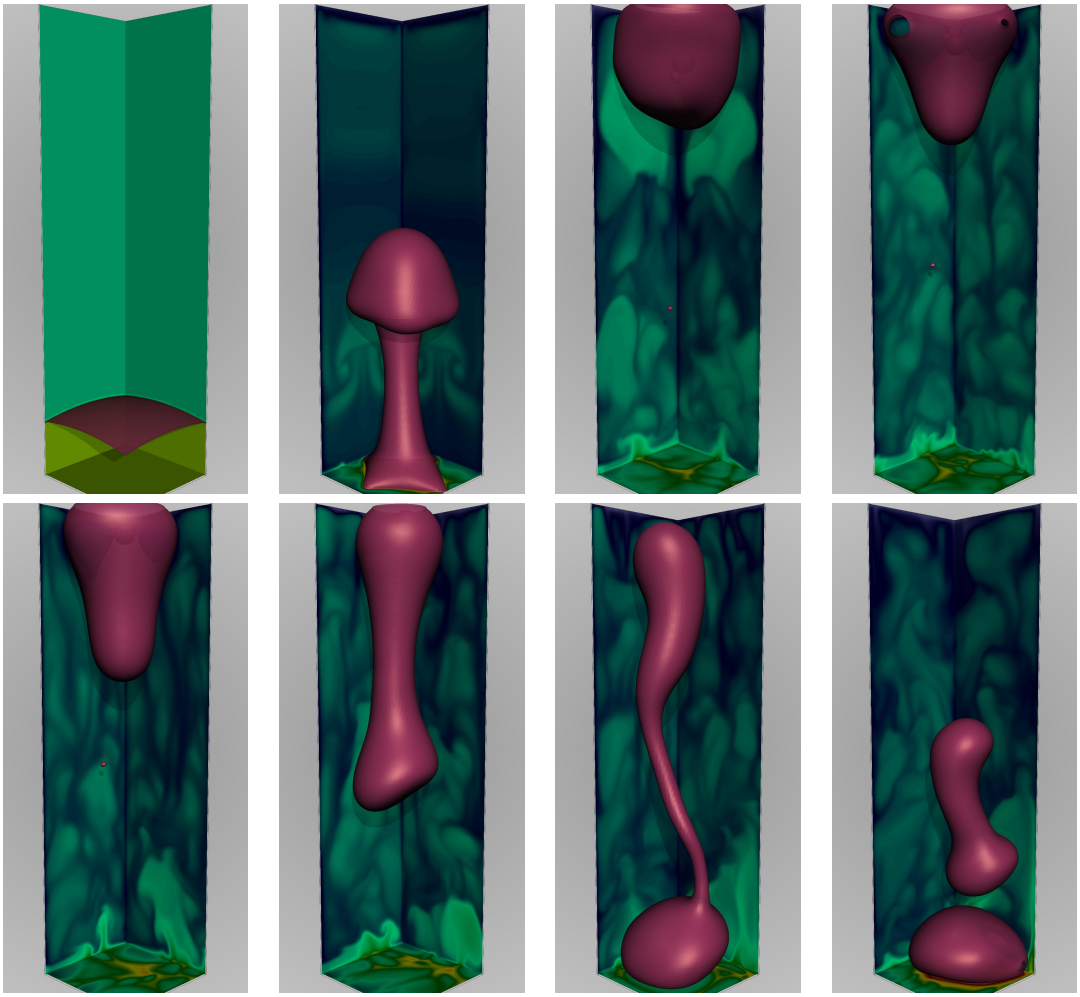

Figure 12.1: A time sequence presentation of a buoyancy driven flow. The purple surface indicates the $c = 0.5$ iso-surface, which is a representation of the interface between a wax-like fluid and a salt solution. The colour scale on the walls represent temperature in a range between $42°C$ and $48°C$.

A three dimensional domain of $L_x \times L_y \times L_z = 100\,mm \times 400\,mm \times 100\,mm$ is filled with these two fluids. The origin of the coordinate system used for the domain is in one of its bottom corners. The silicone fluid is initialized at a temperature of $55°C$. The shape of initialisation is a spherical cap, which is formed by the intersection of the domain and a sphere of radius $258\,mm$ with its origin at $x = 46\,mm$, $y = -200\,mm$ and $z = 48\,mm$. Note that a slight asymmetry is introduced in the initialisation. The simulation was run using $64 \times 256 \times 64$ grid points in parallel on $2 \times 16 \times 2$ processors.

A Dirichlet boundary condition for the temperature is used on all of the domain boundaries, with no-slip wall conditions for the flow. The temperatures on the side walls are $T = 40°C$, with the bottom at $T = 90°C$ and the top at $T = 15°C$. The simulated time was more than $600\,s$, including several cycles of the wax fluid, or part thereof, floating up, cooling down and

descending back down. A time sequence is shown in Fig. 12.1. Fig. 12.2 shows two plots from the simulation: The thermal energy in each phase, which is normalized by its initial value and the y-momentum in each phase. It can be seen that the initial energy was above the equilibrium value in the domain and that heat left the domain through the walls. The momentum in the y-direction is constantly exchanged between phases, as a result of the buoyancy force.

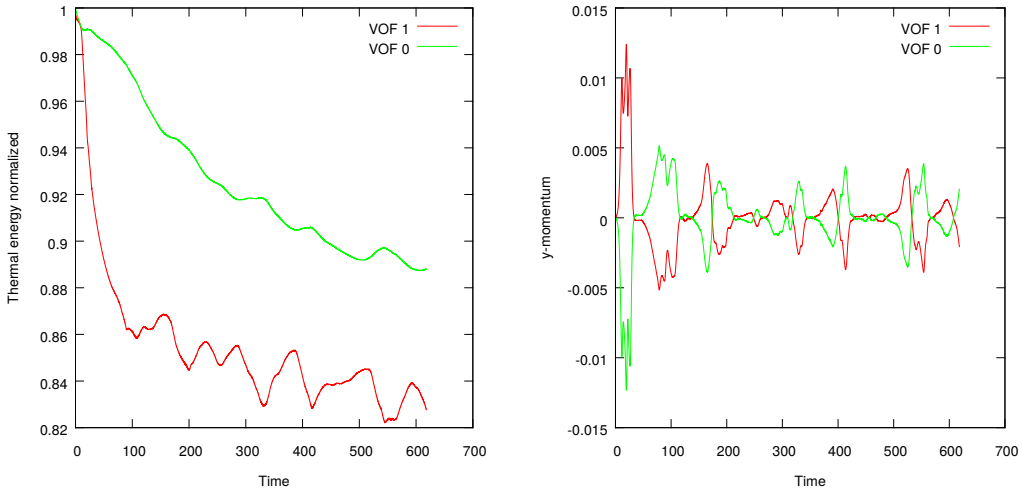

Figure 12.2: The plot on the left shows the time evolution of thermal energy in the two phases. The energies are normalized with their respective initial values. The plot on the right shows the time evolution of the y-momentum in each phase. In both plots the VOF 1 and VOF 0 phases are respectively the wax-like fluid and the salt solution.

This offers a qualitative proof of the robustness and mass conservation of the parallel implementation in PARIS .

12.2 Two-dimensional droplet evaporating test

One crucial aspect of the novel numerical method is the proposed two-step VOF advection procedure. This includes the correct calculation of a divergence free liquid velocity and subsequent phase change adjustment to ensure mass conservation. A two-dimensional evaporating droplet is modelled to validate this part of the implementation. Therefore, the discretization errors that may be present from the mass transfer rate calculations are removed by specifying a constant mass transfer rate of $\dot{m}'' = 0.05$.

A two-dimensional, circular liquid droplet with initial radius $R = 0.23$ is initialized in the center of a square domain of unit length. The units in this problem are irrelevant and we can consider the problem dimensionless. The boundaries are given an outflow boundary condition. The constant mass transfer rate causes the droplet to evaporate. The radius evolution over time is simply

$$R(t) = R_0 - \dot{m}'' t\,. \tag{12.1}$$

Three grid resolutions were used: $N_x = 32, 64$ and 128 with respective time step sizes of $t = 0.002\,s$, $t = 0.001\,s$ and $t = 0.0005\,s$. The time evolution of the droplet volume is shown in

Fig. 12.3 and compared to the analytical solution. As shown, an accurate solution is achieved on all meshes. Fig. 12.4 shows a time sequence of the droplet evolution for the finest resolution. The velocity magnitude is shown, revealing resulting radial flow patterns. The velocity field is symmetric throughout.

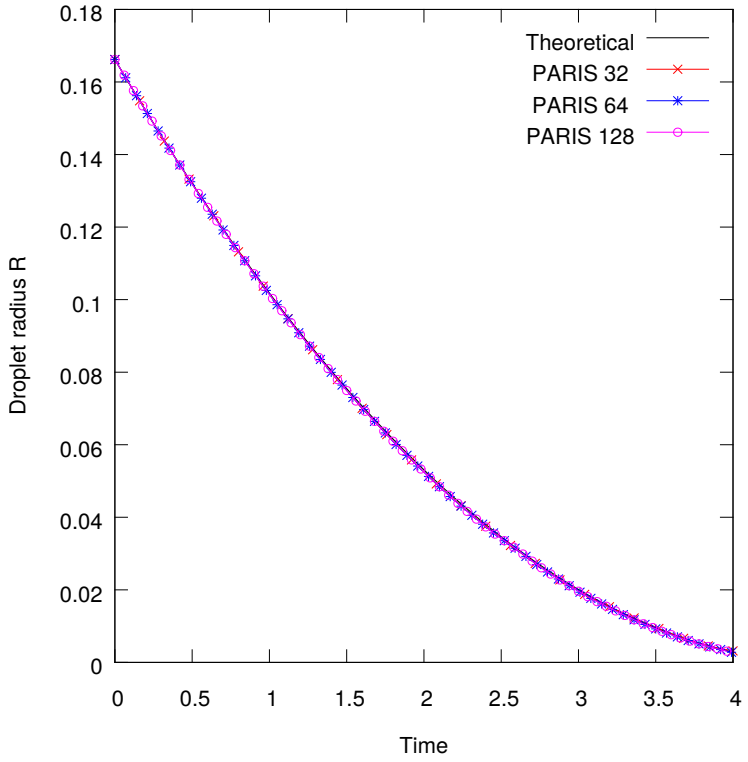

Figure 12.3: The volume evolution an evaporating cylinder in 2D with constant rate of evaporation.

In Fig. 12.5, the velocity fields for the flux-consistent VOF and energy advection method are shown.

12.3 Stefan problem

The Stefan problem was used by Welch and Wilson [86] to validate their VOF base method and has since then often been used to validate incompressible phase change methods [24, 53]. In this problem, a liquid at saturation temperature is initially at rest. A thin vapour layer is present between the liquid and a wall, which is at a fixed, elevated temperature of T_{sup} degrees above the saturation temperature, $T_{wall} = T_{sat} + T_{sup}$. Gravity is neglected and an outflow boundary condition is used opposite the heated wall.

The temperature gradient between the wall and the interface, which is at saturated temperature, causes phase change and the vapour layer to grow in time. The liquid is pushed out of the domain by the growing vapour layer. Let the thickness of the vapour layer be δ. An analytical solution is available for the evolution of the interface thickness and temperature profile [86]. The interface thickness is given by

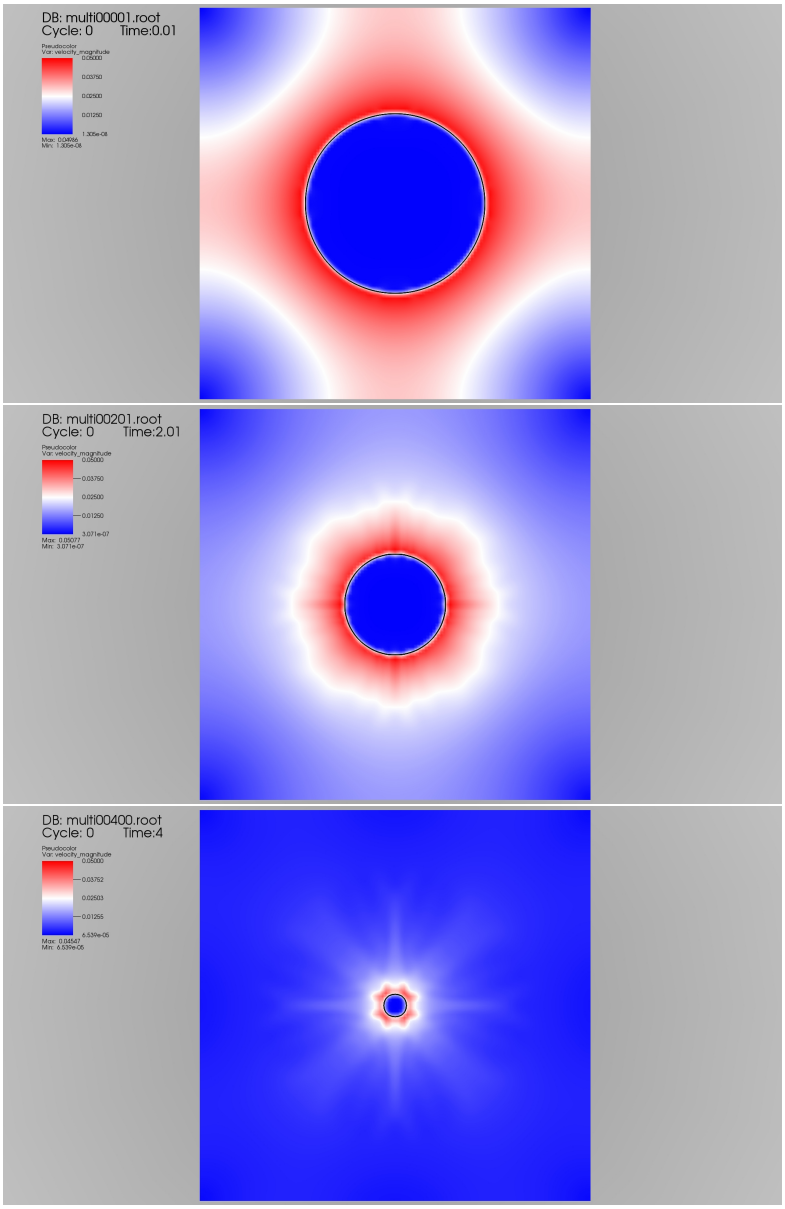

Figure 12.4: A time series showing the velocity magnitude for the finest resolution simulation.

$$\delta(t) = 2\lambda\sqrt{\alpha t}\,, \tag{12.2}$$

with t the time and $\alpha = {}^{k_g}/_{\rho_g c_{p,g}}$ the thermal diffusivity of the vapour phase. λ is found by solving the transcendental equation

$$\lambda \exp(\lambda^2) erf(\lambda) = \frac{c_{p,g} T_{sup}}{h_{fg}\sqrt{\pi}}\,. \tag{12.3}$$

A two-dimensional test case was defined with a domain size of $10\,mm$, a $T_{sup} = 10\,K$ su-

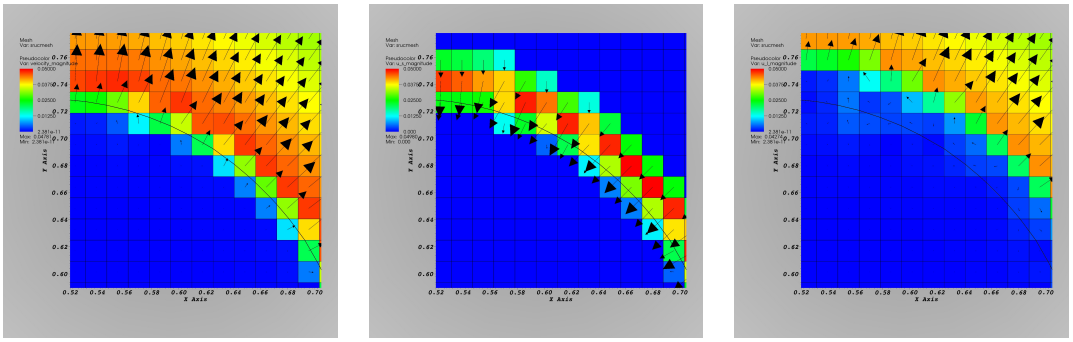

Figure 12.5: The three images show the interface with the velocity vectors. The color scale represents the velocity magnitude. From left to right, the one-fluid velocity $\boldsymbol{u}$, the velocity from the inverse problem in the sub-domain $\tilde{\boldsymbol{u}}$ and liquid velocity $\boldsymbol{u}_\ell$ are shown.

Property	**Units**	**Liquid**	**Vapour**
Density ρ	$[kg.m^3]$	958	0.6
Specific heat c_p	$[kJ.kg^{-1}.K^{-1}]$	4216	2080
Viscosity μ	$[Pa.s]$	2.82×10^{-4}	1.23×10^{-5}
Thermal conductivity k	$[W.m^{-1}.K^{-1}]$	0.68	0.025
Surface tension σ	$[N.m^{-1}]$	0.059	-

Table 12.2: Properties for saturated water at atmospheric conditions

perheat and fluid properties for water at atmospheric conditions. These properties are given in Table 12.2

The problem was set up with these fluid properties in PARIS . The initial temperature field was T_{sat} in the liquid and a linear profile from the interface to the wall temperature. Three grid spacings were used on the $10\,mm$ domain: $N_x = 64, 128, 256$ with respective time step sizes of $t = 0.002\,s$, $t = 0.001\,s$ and $t = 0.0005\,s$. The initial vapour layer thickness was taken as $322.5\,\mu m$, which corresponds to a time $t = 0.282435\,s$, if the vapour layer would have grown from zero thickness at time $t = 0\,s$. The simulated time was $10s$.

The theoretical solution of the evolution of the interface thickness was obtained by solving (12.3) numerically with a relative convergence error of 10^{-6} for λ. The results from PARIS for the three grid resolutions are plotted in Fig. 12.6. An excellent agreement was obtained. The relative error of the interface position at $t = 10\,s$ for the three grid resolutions are presented in Table 12.3. The theoretical solution for $t = 10\,s$ is $\delta(10) = 1.919 \times 10^{-3}\,m$.

The results show an error of less that 1% for the coarsest grid. Since the errors are so small, the rate of convergence will be determined with a more demanding test case.

Grid points	δ PARIS	Relative error %
$N_x = 64$	1.93088×10^{-3}	0.62
$N_x = 128$	1.92650×10^{-3}	0.39
$N_x = 256$	1.92349×10^{-3}	0.23

Table 12.3: Relative errors for Stefan problem interface location at $t = 10\,s$.

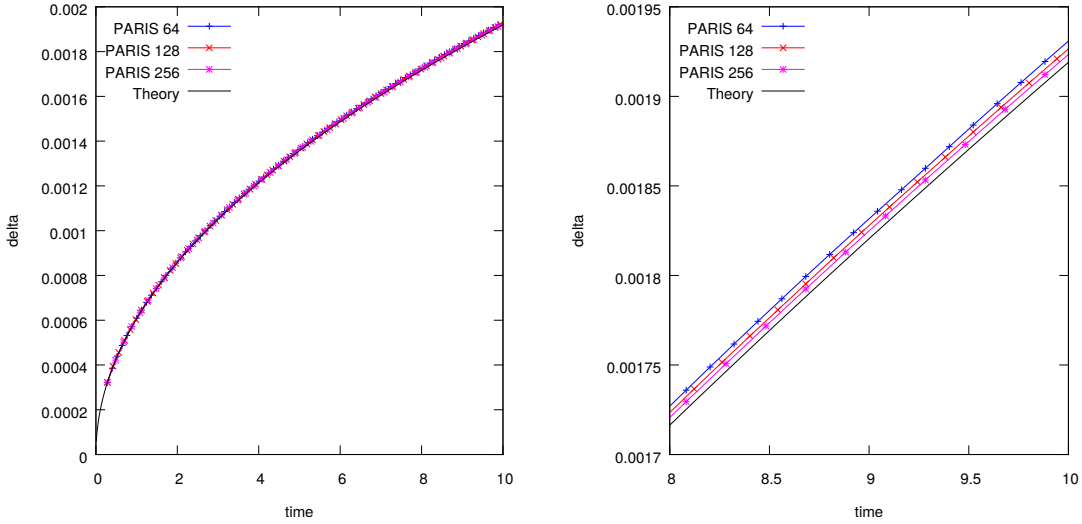

Figure 12.6: The interface time evolution results for the Stefan problem.

12.4 Bubble in superheated liquid

A more demanding test case, is that of a gas bubble at saturated temperature in a superheated liquid. The superheated temperature is denoted T_∞ and no gravity force is applied. There is an analytical solution to the problem assuming spherical symmetry, obtained by Scriven [58]. The solution gives the bubble radius R as

Property	**Units**	**Liquid**	**Vapour**
Density ρ	$[kg.m^3]$	2.5	0.25
Specific heat c_p	$[J.kg^{-1}.K^{-1}]$	2.5	1.0
Viscosity μ	$[Pa.s]$	7.0×10^{-3}	7.0×10^{-4}
Thermal conductivity k	$[W.m^{-1}.K^{-1}]$	0.07	0.007
Surface tension σ	$[N.m^{-1}]$	0.001	0.001
Latent heat h_{fg}	$[J.kg^{-1}]$	100.0	100.0

Table 12.4: Properties for the bubble in superheated liquid case.

$$R = 2\,\beta_g \sqrt{\frac{k_\ell}{c_{p,\ell}\rho_\ell} t} \tag{12.4}$$

with t the time and the fluid properties as defined before. The value of β_g, sometimes referred to as the "growth constant" is obtained by solving

$$\frac{\rho_\ell c_{p,\ell}\left(T_\infty - T_{sat}\right)}{\rho_g\left(h_{fg} + \left(c_{p,\ell} - c_{p,g}\right)\left(T_\infty - T_{sat}\right)\right)} = 2\,\beta_g^2 \int_0^1 exp\left(-\beta_g^2\left(\left(1-\zeta\right)^{-2} - 2\left(1 - \frac{\rho_g}{\rho_\ell}\right)\zeta - 1\right)\right) d\zeta \tag{12.5}$$

The solution is obtained numerically using the native numerical tools in the GNU package OCTAVE . The temperature field is then given by

$$
\begin{aligned}
T(r < R) &= T_{sat} \\
T(r > R) &= T_{\infty} - 2\,\beta_g^2 \left(\frac{\rho_g \left(h_{fg} + \left(c_{p,\ell} - c_{p,g} \right) \left(T_{\infty} - T_{sat} \right) \right)}{\rho_\ell c_{p,\ell}} \right) \\
&\int_{1-{}^{R}/_{r}}^{1} exp\left(-\beta_g^2 \left((1-\zeta)^{-2} - 2\left(1 - \frac{\rho_g}{\rho_\ell} \right) \zeta - 1 \right) \right) d\zeta
\end{aligned}
\tag{12.6}
$$

The problem can be characterized by the Jacob number, given by

$$
Ja = \frac{\rho_\ell c_{p,\ell} \left(T_{\infty} - T_{sat} \right)}{\rho_g h_{fg}} \,. \tag{12.7}
$$

A test case is defined with fluid properties given in Table 12.4. Note that these properties do not correspond to a specific fluid, but was chosen for the purposes of a test with ${}^{\rho_\ell}/_{\rho_g} = {}^{\mu_\ell}/_{\mu_g} = {}^{k_\ell}/_{k_g} = 10$. The heat capacity ratio is ${}^{c_{p,\ell}}/_{c_{p,g}} = 2.5$.

The saturated temperature is $T_{sat} = 1\,K$ with the temperature at infinity in the liquid $T_{\infty} = 3\,K$. This results in $Ja = 0.5$. A bubble of initial radius $R(t_0) = 0.12$ is placed in the center of a unit cube. The initial temperature is taken from the analytical solution and the simulation is run for a time $t_f \approx 4 \times t_0$, with t_f the final time. The time t_0 corresponds to the time when a bubble of zero initial radius reached the value of the initial value used in the simulation, $R(t_0) = 0.12$.

Grid points	Radius R PARIS	Relative error %
$N = 64^3$	2.228×10^{-1}	7.85
$N = 128^3$	2.315×10^{-1}	4.07
$N = 256^3$	2.366×10^{-1}	1.95

Table 12.5: Relative errors for the bubble radius R at $t = 4\,t_0$.

Three test cases were run: $N = 64^3, 128^3, 256^3$ with respective time step sizes of $t = 0.01\,s$, $t = 0.005\,s$ and $t = 0.0025\,s$. The time evolution of the bubble radius in the simulations is compared to the theoretical value in Fig. 12.7. The theoretical value of the bubble radius at the final time was determined by the analytical solution: $R(t_f = 2.2156\,s) = 0.2413$. The values from the simulations are given in Table 12.5, along with the relative error to the theoretical value.

The rate of convergence on the bubble radius error is of order 1.

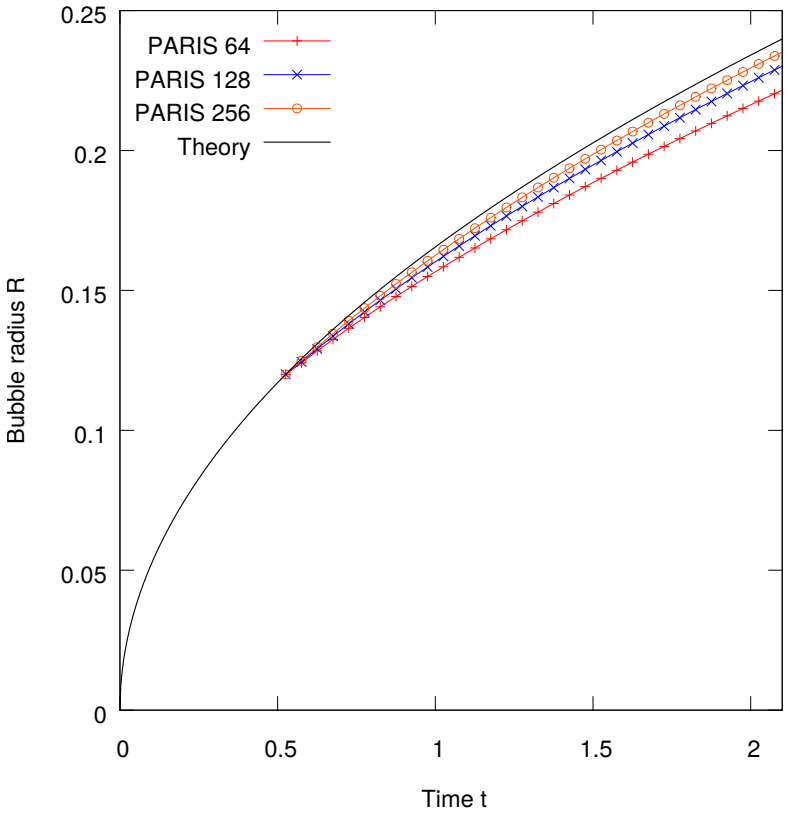

Figure 12.7: The time evolution of the bubble radius for a bubble at saturated temperature in a superheated liquid.

Chapter 13

Conclusion: Part II

13.1 Summary

The Direct Numerical Simulation of flows with phase change was studied. The governing equations were derived, with specific attention given to the effects of phase change at the interface. The velocity jump condition due to phase change was obtained by employing a control volume analysis around the interface.

This velocity jump condition poses a challenge in terms of the numerical implementation of some conventional geometric VOF advection techniques that rely on a smooth, divergence–free velocity field. From a detailed literature review, it was found that geometric VOF advection techniques for flows with phase change are rare and not well described. A novel method was proposed. This method relies only on the VOF function to calculate all required values to simulate phase change problems. The planar interface reconstruction (PLIC), based on the MYC scheme [3] and geometric volume calculations in mixed cells [55], is used extensively in this method.

To deal with the velocity jump at the interface, a novel two-step VOF advection method is employed. In the first step, the interface is advected with a divergence free liquid velocity, which is obtained from the solution of a Poisson problem that decomposes the one-fluid velocity into a liquid velocity and a phase-change component. In the second step, the phase change component is accounted for with an explicit interface shift in the local normal direction.

The geometric treatment of VOF advection is applied consistently to the thermal energy advection term. The thermal energy diffusion term is solved implicitly, using a similar technique to Sato and Ničeno [53], where an asymmetric stencil is used to apply the interface temperature directly.

The method was implemented in PARIS , with full parallel computation capability and was tested using several benchmark test cases. The two-step VOF advection method was tested on a two-dimensional evaporating droplet. The results on three different grids were indistinguishable and showed excellent agreement to the $^1/_{t^2}$ evolution of the volume. The one-dimensional Stefan problem was solved to excellent accuracy. A three dimensional bubble at saturated temperature in a superheated liquid with $Ja = 0.5$ was simulated at three different grid resolutions. A first order spatial convergence rate was observed on the numerical method.

An outlook on the numerical method as well as recommendations for future work will be provided in the next section.

13.2 Outlook and recommendations for future work

The numerical method presented is suitable for implementation in codes which use uniform, Cartesian grids. It can be used for a variety of problems in its present implementation in PARIS, but the method may benefit if the following work is performed:

- Assessing the accuracy of the interface normal temperature gradient calculation. This may provide some insight on the first order spatial convergence rate.
- Improving the time convergence accuracy: The present, explicit time integration scheme is first order in time. A suitable second order scheme, which does not suffer from the problem presented in Chapter 3, can be implemented.

It may be useful to create some benchmark three-dimensional test case to compare the method to previous work. One-dimensional problems, like the Stefan problem, have become a standard when evaluating methods, but for several aspects of general methods it is required to have more stringent test cases where complex, three-dimensional effects can be evaluated. The bubble in superheated liquid in a three–dimensional domain can be used for this purpose. It will also be interesting to test more complex physical problems. A candidate case can be three–dimensional film boiling at industrial conditions.

Industrial problems often include modeling complex geometries and may require special contact line dynamics. Contact line models that rely on a modification of the VOF boundary condition should be implementable to the present method with relative ease, since the VOF field is used as a basis for all calculations.

One method to introduce arbitrary boundaries in uniform, Cartesian grids is the embedded or immersed boundary method, of which a review is given by Mittal [40]. This approach may be feasible with the method presented here, but special care will have to be given to the consistent VOF and energy-advection in cut boundary cells. Another approach for complex geometries is to use unstructured grids. Even though some of the conceptual ideas in this method may be applied, this will be a significant task. One reason is that geometric VOF advection techniques on unstructured grids introduce a remarkable amount of computational complexity to ensure conservation.

Bibliography

[1] D. K. Agarwal, S. W. J. Welch, G. Biswas, and F. Durst, *Planar simulation of bubble growth in film boiling in near-critical water using a variant of the VOF method*, Journal of heat transfer, 126 (2004), pp. 329–338.

[2] P. Andriot, P. Chapron, V. Lambert, and F. Olive, *Influence of melting on shocked free surface behaviour using Doppler laser interferometry and X-ray densitometry*, Elsevier Science The Netherlands, 1983, pp. 277–280.

[3] E. Aulisa, S. Manservisi, R. Scardovelli, and S. Zaleski, *Interface reconstruction with least-squares fit and split advection in three-dimensional Cartesian geometry*, Journal of Computational Physics, 225 (2007), pp. 2301–2319.

[4] S. Bnà, S. Manservisi, R. Scardovelli, P. Yecko, and S. Zaleski, *VOFI - A library to initialize the volume fraction scalar field*, Computer Physics Communications, 200 (2016), pp. 291–299.

[5] A. Bourlioux, *A coupled level-set volume-of-fluid algorithm for tracking material interfaces*, in proceedings of the 6th international symposium on computational fluid dynamics, Lake Tahoe, CA, vol. 15, 1995.

[6] J. U. Brackbill, D. B. Kothe, and C. Zemach, *A continuum method for modeling surface tension*, Journal of Computational Physics (ISSN 0021-9991), vol. 100, no. 2, June 1992, p. 335-354., 100 (1992), pp. 335–354.

[7] C. E. Brennen, *Cavitation and Bubble Dynamics*, Oxford engineering science series, Oxford University Press, 1995.

[8] E. Can and A. Prosperetti, *A level set method for vapor bubble dynamics*, Journal of Computational Physics, Volume 231, Issue 4, p. 1533-1552., 231 (2012), pp. 1533–1552.

[9] Y. A. Çengel and M. A. Boles, *Thermodynamics: An Engineering Approach*, McGraw-Hill series in mechanical engineering, McGraw-Hill, 2007.

[10] R. K. C. Chan and R. L. Street, *A Computer Study of Finite-Amplitude Water Waves*, Journal of Computational Physics, 6 (1970), pp. 68–94.

[11] A. J. Chorin, *On the convergence of discrete approximations to the Navier-Stokes equations*, Mathematics of computation, 23 (1969), pp. 341–353.

[12] I. M. Cohen and P. K. Kundu, *Fluid Mechanics*, Fluid Mechanics Series, Elsevier Science, 4 ed., 2007.

[13] T. De Rességuier, E. Lescoute, G. Morard, and F. Guyot, *Dynamic Fragmentation as a Possible Diagnostic for High Pressure Melting in Laser Shock-Loaded Iron*, Shock Compression of Condensed Matter 2009: Proceedings of the American Physical Society Topical Group on Shock Compression of Condensed Matter. AIP Conference Proceedings, 1195 (2009), pp. 1007–1010.

[14] R. DeBar, *Fundamentals of the KRAKEN code*, tech. rep., Lawrence Livermore Laboratory, UCIR-760, 1974.

[15] C. F. Delale, S. Nas, and G. Tryggvason, *Direct numerical simulations of shock propagation in bubbly liquids*, Physics of Fluids, Volume 17, Issue 12, pp. 121705-121705-4 (2005)., 17 (2005), pp. 121705–121705.

[16] J.-M. Delhaye, *Jump conditions and entropy sources in two-phase systems. Local instant formulation*, International Journal of Multiphase Flow, 1 (1974), pp. 395–409.

[17] O. Durand and L. Soulard, *Mass-velocity and size-velocity distributions of ejecta cloud from shock-loaded tin surface using atomistic simulations*, Journal of Applied Physics, Volume 117, Issue 16, id.165903, 117 (2015), p. 165903.

[18] A. Esmaeeli and G. Tryggvason, *Computations of explosive boiling in microgravity*, Journal Of Scientific Computing, 19 (2003), pp. 163–182.

[19] A. Esmaeeli and G. Tryggvason, *Computations of film boiling. Part I: numerical method*, International journal of heat and mass transfer, 47 (2004), pp. 5451–5461.

[20] R. P. Fedkiw, T. Aslam, B. Merriman, and S. Osher, *A Non-oscillatory Eulerian Approach to Interfaces in Multimaterial Flows (the Ghost Fluid Method)*, Journal of Computational Physics, 152 (1999), pp. 457–492.

[21] D. Fuster, K. Pham, and S. Zaleski, *Stability of bubbly liquids and its connection to the process of cavitation inception*, Physics of Fluids, 26 (2014), p. 042002.

[22] E. Gabriel, G. E. Fagg, G. Bosilca, T. Angskun, J. J. Dongarra, J. M. Squyres, V. Sahay, P. Kambadur, B. Barrett, A. Lumsdaine, R. H. Castain, D. J. Daniel, R. L. Graham, and T. S. Woodall, *Open MPI: Goals, Concept, and Design of a Next Generation MPI Implementation*, in Proceedings, 11th European PVM/MPI Users' Group Meeting, Budapest, Hungary, September 2004, pp. 97–104.

[23] F. Gibou, R. P. Fedkiw, L.-T. Cheng, and M. Kang, *A Second-Order-Accurate Symmetric Discretization of the Poisson Equation on Irregular Domains*, Journal of Computational Physics, Volume 176, Issue 1, pp. 205-227 (2002)., 176 (2002), pp. 205–227.

[24] G. Guédon, *Two-Phase Heat and Mass Transfer Modeling: Flexible Numerical Methods for Energy Engineering Analyses*, PhD thesis, Politecnico Di Milano, 2013.

[25] B. Gyüre and I. M. Jánosi, *Basics of lava-lamp convection*, Physical Review E, vol. 80, Issue 4, id. 046307, 80 (2009), p. 046307.

[26] F. H. Harlow and J. E. Welch, *Numerical Calculation of Time-Dependent Viscous Incompressible Flow of Fluid with Free Surface*, Physics of Fluids, Volume 8, Issue 12, p.2182-2189, 8 (1965), pp. 2182–2189.

[27] A. HARTEN, S. OSHER, B. ENGQUIST, AND S. CHAKRAVARTHY, *Some Results On Uniformly High-Order Accurate Essentially Nonoscillatory Schemes*, Applied Numerical Mathematics, 2 (1986), pp. 347–377.

[28] M. HERRMANN, *A parallel Eulerian interface tracking/Lagrangian point particle multi-scale coupling procedure*, Journal of Computational Physics, 229 (2010), pp. 745–759.

[29] J. A. HEYNS, A. G. MALAN, T. M. HARMS, AND O. F. OXTOBY, *A weakly compressible free-surface flow solver for liquid-gas systems using the volume-of-fluid approach*, Journal Of Computational Physics, 240 (2013), pp. 145–157.

[30] C. W. HIRT AND B. D. NICHOLS, *Volume of fluid (VOF) method for the dynamics of free boundaries*, Journal of Computational Physics, vol. 39, Jan. 1981, p. 201-225. Research sponsored by the U.S. Department of Energy and Electric Power Research Institute;, 39 (1981), pp. 201–225.

[31] G. HUBER, S. TANGUY, M. SAGAN, AND C. COLIN, *Direct numerical simulation of nucleate pool boiling at large microscopic contact angle and moderate Jakob number*, International Journal Of Heat And Mass Transfer, 113 (2017), pp. 662–682.

[32] F. P. INCROPERA, *Fundamentals of heat and mass transfer*, no. v. 1 in Fundamentals of Heat and Mass Transfer, John Wiley, 6 ed., 2007.

[33] D. JURIC AND G. TRYGGVASON, *Computations of boiling flows*, International Journal of Multiphase Flow, 24 (1998), pp. 387–410.

[34] M. KANG, R. P. FEDKIW, AND X.-D. LIU, *A Boundary Condition Capturing Method for Multiphase Incompressible Flow*, Journal of Scientific Computing, 15 (2000), pp. 323–360.

[35] I. KATAOKA, *Local instant formulation of two-phase flow*, International Journal of Multiphase Flow, 12 (1986), pp. 745–758.

[36] C. KUNKELMANN, *Numerical modeling and investigation of boiling phenomena*, PhD thesis, Technische Universität, 2011.

[37] B. LAFAURIE, C. NARDONE, R. SCARDOVELLI, S. ZALESKI, AND G. ZANETTI, *Modelling Merging and Fragmentation in Multiphase Flows with SURFER*, Journal of Computational Physics, Volume 113, Issue 1, p. 134-147., 113 (1994), pp. 134–147.

[38] B. P. LEONARD, *A stable and accurate convective modelling procedure based on quadratic upstream interpolation*, Computer Methods in Applied Mechanics and Engineering, 19 (1979), pp. 59–98.

[39] J. LI, *Calcul d'interface affine par morceaux*, Comptes rendus de l'Académie des sciences. Série II, Mécanique, physique, chimie, astronomie, 320 (1995), pp. 391–396.

[40] R. MITTAL AND G. IACCARINO, *Immersed boundary methods*, Annu. Rev. Fluid Mech., 37 (2005), pp. 239–261.

[41] D. Q. NGUYEN, R. P. FEDKIW, AND M. KANG, *A Boundary Condition Capturing Method for Incompressible Flame Discontinuities*, Journal of Computational Physics, 172 (2001), pp. 71–98.

[42] B. D. Nichols and C. W. Hirt, *Calculating three-dimensional free surface flows in the vicinity of submerged and exposed structures*, Journal of Computational Physics, 12 (1973), pp. 234–246.

[43] S. Osher and J. A. Sethian, *Fronts propagating with curvature-dependent speed: algorithms based on Hamilton-Jacobi formulations*, Journal of computational physics, 79 (1988), pp. 12–49.

[44] M. S. Plesset and A. Prosperetti, *Bubble dynamics and cavitation*, Annual review of fluid mechanics, 9 (1977), pp. 145–185.

[45] S. Popinet, *Gerris: a tree-based adaptive solver for the incompressible Euler equations in complex geometries*, Journal of Computational Physics, 190 (2003), pp. 572–600.

[46] S. Popinet, *An accurate adaptive solver for surface-tension-driven interfacial flows*, Journal of Computational Physics, 228 (2009), pp. 5838–5866.

[47] S. Popinet and S. Zaleski, *Bubble collapse near a solid boundary: a numerical study of the influence of viscosity*, Journal of Fluid Mechanics, 464 (2002), pp. 137–163.

[48] D. Rossinelli, B. Hejazialhosseini, P. Hadjidoukas, C. Bekas, A. Curioni, A. Bertsch, S. Futral, S. J. Schmidt, N. A. Adams, and P. Koumoutsakos, *11 PFLOP/s simulations of cloud cavitation collapse*, in High Performance Computing, Networking, Storage and Analysis (SC), 2013 International Conference for, 2013, pp. 1–13.

[49] M. Rudman, *A volume-tracking method for incompressible multifluid flows with large density variations*, International Journal For Numerical Methods In Fluids, 28 (1998), pp. 357–378.

[50] M. S. Sagan, *Simulation numérique directe et étude expérimentale de l'ébullition nucléée en microgravité: application aux réservoirs des moteurs d'Ariane V*, PhD thesis, École Doctorale Mécanique, Énergétique, Génie civil et Procédés (Toulouse); 154236012, 2013.

[51] Y. Sato and B. Niceno, *Nucleate pool boiling simulations using the interface tracking method: Boiling regime from discrete bubble to vapor mushroom region*, International Journal of Heat and Mass Transfer, 105 (2017), pp. 505–524.

[52] Y. Sato and B. Ničeno, *A conservative local interface sharpening scheme for the constrained interpolation profile method*, International Journal for Numerical Methods in Fluids, 70 (2012), pp. 441–467.

[53] ——, *A sharp-interface phase change model for a mass-conservative interface tracking method*, Journal of Computational Physics, 249 (2013), pp. 127–161.

[54] R. Scardovelli and S. Zaleski, *Direct Numerical Simulation of Free-Surface and Interfacial Flow*, Annual Review of Fluid Mechanics, vol. 31, pp. 567-603, 31 (1999), pp. 567–603.

[55] R. Scardovelli and S. Zaleski, *Analytical Relations Connecting Linear Interfaces and Volume Fractions in Rectangular Grids*, Journal of Computational Physics, 164 (2000), pp. 228–237.

[56] R. Scardovelli and S. Zaleski, *Interface reconstruction with least-square fit and split Eulerian-Lagrangian advection*, International Journal For Numerical Methods In Fluids, 41 (2003), pp. 251–274.

[57] J. Schlottke and B. Weigand, *Direct numerical simulation of evaporating droplets*, Journal of Computational Physics, 227 (2008), pp. 5215–5237.

[58] L. E. Scriven, *On the dynamics of phase growth*, Chemical engineering science, 10 (1959), pp. 1–13.

[59] C.-W. Shu, *High Order Weighted Essentially Nonoscillatory Schemes for Convection Dominated Problems*, Siam Review, 51 (2009), pp. 82–126.

[60] L. Signor, *Contribution à la caractérisation et à la modélisation du micro-écaillage de l'étain fondu sous choc*, PhD thesis, Ecole Nationale Supérieure de Mécanique et d'Aérotechnique, 2008.

[61] L. Signor, A. Dragon, G. Roy, T. De Rességuier, and F. Llorca, *Dynamic fragmentation of melted metals upon intense shock wave loading. Some modelling issues applied to a tin target*, Archives of Mechanics, 60 (2008), pp. 323–343.

[62] L. Signor, E. Lescoute, D. Loison, T. De Rességuier, A. Dragon, and G. Roy, *Experimental study of dynamic fragmentation of shockloaded metals below and above melting*, ICEM 14 - 14th International Conference on Experimental Mechanics, Poitiers, France, Edited by Fabrice Brémand; EPJ Web of Conferences, 6 (2010), p. 39012.

[63] L. Signor, G. Roy, P.-Y. Chanal, P.-L. Héreil, F. Buy, C. Voltz, F. Llorca, T. De Rességuier, and A. Dragon, *Debris Cloud Ejection from Shock-Loaded Tin Melted on Release or on Compression*, Shock Compression of Condensed Matter 2009: Proceedings of the American Physical Society Topical Group on Shock Compression of Condensed Matter. AIP Conference Proceedings, Volume 1195. AIP Conference Proceedings, Volume 1195, Issue 1, p.1065-1088, 1195 (2009), pp. 1065–1088.

[64] G. Son and V. K. Dhir, *Numerical simulation of film boiling near critical pressures with a level set method*, TRANSACTIONS-AMERICAN SOCIETY OF MECHANICAL ENGINEERS JOURNAL OF HEAT TRANSFER, 120 (1998), pp. 183–192.

[65] G. Son, N. Ramanujapu, and V. K. Dhir, *Numerical simulation of bubble merger process on a single nucleation site during pool nucleate boiling*, Journal of heat transfer, 124 (2002), pp. 51–62.

[66] D. S. Sorenson, R. W. Minich, J. L. Romero, T. W. Tunnell, and R. M. Malone, *Ejecta particle size distributions for shock loaded Sn and Al metals*, Journal of Applied Physics, Volume 92, Issue 10, pp. 5830-5836 (2002)., 92 (2002), pp. 5830–5836.

[67] E. A. Spiegel and G. Veronis, *On the Boussinesq approximation for a compressible fluid.*, The Astrophysical Journal, 131 (1960), p. 442.

[68] N. A. Stebnovskii, *Formation conditions for bubble suspensions upon shock-wave loading of liquids*, Journal of Applied Mechanics and Technical Physics, 41 (2000), pp. 251–260.

[69] S. V. Stebnovskii, *Generalized rheological model of cavitating condensed media*, Journal of Applied Mechanics and Technical Physics, 42 (2001), pp. 482–492.

[70] ——, *Generalized rheological model of shear deformation of structured condensed media*, Journal Of Applied Mechanics And Technical Physics, 48 (2007), pp. 694–700.

[71] M. Sussman, *A second order coupled level set and volume-of-fluid method for computing growth and collapse of vapor bubbles*, Journal of Computational Physics, Volume 187, Issue 1, p. 110-136., 187 (2003), pp. 110–136.

[72] M. Sussman and E. G. Puckett, *A Coupled Level Set and Volume-of-Fluid Method for Computing 3D and Axisymmetric Incompressible Two-Phase Flows*, Journal of Computational Physics, 162 (2000), pp. 301–337.

[73] M. Sussman, P. Smereka, and S. Osher, *A level set approach for computing solutions to incompressible two-phase flow*, Journal of Computational physics, 114 (1994), pp. 146–159.

[74] W. G. Szymczak, J. C. W. Rogers, J. M. Solomon, and A. E. Bergert, *A numerical algorithm for hydrodynamic free boundary problems*, Journal of Computational Physics, 106 (1993), pp. 319–336.

[75] H. Tan, *An adaptive mesh refinement based flow simulation for free-surfaces in thermal inkjet technology*, International Journal Of Multiphase Flow, 82 (2016), pp. 1–16.

[76] S. Tanguy, T. Ménard, and A. Berlemont, *A Level Set Method for vaporizing two-phase flows*, Journal of Computational Physics, 221 (2007), pp. 837–853.

[77] G. Tomar, G. Biswas, A. Sharma, and A. Agrawal, *Numerical simulation of bubble growth in film boiling using a coupled level-set and volume-of-fluid method*, Physics of Fluids, Volume 17, Issue 11, pp. 112103-112103-13 (2005)., 17 (2005), pp. 112103–112103.

[78] G. Tomar, G. Biswas, A. Sharma, and S. W. J. Welch, *Multimode analysis of bubble growth in saturated film boiling*, Physics of Fluids, Volume 20, Issue 9, pp. 092101-092101-7 (2008)., 20 (2008), pp. 092101–092101.

[79] G. Tryggvason, A. Esmaeeli, and N. Al-Rawahi, *Direct numerical simulations of flows with phase change*, Computers & structures, 83 (2005), pp. 445–453.

[80] G. Tryggvason, A. Esmaeeli, J. Lu, and S. Biswas, *Direct numerical simulations of gas/liquid multiphase flows*, Fluid Dynamics Research, 38 (2006), pp. 660–681.

[81] G. Tryggvason, R. Scardovelli, and S. Zaleski, *Direct Numerical Simulations of Gas–Liquid Multiphase Flows*, Cambridge University Press, 2011.

[82] S. O. Unverdi and G. Tryggvason, *A front-tracking method for viscous, incompressible, multi-fluid flows*, Journal of Computational Physics (ISSN 0021-9991), vol. 100, no. 1, May 1992, p. 25-37., 100 (1992), pp. 25–37.

[83] H. K. Versteeg and W. Malalasekera, *An Introduction to Computational Fluid Dynamics: The Finite Volume Method*, Pearson Education Limited, 2007.

[84] M. Watanabe and A. Prosperetti, *Shock waves in dilute bubbly liquids*, Journal of Fluid Mechanics, 274 (1994), pp. 349–381.

[85] S. W. J. Welch and T. Rachidi, *Numerical Computation of Film Boiling Including Conjugate Heat Transfer*, Numerical Heat Transfer: Part B: Fundamentals, vol. 42, issue 1, pp. 35-53, 42 (2002), pp. 35–53.

[86] S. W. J. Welch and J. Wilson, *A Volume of Fluid Based Method for Fluid Flows with Phase Change*, Journal of Computational Physics, Volume 160, Issue 2, pp. 662-682 (2000)., 160 (2000), pp. 662–682.

[87] G. D. Weymouth and D. K.-P. Yue, *Conservative Volume-of-Fluid method for free-surface simulations on Cartesian-grids*, Journal of Computational Physics, Volume 229, Issue 8, p. 2853-2865., 229 (2010), pp. 2853–2865.

[88] F. M. White, *Fluid Mechanics*, McGraw-Hill international editions, McGraw-Hill, 5 ed., 2003.

[89] D. Youngs, *Numerical Methods for Fluid Dynamics*, vol. 24, Academic Press, 01 1982, ch. Time-Dependent Multi-material Flow with Large Fluid Distortion, pp. 273–285.

Appendix A

Boussinesq thermal energy conservation

In this chapter, the thermal energy conservation equation is simplified by applying the Boussinesq approximation. The derivation will be done by writing the equations in differential form. Parts of the derivation are taken from [12].

A.1 Boussinesq approximation

The general form of the conservation of thermal energy is given in integral form in (2.41). In differential form, it is written

$$\frac{\partial(\rho e_i)}{\partial t} + \boldsymbol{\nabla} \cdot (\rho e_i \boldsymbol{u}) = -p\,(\boldsymbol{\nabla} \cdot \boldsymbol{u}) + \mathrm{S}\,, \tag{A.1}$$

where the nomenclature is the same as in Chapter 2 and S is the heat transfer, viscous dissipation and other source terms. This equation can be rewritten as

$$\rho \left(\frac{\partial e_i}{\partial t} + \boldsymbol{u} \cdot \boldsymbol{\nabla} e_i \right) = -p\,(\boldsymbol{\nabla} \cdot \boldsymbol{u}) + \mathrm{S}\,, \tag{A.2}$$

by using mass conservation

$$\frac{\partial \rho}{\partial t} + \boldsymbol{\nabla} \cdot (\rho \boldsymbol{u}) = 0\,. \tag{A.3}$$

Since the temperature variations are small, the specific heat capacity of a phase is assumed constant and it is assumed that fluid properties adhere to the ideal gas law [9, p.180]

$$p = \rho R T\,, \tag{A.4}$$

with R the gas constant. The internal energy is now approximated as $e_i = c_v T$, with c_v the constant volume specific heat. This can be substituted into (A.2)

$$\rho c_v \left(\frac{\partial T}{\partial t} + \boldsymbol{u} \cdot \boldsymbol{\nabla} T \right) = -p\,(\boldsymbol{\nabla} \cdot \boldsymbol{u}) + \mathrm{S}\,, \tag{A.5}$$

where the specific heat is removed from partial derivatives, since it is constant. Even though the flow is incompressible, the term for the volumetric pressure work is not neglected, but is rather expanded. To do this, (A.3) is rewritten as

$$\frac{\partial \rho}{\partial t} + \boldsymbol{u} \cdot \boldsymbol{\nabla} \rho = \rho \left(\boldsymbol{\nabla} \cdot \boldsymbol{u} \right) , \tag{A.6}$$

so that the volumetric pressure work term is written

$$p \left(\boldsymbol{\nabla} \cdot \boldsymbol{u} \right) = \frac{p}{\rho} \left(\frac{\partial \rho}{\partial t} + \boldsymbol{u} \cdot \boldsymbol{\nabla} \rho \right) \tag{A.7}$$

The flow is assumed incompressible and by the Boussinesq approximation, it is assumed that temperature variations are relatively small. This means that pressure changes in the flow have a negligible impact on the pressure, but would rather effect the velocity. Using this assumption, the pressure derivative can be written

$$\left(\frac{\partial \rho}{\partial t} + \boldsymbol{u} \cdot \boldsymbol{\nabla} \rho \right) \approx \left(\frac{\partial \rho}{\partial T} \right)_p \left(\frac{\partial T}{\partial t} + \boldsymbol{u} \cdot \boldsymbol{\nabla} T \right) . \tag{A.8}$$

The volumetric thermal expansion coefficient is given by [32, p.564]

$$\beta = -\frac{1}{\rho} \left(\frac{\partial \rho}{\partial T} \right)_p \tag{A.9}$$

Substituting the ideal gas law into (A.9), it is found that $\beta = {}^1/_T$. Using this and (A.8), it is now possible to write

$$\begin{aligned} p \left(\boldsymbol{\nabla} \cdot \boldsymbol{u} \right) &= \frac{p}{\rho} \left(\frac{\partial \rho}{\partial T} \right)_p \left(\frac{\partial T}{\partial t} + \boldsymbol{u} \cdot \boldsymbol{\nabla} T \right) \\ &= \rho \left(c_v - c_p \right) \left(\frac{\partial T}{\partial t} + \boldsymbol{u} \cdot \boldsymbol{\nabla} T \right) . \end{aligned} \tag{A.10}$$

The ideal gas law was used to here to substitute $p = \rho(c_p - c_v)T$, with $R = c_p - c_v$ for ideal gases. Substituting this into (A.5), the thermal energy conservation can now be written, after applying the Boussinesq approximation as

$$\rho c_p \left(\frac{\partial T}{\partial t} + \boldsymbol{u} \cdot \boldsymbol{\nabla} T \right) = \boldsymbol{\nabla} \cdot k \boldsymbol{\nabla} T + \Phi \, , \tag{A.11}$$

where S was replaced with the Fourier law for heat transfer and viscous dissipation.

Appendix B

Rayleigh-Plesset Note

In this chapter, the derivation of the Rayleigh-Plesset equation will be given for one-dimensional, spherically symmetric inviscid flow, as applied in Part I of this work. The pressure at a finite distance will also be derived. This is useful for simulation purposes when a pressure boundary condition is applied at a boundary that is some finite distance from the bubble.

B.1 Rayleigh-Plesset equations

As mentioned in the introduction, the governing equation for a bubble with radius R in an inviscid fluid will be derived. The flow is assumed to be spherically symmetric and incompressible. First, the velocity $\boldsymbol{u}$ is written as a function of the general radial coordinate r and the bubble radius R. The continuity equation for incompressible flow is

$$\boldsymbol{\nabla} \cdot \boldsymbol{u} = 0\,. \tag{B.1}$$

For a spherically symmetric flow, the velocity $\boldsymbol{u}$ is only a function of the radial coordinate r and time t

$$\boldsymbol{u} = u(r,t)\,, \tag{B.2}$$

so the velocity will simply be denoted $u = u(r,t)$.

In general, the velocity at position r can be written as some function of time

$$u = \frac{f\,(t)}{r^2}\,. \tag{B.3}$$

At the interface of the bubble $r = R$, so that $u = {}^{f(t)}/_{R^2} = {}^{dR}/_{dt} = \dot{R}$. Rewriting this equation gives

$$f\,(t) = \dot{R}R^2 \tag{B.4}$$

and substituting this back into (B.3) gives

$$u = \frac{\dot{R}R^2}{r^2} \tag{B.5}$$

The one-dimensional Euler equation is given by

$$\frac{Du}{Dt} = -\frac{\boldsymbol{\nabla} p}{\rho} \tag{B.6}$$

Substituting (B.5) into the above equation gives

$$\frac{\ddot{R}R^2 + 2R\dot{R}^2}{r^2} - \frac{2\dot{R}^2R^4}{r^5} = -\frac{1}{\rho_\ell}\frac{dp}{dr}\,, \tag{B.7}$$

with ρ_ℓ the liquid density.

This equation can now be integrated from the bubble interface at R, where the pressure is p_R to infinity at pressure p_∞:

$$\begin{aligned}\ddot{R}R + \frac{3}{2}\dot{R}^2 &= \frac{p_R - p_\infty}{\rho_l} \\ &= \frac{p_c - \frac{2\sigma}{R} - p_\infty}{\rho_l}\,,\end{aligned} \tag{B.8}$$

with σ the surface tension coefficient and the pressure jump from surface tension accounted for.

B.2 Pressure at a finite distance

We are interested in knowing the spatial pressure distribution in order to set the pressure on the boundary of a numerical simulation. From equation B.7, we now integrate from R to r in space, at respective pressures p_R and $p(r)$. An expression is then obtained for p as a function of r which can be used to set the pressure at some finite distance:

$$p(r,t) = p_R - \rho_l\left(\frac{\dot{R}^2R^4}{2r^4} - \frac{\ddot{R}R^2 + 2R\dot{R}^2}{r} - \frac{\dot{R}^2}{2} + \ddot{R}R + 2\dot{R}^2\right)\,, \tag{B.9}$$

with $p_R = p_c - \dfrac{2\sigma}{R}$.